ALGORITHM FOR REMOTE SENSING OF TROPOSPHERIC AEROSOL OVER DARK TARGETS
March 2024

Current PI/lead: Robert C. Levy[1]
Programming: Shana Mattoo [2,1], Virginia Sawyer [2,1], Praju Kiliyanpilakkil[2,1]
Science Co-Is: Yingxi Shi [3,1], Pawan Gupta [1], Lorraine Remer[3]
Current team contributors: Mijin Kim[4,1], Yaping Zhou[4,1], Richard Kleidman[3,1]

Previous leads: Lorraine A. Remer[3], Didier Tanré[5], and Yoram J. Kaufman[1*]

[1] NASA Goddard Space Flight Center, Code 613, Greenbelt, MD 20771, USA
[2] Science Systems and Applications, Inc., Lanham, MD, USA.
[3] University of Maryland Baltimore County (UMBC), Baltimore, MD 21228, USA.
[4]Morgan State University (MSU), Baltimore, MD USA
[5]Laboratoire d'Optique Atmospherique, Université de Sciences et Techniques de Lille, Villeneuve d'Ascq, France

Abstract:

Atmospheric particulates otherwise known as aerosols, have a significant impact on the Earth's radiative budget, climate change, hydrological processes, and the global carbon, nitrogen and sulfur cycles. To understand the wide-ranging effects of aerosols, it is necessary to measure aerosol characteristics globally with high spatial and temporal resolution. This Algorithm Theoretical Basis Document (ATBD) describes the family of "Dark-Target" (DT) algorithms for retrieving aerosol properties over land and ocean, as applied to spectral reflectance observed by a multi-spectral wavelength imager on a satellite or aircraft. Originally developed for Moderate resolution Imaging Spectroradiometer (MODIS) aboard NASA's Terra and Aqua satellites, DT has been ported to, and is producing products from additional satellite sensors, including: Visible-Near Infrared Radiometer Suite (VIIRS) aboard Suomi-NPP and NOAA's Joint Polar Satellite Series (JPSS), Advanced Baseline Imager (ABI) aboard NOAA's Geostationary Operational Environmental System-R series (GOES-R), Advanced Himawari Imager (AHI) aboard Japan Meteorological Agency's (JMA) Himawari series. DT has also been used for retrieving on enhanced-MODIS Airborne Simulator (eMAS) flying on ER-2 high-altitude aircraft during multiple field campaigns.

Essentially, DT works by observing the contrast of highly reflective aerosol over a surface of low scattering (e.g., a "dark" surface), using a Lookup Table (LUT) approach to infer aerosol properties from multi-spectral observations. These observations include visible (VIS), near-infrared (NIR) and shortwave-infrared (SWIR) wavelength bands, which are each in "window" wavelengths with minimum gas absorptions. Additional wavelength bands are used to further constrain the aerosol/surface contrast and/or help identify clouds or pixels that must be filtered. Using the LUT, the DT algorithm retrieves the aerosol optical depth (AOD) over ocean and vegetated land, as well as proxies for aerosol size (e.g. Fine-Model Weighting or Ångström Exponent) over ocean. These aerosol products are primarily intended for radiative budget and climate applications, but are also relevant for hydrological, oceanographic and air quality applications.

This ATBD updates and simplifies previous complete versions, including the 1996 pre-launch version (ATBD-96), 2009 Collection 5 version-Revision 2: (ATBD-09), and details presented at the dark-target aerosol website, along with information from various papers, users' guides, and product "change" documents. We attempt to describe the DT algorithm generically (applied to all versions/satellites/sensors) while also discussing/listing modifications that are required to retrieve on a particular satellite/sensor, or for a particular application or instance.

TABLE 1-1 LIST OF PRODUCTS REFERRED TO WITHIN THIS ATBD.

Product ID / name	Sensor – Satellite (or experiment)	Collection or Version	Dates of Records	DOI or website for access	Notes
STANDARD and CONTINUITY PRODUCTS					
MOD04_L2 / Aerosol 5-Min L2 Swath 10km	MODIS-Terra	C 61	3/2000 – 3/2023	http://dx.doi.org/10.5067/MODIS/MOD04_L2.061	Standard 10 km product (joint with Deep Blue)
MYD04_L2 / Aerosol 5-Min L2 Swath 10km	MODIS-Aqua	C 61	6/2002 – 3/2023	http://dx.doi.org/10.5067/MODIS/MYD04_L2.061	Standard 10 km product (joint with Deep Blue)
MOD04_3K Aerosol 5-Min L2 Swath 3km	MODIS-Terra	C 61	3/2000 – 3/2023	http://dx.doi.org/10.5067/MODIS/MOD04_3K.061	Standard 3 km product (DT only)
MYD04_3K Aerosol 5-Min L2 Swath 3km	MODIS-Aqua	C 61	6/2002 – 3/2023	http://dx.doi.org/10.5067/MODIS/MYD04_3K.061	Standard 3 km product (DT only)
AERDT_L2_VIIRS_SNPP / Dark Target Aerosol L2 6-Min Swath 6 km	VIIRS-SNPP	V2.0	3/2012-9/2023	http://dx.doi.org/10.5067/VIIRS/AERDT_L2_VIIRS_SNPP.002	Standard 6 km product
AERDT_L2_VIIRS_NOAA20 / Dark Target Aerosol L2 6-Min Swath 6 km	VIIRS-N20	V2.0	2/2018-3/2023	http://dx.doi.org/10.5067/VIIRS/AERDT_L2_VIIRS_NOAA20.002	Standard 6 km product
Airborne products (field experiments)					
eMASL2AER	eMAS - SEAC4RS		08/2013 – 09/2013		0.5 km product
eMASL2AER	eMAS - FIREXAQ		08/2019 – 09/2019	https://ladsweb.modaps.eosdis.nasa.gov/archive/MAS_eMAS/FIREXAQ/	0.5 km product
MEaSUREs products (satellite = XAERDT)					
XAERDT_L2_MODIS_Terra	MODIS-Terra	V 1.0	01/2019-12/2022	https://ladsweb.modaps.eosdis.nasa.gov/archive/allData/5019	10 km product
XAERDT_L2_MODIS_Aqua	MODIS-Aqua	V 1.0	01/2019-12/2022	https://ladsweb.modaps.eosdis.nasa.gov/archive/allData/5019	10 km product
XAERDT_L2_VIIRS_SNPP	VIIRS-SNPP	V 1.0	01/2019-12/2022	https://ladsweb.modaps.eosdis.nasa.gov/archive/allData/5019	6 km product
XAERDT_L2_ABI_G16	ABI – GOES-16	V 1.0	01/2019-12/2022	https://ladsweb.modaps.eosdis.nasa.gov/archive/allData/5019	10 km product
XAERDT_L2_ABI_G17	ABI – GOES-17	V 1.0	01/2019-12/2022	https://ladsweb.modaps.eosdis.nasa.gov/archive/allData/5019	10 km product
XAERDT_L2_AHI_H08	AHI Himawari-8	V 1.0	01/2019-12/13/2022	https://ladsweb.modaps.eosdis.nasa.gov/archive/allData/5019	10 km product
XAERDT_L2_AHI_H09	AHI Himawari-9	V1.0	12/13/2022-12/31/2022	https://ladsweb.modaps.eosdis.nasa.gov/archive/allData/5019	10 km product
Other products (test, etc.)					
	ABI – GOES-18	V 1.0	After June 2022		10 km product
	AHI Himawari - 9	V 1.0	After Dec 2022		10 km product
	VIIRS – NOAA21				

TABLE OF CONTENTS

1. Introduction

Ranging in size from nanometers (nm) to tens of micrometers (μm), atmospheric particulate matter known as aerosols impact the Earth's radiative budget, climate change, hydrological processes, and the global carbon, nitrogen and sulfur cycles. To understand the wide-ranging effects of aerosol, it is necessary to measure the aerosol characteristics globally with high spatial and temporal resolution. The polar-orbiting MODerate resolution Imaging Spectrometer [MODIS-*Salmonson et al., 1989*] on board NASA Terra (1999 -) and Aqua (2002 -) sensor was developed, in-part, for the capability of observing global aerosol. The family of Dark-Target algorithms, discussed here, was originally developed to take advantage of MODIS's ability to observe aerosols. In fact, MODIS has been flying for so long that the aerosol record is now over 20 years. However, with the imminent de-orbiting of both Terra and Aqua missions in the next few years, means that such a global data record could be in danger of ending. Fortunately, DT is versatile, and can be run on any sensor with appropriate coverage and sampling in spectral, spatial, and temporal domains. Hence it has been ported to Visible Near Infrared Radiometer Suite (VIIRS) on the Suomi-NPP (SNPP) and now the Joint Polar Satellite System (JPSS) series of polar orbiting satellites to continue the low earth orbit (LEO) data record. More recently, DT has been ported to Advanced Baseline Imager (ABI) on NOAA's Geostationary Operational Environment Satellite series-R (GOES-R), and Advanced Himawari Imager (AHI) on Japan's Himawari series. ABI and AHI are both in geostationary orbits (GEO). DT has also been ported to run on higher-spatial resolution sensors including enhanced MODIS Airborne Simulator (eMAS), to study aerosol processes near sources or near clouds.

The DT aerosol algorithm takes advantage of these sensors' wide spectral range for observing reflected solar radiation. In fact DT is two sub-algorithms, one for deriving aerosols over land (DT-L) and the second for retrieving aerosols over ocean (DT-O). Both assume that the ambient aerosol distribution is a summation of two particle types or "models", one that is dominated by small particles (radius < 1.0 μm) known as the *fine model*, and one that is dominated by larger particles known as the *coarse model*. Both fine and coarse aerosol models scatter and absorb sunlight, but their relative contribution in any one wavelength depends on its details. The goal of the DT algorithm to use appropriate assumptions and lookup tables (LUTs) to derive the total aerosol optical loading and the relative weighting of the fine and coarse models. Thus, the basic aerosol products from DT include total spectral 'aerosol optical depth' (AOD or τ) and the 'Fine aerosol-Model Weighting' (FMW or η). In the literature, AOD is sometimes referred as 'aerosol optical thickness' (AOT), but we shall use AOD. The concept of FMW is also variously defined, however, here η refers to both the relative contribution of the fine model to the total observed reflectance at any wavelength as well as the contribution of the fine model to the total AOD at a specific defined wavelength, namely 0.55 μm. Each retrieval of AOD + FMW product is also associated with Quality Assurance/Confidence (QAC) and additional products representing diagnostic and derived quantities.

The general science and methodology of both flavors were conceived and developed before the Terra launch and described in depth in Kaufman, et al. [*1997b*], Tanré, et al. [*1997*] and ATBD-96. The theoretical basis of DT-O is largely the same as pre-launch. DT-L has had more significant changes, first described by Levy et al. [*2007a, b*] and ATBD-09. Since 2009, rather than update the ATBD in its entirety, updates to the algorithm and products have been described in the literature and via "User Guides".

Routine *standard* MODIS products are designated into "Collections", which means that calibration and processing of the on-orbit observations (the Level 1B or L1B) and the science and processing of the along-orbit retrievals and gridded aggregations (Level 2 or L2 and Level 3 or L3) are applied consistently. The at-launch version was used for all Collections through Collection 4 (C004). ATBD-

09 coincided with Collection 5 (C005) and a subsequent L1B re-processing (C51). Collection 6 (C006 or C6) began in 2013, and with major updates to L1B and small updates to the DT algorithm, MODIS is currently running as Collection 6.1 (C61) with plans to begin a Collection 7 (C007 or C7) sometime in 2024. Note that MODIS Collections include both forward processing (from starting point going forward) as well as re-processing (back to beginning of mission). For MODIS, standard Collections are produced by the MODIS Adaptive Processing System (MODAPS), at Goddard Space Flight Center in Maryland. A special flavor of the standard MODIS processing is known as the Near Real Time (NRT) that is produced by NASA's Land, Atmosphere Near-real-time Capability for EOS (LANCE) system. Although different requirements for the availability of L1B data and ancillary data, the MODIS NRT processing uses identical versions of the MODIS DT retrieval code. In all standard and NRT processing, the MODIS L2 aerosol product is known as MxD04, where the x=O for MODIS on Terra and x=Y for MODIS on Aqua. All standard MxD04 products are publicly available through NASA's Level-1 and Atmosphere Archive & Distribution System Distributed Active Archive Center (LAADS-DAAC).

Processed under the auspices of a different Science Investigation Production and Support (SIPS), known as the Atmosphere-SIPS at the University of Wisconsin (A-SIPS), VIIRS standard processing is categorized by Versions. Rather than L1B and L2 processing happening necessarily in-step, updates to algorithms are applied when ready. Relevant to the DT algorithm, the most current set of products is known as Version 2 (V2). These products, also publicly available through the LAADS-DAAC, are known as AERDT_L2_VIIRS_x, where x=SNPP, NOAA20 (was JPSS-1) or NOAA21 (was JPSS-2).

Using SIPS (MODAPS and A-SIPS) as well as additional resources, DT products for the geostationary sensors (ABI and AHI) are known as AERDT_L2_y_x, where y=ABI or AHI, and x=G16, G17, G18, H08 or H09 (for GOES 16, 17 or 18, or Himawari 8 and 9). Supported by the NASA-funded Making Earth System Data Records for Use in Research Environments (MEaSUREs) Program, the DT algorithm is being used to process a subset of GEO and LEO observations from 2019-2022, with the products being known as XAERDT_L2_y_x, where y=sensor (e.g. MODIS, VIIRS, ABI or AHI) and x=platform (Terra, Aqua, SNPP, N20, N21, G16, G17 or H08). To be consistent, all XAERDT products are currently designated as Version 1 (V1), regardless of L1B provenance and calibration, and are also archived via the LAADS-DAAC.

While MODIS has historically provided the anchor for updating and improving the DT algorithm, the need to port to different sensors and for different purposes has led to the idea of the generic DT framework known as the *DT-Package*. Ideally, the DT-Package can run within any computer environment and with minimal "if-then-else" type statements can pick the appropriate L1B and LUTs for a particular sensor or purpose. However, because of subtle differences between instrument characteristics, availability of analogous wavelength bands, file formats, or other aspects, the DT-Package presents differences from version of DT used for MODIS C6.1. In terms of a resulting AOD retrieval on MODIS, a user would see only minor differences. However, with our desire to develop continuity between MODIS, VIIRS, ABI, AHI and possible future sensors, we intend to use DT-Package as a basis for processing/re-processing MODIS C7. For the MEaSUREs XAERDT product, the DT-Package has been used for all sensors. Table 1-1 lists all the DT products including MODIS, VIIRS, and products generated under MEASURES project.

The history of the DT algorithm also involves a systematic evaluation process, utilizing uncertainty analyses, sensitivity studies, and comparisons with ground-based sunphotometers, primarily from the Aerosol Robotic Network (AERONET) over land and coastlines and Marine Aerosol Network (MAN) over the open ocean. To gauge the accuracy of the retrieved data against ground truth, an expected error (EE) envelope is established, requiring that a minimum of 2/3 (or one standard deviation) of

global matched pairs (e.g. MODIS versus AERONET AOD at 0.55 μm) should fall within this EE, defined to be the sum of absolute and relative errors. For MODIS C6.1 standard resolution (10 km) product, EE is shown to be $\pm(0.05 + 0.15\tau_{ground\_truth})$ over land and $(+(0.04 + 0.10\tau_{ground\_truth}, -(0.02 + 0.10\tau_{ground\_truth}))$ over ocean (note +0.02 asymmetry around zero). For the higher-resolution (3KM) MODIS products, as well as VIIRS V2 product and the ABI products, the EE envelope is looser. For these products, we see EE about $\pm(0.05 + 0.20\tau_{ground\_truth})$ overland and $\pm(0.05 + 0.15\tau_{ground\_truth})$ overocean. In addition to continuous validation against ground measurements, intercomparisons across all applied sensors are conducted to assess the consistency between DT products.

 Due to the similarity in the basic science of the current DT retrieval (both for MODIS C6.1 and within DT-Package used for VIIRS, ABI and AHI) and the long heritage of DT algorithm, we provide this new ATBD. This, along with accompanying User Guides and published literature, are being used describe commonalities and differences between the various versions.

 This ATBD is organized as follows. Section 2 provides a review of aerosols, their optics, and a history of retrieval strategies. Section 3 describes the family of sensors. Section 4 describes the inputs and processing environment for DT aerosol retrievals, Section 5 introduces the overview of DT retrieval strategy. Section 6 and 7 describe the DT ocean and land aerosol algorithm separately and present the corresponding generic product. Section 8 introduces MODIS 3 km aerosol product. Section 9 describes basic validation strategy. Section 10 explains the file format and content.

2. Aerosols, Optics and Basic Retrieval Strategy

2.1.   Properties of Aerosols

Aerosols are a mixture of solid and liquid particles (in suspension of air) of different sizes, shapes, compositions, and chemical, physical, and thermodynamic properties. They range in size from nanometers to micrometers, spanning from molecular aggregates to cloud droplets. Aerosols between about 0.1 μm and 2.5 μm in radius are of primary interest for climate, precipitation, visibility, and human health studies. Most of these aerosols are found in the troposphere and concentrated toward the Earth's surface (having a scale height about 2-3 km). Aerosols' physical and chemical properties are determined by their sources and production processes. Ambient aerosol distributions contain all size ranges although we generally categorize them as belonging to one of two modes. Fine aerosols (radius between 0.1 and 1.0 μm) are formed by coagulation of smaller nuclei (very fine aerosols) or produced directly during incomplete combustion (from biomass-burning or coal power plants). Aerosols larger than about 1.0 μm are known as coarse particles and are produced primarily from mechanical processes such as erosion of the Earth's surface. Coarse particles include sea salt and soil dust lifted by winds.

The two aerosol size ranges differ in their spatial distribution and life cycle. Coarse mode particles are usually small in number but can contain the largest portion of aerosol mass (or volume). Because of their larger size (and mass), coarse particles are usually quickly settled out of the atmosphere and are concentrated close to their sources. However, convection may lift them into prevailing winds, where they can be transported far from their source. Fine mode, also known as accumulation mode, aerosols have the longest residence time in the atmosphere (days to weeks) because they neither efficiently settle nor coagulate on their own. The fine mode contains the largest portion of aerosol surface area, and therefore the greatest ability to scatter solar radiation. Depending on whether discussing number, mass, volume or optical properties, there are many ways to define the fraction of the fine model to the total aerosol. However, here we use the term *Fine aerosol-Model Weighting* (FMW or, η) to refer to fractional contribution to the optics of the atmospheric column.

Many aerosols are hygroscopic, meaning that they can absorb water vapor and thus become involved in cloud processes and the hydrologic cycle. For most accumulation-sized aerosols, the residence time is on the same order as water vapor in the atmosphere, usually about four to fourteen days. Generally, more hygroscopic aerosols (known as hydrophilic, e.g., sulfate or sea salt) are spherical in shape, whereas those less hygroscopic (e.g., hydrophobic, e.g., soot or dust) tend to be non-spherical. Non-spherical aerosols may be clumplike (soot) or crystalline (certain dusts). Larger aerosols usually have shorter residence times (days to hours) due to dry deposition.

For the purposes of aerosol retrieval from satellite, we must make some assumptions about typical aerosol size distributions and optical properties. We start with basic definitions.

2.1.1. Aerosol Properties

Because aerosols in nature are not monodisperse, we describe with particle size distributions (PSD) in terms of number (nPSD) expressed as functions of radius r or diameter $D=2r$. It is common for remote sensing algorithms to define in terms of radius, and assume a mathematical function for the PSD. Because particle size may cover several orders of magnitude, a Normal (Gaussian) Distribution (ND) may not be useful. The literature commonly uses lognormal (LND), Gamma (GD), and Modified Gamma (MGD), with the LND the most common in remote sensing of aerosols. The LND is extremely convenient because we can define nPSD in terms of $l = \ln r$. Thus, the number distribution $N(r)$, is related to the volume V and area A distributions by:

$$\frac{dN(\ln r)}{d\ln r} = \frac{3}{4\pi r^3}\frac{dV}{dlnr} = \frac{1}{\pi r^2}\frac{dA}{dlnr},$$

<div align="right">Eq. 2-1</div>

such that N_0, V_0, and A_0 are the totals of the corresponding distributions, i.e.,

$$N_0 = \int_0^\infty \frac{dN(\ln r)}{d\ln r}\,d\ln r$$

<div align="right">Eq. 2-2</div>

$$V_0 = \int_0^\infty \frac{dV(\ln r)}{d\ln r}\,d\ln r$$

<div align="right">Eq. 2-3</div>

$$A_0 = \int_0^\infty \frac{dA(\ln r)}{d\ln r}\,d\ln r$$

<div align="right">Eq. 2-4</div>

and $\frac{dN(\ln r)}{d\ln r}$; $\frac{dV(\ln r)}{d\ln r}$; $\frac{dA(\ln r)}{d\ln r}$ are the number/volume/area size distributions with r denoting radius (in

µm). Here, we define the means of the log-radii of the number (r_g) and volume (r_v) distributions, as

$$\ln r_g = \frac{\int_{r_{min}}^{r_{max}}\ln r\,\frac{dN(r)}{dlnr}\,dlnr}{\int_{r_{min}}^{r_{max}}\frac{dN(r)}{dlnr}\,dlnr};\ \ln r_v = \frac{\int_{r_{min}}^{r_{max}}\ln r\,\frac{dV(r)}{dlnr}\,dlnr}{\int_{r_{min}}^{r_{max}}\frac{dV(r)}{dlnr}\,dlnr}$$

<div align="right">Eq. 2-5</div>

and the standard deviations of the log-radii, σ_g and σ_v, as:

$$\sigma_g = \sqrt{\frac{\int_{r_{min}}^{r_{max}}(\ln r - \ln r_g)^2\frac{dN(r)}{dlnr}dlnr}{\int_{r_{min}}^{r_{max}}\frac{dN(r)}{dlnr}dlnr}};\ \sigma_v = \sqrt{\frac{\int_{r_{min}}^{r_{max}}(\ln r - \ln r_v)^2\frac{dV(r)}{dlnr}dlnr}{\int_{r_{min}}^{r_{max}}\frac{dV(r)}{dlnr}dlnr}}$$

<div align="right">Eq. 2-6</div>

Note that σ is the log of the quantity that is commonly defined within the *in situ* community.

Aerosol distributions are often approximately lognormal, so they are often assumed as such. For a lognormal distribution, the moments of order k, M^k are

$$M^K = \int_0^\infty r^k\frac{dN(\ln r)}{d\ln r}\,dlnr = (r_g)^k\exp(0.5k^2\sigma^2).$$

<div align="right">Eq. 2-7</div>

We can see those desirable properties of the lognormal distribution include

$$\sigma = \sigma_g = \sigma_v$$

<div align="right">Eq. 2-8</div>

and

$$r_v = r_g\exp(3\sigma^2).$$

<div align="right">Eq. 2-9</div>

For a single lognormal mode, the volume and number size distribution is:

$$\frac{dN(\ln r)}{d\ln r} = \frac{N_0}{\sigma\sqrt{2\pi}}e^{\left(-\frac{\ln(r/r_g)^2}{2\sigma^2}\right)},$$

<div align="right">Eq. 2-10</div>

and the total volume and number are easily related by

$$N_0 = V_0\frac{3}{4\pi r^3}e^{-\frac{9}{2}\sigma^2}.$$

<div align="right">Eq. 2-11</div>

This also leads to the definition of effective radius r_{eff} of a lognormal distribution, i.e.,

$$r_{eff} = \frac{M^3}{M^2} = \frac{\int_0^\infty r^3\frac{dN}{d\ln r}\,d\ln r}{\int_0^\infty r^2\frac{dN}{d\ln r}\,d\ln r} = \frac{3\,V_0}{4\,A_0} = r_g\,e^{\left(\frac{5}{2}\sigma^2\right)}.$$

<div align="right">Eq. 2-12</div>

For aerosols composed of two or more modes, integration must be over both size bin and mode. For example, for a bimodal distribution,

$$r_{eff} = \frac{\int_0^\infty r^3\frac{(dN_1 + dN_2)}{d\ln r}\,d\ln r}{\int_0^\infty r^2\frac{(dN_1 + dN_2)}{d\ln r}\,d\ln r}.$$

<div align="right">Eq. 2-13</div>

2.1.2. Aerosol Optical Properties

Aerosols are important actors on the Earth's climate and radiation because of their size. Particles most strongly affect the radiation field when their size is most similar to the wavelength of the radiation [e.g. *Chandresekhar, 1950*]. Aerosols in the fine mode (0.1 to 1.0 μm) are similar in size to the wavelengths of solar radiation within the atmosphere, and are also the largest contributors to aerosol surface area. Radiation incident on aerosols may be absorbed, reflected or transmitted, depending on the size, chemical composition (complex refractive index, *m+ik*) and orientation (if non-spherical) of the aerosol particles. Scattering and absorption quantities may be represented as functions of path distance (the scattering/absorption *coefficients*, β_{sca} / β_{abs}, each in units of [per length]), number (the scattering/absorption *cross sections*, σ_{sca} / σ_{abs}, each in units of [area]) or mass (the scattering/absorption *mass coefficients*, B_{sca} / B_{abs}, each in units of [area per mass]). Note that the use of symbols is inconsistent in the literature, and we defined for this work following *Liou* [2002]. *Extinction* (coefficient/cross section/mass coefficient) is the sum of the appropriate absorption and scattering (coefficients/cross sections/mass coefficients), e.g.,

$$\sigma_{ext}(\lambda) = \sigma_{sca}(\lambda) + \sigma_{abs}(\lambda). \qquad \text{Eq. 2-14}$$

for the cross sections (σ here is not the same as in Section 2.1.1). These properties define the amount of radiation 'lost' from the radiation field, per unit of material loading, in the beam direction. Note all of the parameters are dependent on the wavelength λ. The ratio of scattering to extinction (e.g., β_{sca}/β_{ext}) is known as the single scattering albedo (SSA or ω_0). As most aerosols are weakly absorbing in mid-visible wavelengths (except for those with large concentrations of organic/black carbon), extinction is primarily by scattering ($\omega_0 > 0.90$ at 0.55 μm). Black or elemental carbon (soot) can have $\omega_0 < 0.5$ [*Bond and Bergstrom*, 2006] especially near sources. Mineral dusts are unique in that they have a spectral dependence of absorption, such that they absorb more strongly in short visible and UV wavelengths ($\lambda < 0.47$ μm) than at longer wavelengths.

Properties of extinction (scattering and absorption) can be calculated, and are dependent on the wavelength of radiation, as well as characteristics of the aerosols' size distribution, chemical composition, and physical shape. For a single *spherical* aerosol particle, the combination of *refractive index)*, and *Mie size parameter*, *X* (relating the ratio of radius to wavelength, i.e., $X=2\pi r/\lambda$) uniquely describe the scattering and extinction properties of the particle. The scattering/extinction *efficiency* (*Q*) for one particle is related to the cross sections by

$$Q_{sca} = \sigma_{sca}/\pi r^2 \text{ and } Q_{ext} = \sigma_{ext}/\pi r^2. \qquad \text{Eq. 2-15}$$

The scattered photons have an angular pattern, known as the *scattering phase function* ($P_\lambda(\Theta)$), which is a function of the scattering angle (Θ) and wavelength. In other words, the Mie quantities describe the interaction between an incoming photon and aerosol particle, whether it is displaced, scattered, and towards which direction relative to the incoming path.

For a *distribution* of aerosol particles, one is concerned with the scattering by all particles within a space (e.g., per volume, per atmospheric column). In general, since the average separation distance between particles is so much greater than particle radius, particles can be considered independent of each other. For a unit volume (or columnar surface area) containing *N* particles of varying *r*, the integrated extinction/scattering cross sections (the extinction/scattering coefficients) are

$$\beta_{ext} = \int \sigma_{ext}(r)N(r)dr \text{ and } \beta_{sca} = \int \sigma_{sca}(r)N(r)dr. \qquad \text{Eq. 2-16}$$

Therefore, the scattering/extinction *efficiencies* for a representative single aerosol are

$$\bar{Q}_{scat} = \frac{\int \sigma_{sca}(r)N(r)dr}{\int \pi r^2 N(r)dr}.$$ Eq. 2-17

Light scattering by aerosols is a function of the wavelength, the aerosol size distribution, and the aerosol composition [*Fraser, 1975*]. The asymmetry parameter, g_λ, represents the degree of asymmetry of the angular scattering (phase function, P_λ), and is defined as:

$$g_\lambda = \frac{1}{2}\int_0^\pi P_\lambda(\Theta)\cos\Theta\sin\Theta\, d\Theta$$ Eq. 2-18

Values of g_λ range from -1 for entirely backscattered light to +1 for entirely forward scattering. For molecular (Rayleigh) scattering, $g_\lambda = 0$. For aerosol, g_λ typically ranges between 0.6 and 0.7 (mostly forward scattering), with lower values in dry (low relative humidity) conditions [e.g, *Andrews et al.*, 2006]. Specifically, *g* is strongly related to the aerosol size, especially of the accumulation mode size.

Calculating the scattering properties at two or more wavelengths provides information about the aerosols' size. Figure 2-1describes the spectral dependence of the aerosol reflectance for some examples of fine-dominated aerosol types (e.g., dry smoke, urban, and "wet") versus coarse-dominated aerosol types (sea salt and dusts of different sizes). The Ångstrom exponent (AE or α) relates the spectral dependence of the extinction (or scattering) at two wavelengths, λ1 and λ2:

$$\alpha_{\lambda_1,\lambda_2} = \frac{-log(\sigma_{p,\lambda_1}/\sigma_{p,\lambda_2})}{log(\lambda_1/\lambda_1)},$$ Eq. 2-19

[e.g., *Ångstrom*, 1929; *Eck et al.*, 1999]. Often the two wavelengths are defined in the visible or infrared (e.g., blue and either red or near-IR). Larger aerosol size is related to smaller values of α, such that aerosol distributions dominated by fine aerosols have α ≥ 1.6, whereas those dominated by coarse aerosols have α ≤ 0.6. Quadratic fits to more than two wavelengths, known as modified Ångstrom exponents [e.g., *O'Neill et al., 2001*], indicate the curvature of the spectral dependence, and can provide additional size and composition information.
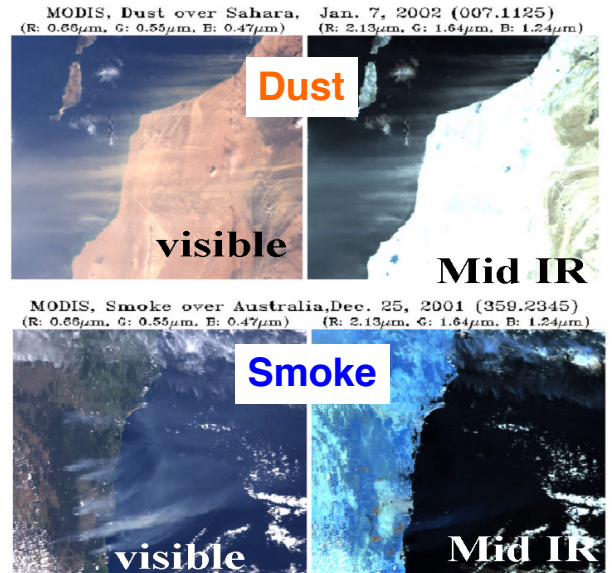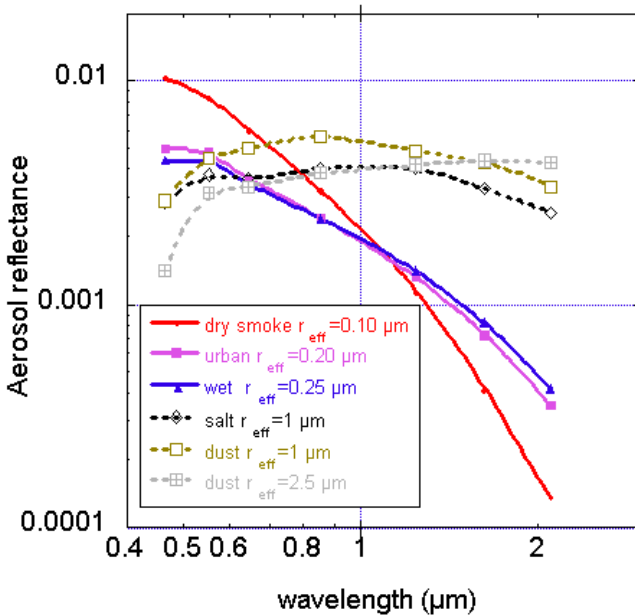

Figure 2-1: Left: Spectral dependence of aerosol reflectance for selected aerosol types for some arbitrary loading. Right: How coarse-sized (e.g. Dust) particles reflect in both shorter visible (Red, Green, Blue) and longer short-wave infrared wavelengths (2.11, 1.64 and 1.24), yet fine-sized (e.g. smoke) particles reflect mostly in the visible. (Figures provided by Yoram Kaufman).

2.1.3. Remote Sensing of Aerosol Optical Depth

Aerosol Optical Depth (AOD) is the fundamental parameter of aerosol remote sensing. The AOD is the integral of the aerosol extinction coefficient over the vertical path from the surface to the top of the atmosphere (TOA), i.e.

$$\tau^a(\lambda) = \int_0^{TOA} \beta_{ext,p}(\lambda, z)dz \qquad \text{Eq. 2-20}$$

where the subscript p represents the contribution from the particles (to be separated from molecular or Rayleigh optical depth). Typically, AOD (at 0.55 µm) range from 0.05 over the remote ocean to 1.0, 2.0 or even 5.0, during episodes of heavy pollution, smoke, or dust. Note, that the AE can also be calculated from spectral AOD.

The simplest way to "measure" AOD using a passive remote sensing technique is with sunphotometry [*Volz*, 1959]. A sunphotometer views the solar disc through a collimator and measures the extinction of direct-beam radiation in distinct wavelength bands. The measurement assumes that the radiation has had little or no interaction with the surface or clouds, and that there is minimal (or known) gas absorption in the chosen wavelength λ. In other words, sunphotometry is a basic application of the Beer-Bouguer-Lambert law, in the form of:

$$L_\lambda(\theta_0) = E_{0,\lambda}(\theta_0, D)e^{-\tau_\lambda^t m^t(\theta_0)} \qquad \text{Eq. 2-21}$$

where L, E_0, d, θ_0, τ^t, and m are the measured solar radiance, extra-terrestrial solar irradiance (irradiance outside the atmosphere), ratio of the actual and average Earth/Sun distance, solar zenith angle, total atmospheric optical depth, and total relative optical air mass, respectively. The factor $\tau_\lambda^t m^t$ is the only unknown, and it can be further broken down as:

$$\tau_\lambda^t m^t = \tau_\lambda^{aer} m^{aer} + \tau_\lambda^R m^R + \tau_\lambda^g m^g \qquad \text{Eq. 2-22}$$

where the superscripts t, *aer*, *R*, and *g* refer to total, aerosol, molecular (Rayleigh scattering), and gas absorption (variably distributed gases such as H_2O, O_3, NO_2, etc.), where the relative optical air masses of each component differ due to differing vertical distributions. The molecular portions of (23) are primarily dependent upon altitude of the surface target, and thus can be accurately calculated (e.g., [*Bodhaine et al., 2003*]). The gas absorption portion, while varying in vertical profile by component, can also be reasonably estimated. Therefore, since errors are well defined, estimation of AOD (τ^{aer}, or hereby simplified as τ) is straightforward from a sunphotometer. When made at more than one wavelength, sunphotometers retrieve spectral (wavelength dependent) τ, which in turn can be used to characterize AE, and the relative size of the ambient aerosol [*Eck et al.*, 1999; *O'Neill et al.*, 2003].

Retrieving AOD from a satellite (or an airborne sensor) is more complicated. For one, the geometry of the solar/target/sensor light path is such that instead of one, there are two passes through the atmosphere. Instead of measuring extinction (and accurately retrieving AOD), our sensor measures back scattered (reflected) light. The scattered light comes not only from the atmosphere, but also from the surface directly, and through surface/atmosphere interactions. This means that for aerosol retrieval, we either have to find situations where the surface contribution is negligible, or can be assumed with accuracy. The geometry of the measurement is illustrated in Figure 2-2, such that θ_0, θ and ϕ are the solar zenith, sensor zenith and relative solar/target relative azimuth angles, respectively. From this we can derive the useful Scattering Angle Θ and Glint Angles (GA or Θ_{glint}) as:

$$\Theta = \cos^{-1}(-\cos\theta_0 \cos\theta + \sin\theta_0 \sin\theta \cos\phi), \qquad \text{Eq. 2-23}$$
$$\Theta_{glint} = \cos^{-1}(\cos\theta_0 \cos\theta + \sin\theta_0 \sin\theta \cos\phi) \qquad \text{Eq. 2-24}$$

Note that in the context of satellite observations the Earth's surface is considered the vantage point from which we define to the 'solar' and 'sensor' angles. One can envision the scattering angle as the

difference in angle between the observation and the direction of the original direct beam. The Glint angle is the difference between the observation and the specular reflection.
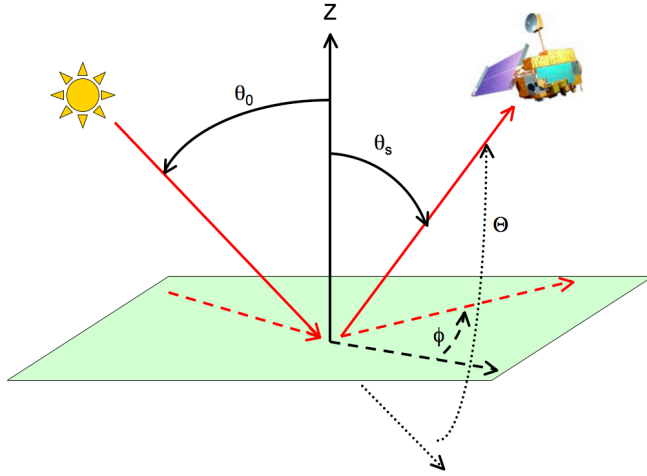
Figure 2-2: Schematic of sun/surface/sensor remote sensing geometry, defining the angles as viewed from the surface target. The solid lines (and curves) represent solar zenith θ_0 and satellite view zenith $\theta_s = \theta$ angles (measured from the zenith, Z). The dashed lines (and curves) represent the relative azimuth angle ϕ (measured from the extension of the solar azimuth), and the dotted lines (and curves) represent the scattering angle Θ (measured from the extension of the direct beam). The Terra icon is from the Earth Observatory (http://earthobservatory.nasa.gov). Glint Angle, not shown, means the angle difference from specular reflectance.

Since aerosol retrieval is primarily a problem of reflected radiation, it is easier to deal with equations in terms of reflectance. For now, let us assume that our observation is in a "window" region of the electromagnetic spectrum, so there is no gas absorption. The normalized spectral radiance, or reflectance, ρ_λ is defined by

$$\rho_\lambda = L_\lambda \frac{\pi}{E_{0,\lambda}\,\cos\theta_0}. \qquad \text{Eq. 2-25}$$

The upward reflectance (normalized solar radiance) is a function of successive orders of radiation interactions within the coupled surface-atmosphere system. It includes scattering of radiation within the atmosphere (the 'atmospheric path reflectance'), transmission of radiation down to the surface, reflection off the surface that is transmitted to the sensor (the 'surface function'), and reflection of radiation from outside the sensor's field of view (the 'environment function'). The environment function is neglected so that to a good approximation, the theoretically TOA reflectance ρ_λ^* (in a clear sky and window wavelength – no gases), for a given atmospheric total optical depth ($\tau_\lambda^a = \tau_\lambda^{aer} + \tau_\lambda^R$) can be approximated by:

$$\rho_\lambda^*(\tau_\lambda^a, \theta_0, \theta, \phi) = \rho_\lambda^a(\tau_\lambda^a, \theta_0, \theta, \phi) + \frac{T_\lambda^\downarrow(\tau_\lambda^a, \theta_0)T_\lambda^\uparrow(\tau_\lambda^a, \theta)\rho_\lambda^s}{1 - s_\lambda(\tau_\lambda^a)\rho_\lambda^s}, \qquad \text{Eq. 2-26}$$

where the first term ρ_λ^a represents the atmospheric path reflectance (for the sum of aerosol and Rayleigh), and the second term represents the interaction of the atmosphere and the surface. $T_\lambda^\downarrow(\theta_0)$ and $T_\lambda^\uparrow(\theta)$, are the atmospheric transmissions (function of zenith angles) from TOA "down" to surface and from surface "up" to observation, s_λ is the 'atmospheric backscattering ratio' (diffuse reflectance of the atmosphere for isotropic light leaving the surface), and ρ_λ^s is the 'surface reflectance' [*Kaufman et al.*, 1997a], which for now we assume to be Lambertian. Since our light source is the sun (outside of the TOA), we recognize that the downward transmission (direct + diffuse) is the also the downward

flux received at the surface, which might be referred to as F_{dn}. Also, note that when our observation is also the TOA (e.g., a satellite), the surface is Lambertian, and the satellite and sensor zenith angles are equal ($\theta_0 = \theta$), then $T_\lambda^\downarrow = T_\lambda^\uparrow$ (known as reciprocity). Reciprocity does not hold when our sensor is on an aircraft below the TOA.

Note that in case of a near-black surface in a particular wavelength ($\rho_\lambda^s = 0$), the second term can be neglected.

2.2. "Dark-target" Retrieval Strategy

Let us assume that in addition to molecular (Rayleigh) components, the observed reflectance includes contributions from two aerosol "types". One is dominated by fine-sized particles ("fine model"), the other dominated by coarse-sized particles ("coarse model"). Let us define the contribution of the fine model as the *fine-model weighting* (FMW or η), in order to write:

$$\rho_\lambda^* = \eta\rho_\lambda^{*,f} + (1-\eta)\rho_\lambda^{*,c} \qquad \text{Eq. 2-27}$$

Here, the *f* and *c* refer to <u>f</u>ine and <u>c</u>oarse aerosol models, and η is independent of wavelength. The reflectance contribution from one of these aerosol models, is in-turn defined by that model's particle scattering properties (size & shape distributions, spectral complex refractive index – resulting in scattering phase matrix), the aerosols' total loading and vertical profile, as well as coupling interactions with the vertical profile of Rayleigh scattering). The transmission/surface contribution also depends on the aerosol model and its coupling with Rayleigh. The angular dependence (noting removed subscripts in Eq 26) also depends on these properties (via coupling of aerosol and Rayleigh phase matrices in the vertical).

Now let us assume that there are limited choices for aerosol model types *j*, so that given assumptions about the aerosol model *j*'s optical properties, total loading and vertical profiles, coupled with Rayleigh optical properties, one can use Radiative Transfer (RT) codes to simulate the path reflectance and surface interaction terms. This is the basis for a lookup table (LUT) that can be expanded to represent any number of aerosol models (*j*), aerosol loadings (τ), and vertical profiles. RT can also compute reflectances observed at any combination of angles ($\theta_0, \theta,$ and ϕ). To differentiate from other types of LUTs, we consider these to be Reflectance-versus-aerosol (RvA) tables.

We want to solve Eq 26 by matching the RvA LUT and the actual observations. The issues are that each observation by our sensor is for a single geometry only, and that the atmosphere and surface both contribute to the TOA. The trick is to attempt retrieval over surfaces which appear "dark" (near zero surface reflectance) in one more wavelengths, so that the second term becomes negligible. The other trick is to define aerosol models (*f* and *c*) which might be observed on Earth, and to limit the retrieval space to pick those most-likely to be observed.

To summarize, the principles of our DT aerosol retrieval include:
- Use a sensor having wavelengths which are "window" wavelengths (minimal gas absorption) and span the visible, NIR and SWIR regions. We expect that the surface reflectance in some of these wavelengths should be near-zero or well-estimated.
- Define aerosol optical models (size & shape distributions, spectral complex refractive index, vertical profiles) which broadly represent known aerosol types for the specific scene or conditions.
- For each of *j* aerosol models, use particle scattering and radiative transfer codes to derive LUTs simulating path reflectance and atmospheric transmission terms. The LUTs account for coupling between the vertical profiles of aerosol and Rayleigh components and are computed for discrete values of total aerosol loading. Nodes are defined as the AOD at 0.55 mm, with LUT reflectance calculated for all wavelengths. Rayleigh is a function of wavelength only

(independent of aerosol). The surface contribution may be implicitly assumed (over land) or explicitly calculated (over ocean).

- o Over land, there are j=5 aerosol models, with 3 being fine-dominated and 1 being coarse.
- o Over ocean, there are j=9 models, 4 are fine and 5 are coarse.
- For a given suitable, clear-sky observation (observed spectral reflectance with angles), interpolate the LUT to find the combination of fine and coarse models, FMW, and AOD (at 0.55 µm) that leads to a modeled spectral reflectance which "best" matches the observations.
- Derive additional parameters (such as Ångstrom Exponent, α), as well as diagnostics (such as Quality Assurance and Confidence) which describe useful properties and the ability of the retrieval to find a successful solution which is appropriate and physically relevant.

The overall strategies for DT performed over land (DT-L) and ocean (DT-O) are generally similar in concept. However, since ocean and land have such different optical properties, their assumptions and mechanics differ greatly. This ATBD will delve into each flow path. Of course, the other major challenge for aerosol retrieval is deciding which surface targets to retrieve over. The dark-target aerosol retrieval is a clear-sky algorithm, and there are clouds everywhere. There are also bright natural (ice/snow, deserts) and unnatural (urban and built-up) surfaces which tend to be inappropriate for retrieval. Therefore, cloud masking and pixel selection strategies are important components to the aerosol retrieval.

3. Characteristics of the Sensors and Reflectance/Radiance Data

Table 3-1 provides information characteristics of the sensors currently used for DT aerosol retrieval, including the dates of mission, equator crossing time (if LEO) or the longitude at the equator (if GEO), their swath width, number of wavelengths, spatial resolution of the blue (lower resolution) or red (often higher resolution) wavelength bands, the nominal granule or full disk (FD) pixel size. **Table 3-2** describes wavelengths and channels used in DT retrieval.

TABLE 3-1: SENSORS USED FOR DT RETRIEVAL.

Sensor	MODIS		VIIRS		ABI			AHI		eMAS	
Platform	Terra	Aqua	SNPP	NOAA20	GOES16	GOES17	GOES18	H08	H09	SEACR4s	FIREX
Dates	Feb 2000 - present	Jul 2002 - present	Nov 2011 - present	Mar 2019 - present	Aug 2017 - present	Dec 2018 – Dec 2022	Jan 2023 - present	2015 – Dec 2022	Dec 2022- present	Aug-Sep 2013	Aug 2019
Eq crossing	10:30 (descend)	13:30 (ascend)	13:30 (ascend)	13:30 (ascend)	75.0°W	137.2°W	137.0°W	140.7°E		N/A	N/A
Altitude (km)	705		824		36K			36K		~18	~20
Orbits/day	14.5		14		N/A			N/A		N/A	N/A
Ground target at equator	<1/day		1/day		144/day			144/day		N/A	N/A
Swath width (km)	2330		3040		FD			FD		37	37
Field of view	±55°		±56°		±8°			±8°		±43°	±43°
Number of Wavebands	36		22		16			16		38	38
Blue / Red band pixel size at nadir (km)	0.5 / 0.25		0.75 / 0.375		1.0 / 0.5			1.0 / 0.5		0.05 / 0.05	0.05 / 0.05

Granule size in pixels (X × Y) / cadence	2708 × 4080 (5 min)	3200 × 3232 (6 min)	10848 × 10848 (10 min)	11000 × 11000 (10 min)	716 × Varies	716 × Varies
Scan lines per scan	20	8	1000	1000	1	1
BowTie?	Yes	Corrected	No	No	No	No
N×N aggregation (of blue band)	20×20 or 6×6**	8×8	10×10	10×10	10×10	10×10
DT Product resolution at nadir (km)	10×10 km or 3×3 km**	6×6 km	10×10 km	10×10 km	0.5×0.5 km	0.5×0.5 km

** "standard" MODIS products are at 10×10 km resolution, there is also a 3×3 km version

TABLE 3-2: WAVELENGTHS USED FOR DT RETRIEVAL:

Band	MODIS		VIIRS-SNPP		VIIRS-NOAA20		ABI-GOES16		ABI-GOES17 & 18		AHI-H08 & H09		eMAS-SEACR4s		eMAS-FIREX	
	B#	Wave	B#	Wave	B#	Wave	B#	Wave	B#	Wave	B#	Wave	B#	Wave	B#	Wave
DarkBlue	B8	0.412	M1	0.411	M1	0.411										
Blue	B3	0.466	M3	0.486	M3	0.488	G1	0.471	G1	0.471	H1	0.470	E01	0.467	E01	0.474
Green	B4	0.554	M4	0.551	M4	0.558					H2	0.510	E02	0.550	E02	0.556
Red	B1	0.645	M5/I1	0.671/0.637	M5/I1	0.667/0.648	G2	0.639	G2	0.639	H3	0.640	E03	0.655	E03	0.661
NIR	B2	0.857	M7	0.862	M7	0.868	G3	0.864	G3	0.864	H4	0.856	E07	0.865	E07	0.870
NIR1	B5	1.242	M8	1.238	M8	1.238										
SWIR1	B6	1.630	M10	1.601	M10	1.604	G5	1.610	G5	1.609	H5	1.610	E10	1.605	E10	1.613
SWIR2	B7	2.114	M11	2.257	M11	2.258	G6	2.243	G6	2.242	H6	2.257	E20	2.126	E20	2.133
Cirrus	B26	1.382	M9	1.375	M9	1.375	G4	1.37	G4	1.37			E15	1.874	E15	1.881
TIR1	B29	8.6	M14	8.5	M14	8.5	G11	8.4	G11	8.4	H11	8.6	E30	8.417	E30	8.417
TIR2	B31	11.	M15	11.	M15	11.	G14	11.2	G14	11.2	H14	11.2	E34	11.9	E34	11.9

3.1. MODIS Instrument

The MODerate resolution Imaging Spectrometer (MODIS) instrument flies on the Earth Observation System's (EOS) Terra and Aqua satellites. Both satellites are in polar-orbiting, sun-synchronous, Low Earth Orbit (LEO), with Terra descending (southward) over the equator about 10:30 local sun time (LST), and Aqua ascending (northward) over the equator about 13:30 LST. From a vantage 705 km above the surface and a ±55° view scan, each MODIS instrument views a swath about 2330 km. Each day, MODIS makes ~14.5 orbits (99 minutes per orbit), observing nearly the entire globe. There are small gaps at the equator, so full coverage takes about 3 days. Orbit patterns repeat every 16 days.

MODIS performs measurements in 36 spectral channels (or bands) that cover the solar to thermal infrared spectrum region between 0.41 to 14.2 μm [*Salomonson et al., 1989*]. Nominal pixel resolutions (at nadir) are 0.25 km (for 2 bands), 0.5 km (for 5 bands) and 1 km (for 29 bands). Detailed specifications and components can be found at http://modis.gsfc.nasa.gov. For the DT aerosol retrieval, we rely on window (small gas absorption) Bands 1 through 7 (B1-B7), with "centroid" wavelengths calculated as in Table 3b. B1 and B2 (red and NIR) are observed at 0.25 km resolution, with B3-B7 (blue, green, NIR1, SWIR1 and SWIR2) at 0.5 km resolution. For cloud masking and other purposes, we also use 1 km resolution B26 (cirrus band in the SWIR) as well as B29 and B31 in the Thermal infrared (TIR). The copies of MODIS on Terra and Aqua are similar

enough that we can use the same centroid wavelengths (within 1 nm) to describe both instruments. (see Appendix 1 for details of calculations).

MODIS is not a "camera", rather it makes use of a continually rotating scan mirror. Each scan of the mirror images 10 lines of 1 km pixels, (20/40 lines of 0.5/0.25 km pixels). Because of the 55° swath convolved with Earth's curvature, 1 km pixels grow to approximately 4.8 by 2.0 km at swath edge. This gives rise to the geolocational oddity known as the panoramic "bow-tie" effect that means the scans are partially overlapping towards swath edge. For simplification, pixel size will refer to nadir pixel size, unless stated otherwise.

3.2.   VIIRS Instrument

The Visible Near Infrared Radiometer Suite (VIIRS) was launched aboard Suomi-NPP in 2011, on NOAA-20 in 2017, on NOAA-21 in 2022, and on future NOAA Joint Polar Satellite System (JPSS-3 and 4) satellites. All VIIRS copies are at elevation of ~825 km with ascending equator crossings around 13:30 LST. With a higher altitude and slightly wider view ±56°, each VIIRS observes a 3040 km wide swath which entirely covers the globe (no gaps) with ~14 orbits per day. NOAA-20 is placed a half-orbit behind SNPP (50 minutes), so crosses the equator at the same LST but to the west.

Like MODIS, VIIRS is multi-spectral, but with only 22 bands (covering 0.41 to 12.3 μm). Nominal spatial resolution for the 5 "Imagery bands" (I-bands; I1-I5) are at 0.375 km, with the remaining "Moderate bands" (M-bands; M1-M16) and the DayNightBand (DNB) at 0.75 km. The DT retrieval (in daylight) makes direct use of wavelengths described in Table 3b, which are generally similar as those to MODIS. These include window bands (M3, M4, M5, M7, M9, M10 and M11), cirrus reflective band (M8), and TIR bands (M14 and M15). Beginning with Version 2, DT is making use of the I2 (red wavelength I-band) to help with cloud masking. Note that unlike MODIS on Terra and Aqua, the copies of VIIRS on SNPP and NOAA-20 differ slightly in their wavelength spectral response, leading to differences of 3-5 nm in some bands. VIIRS on NOAA-21 is nearly identical to that on NOAA-20.

VIIRS is similar in technology to MODIS in that it uses a scanning mirror and is hampered by bow-tie effect and pixel overlap. However, VIIRS onboard processing is such that it partially compensates for the bow-tie effect, by deleting bow-tie influenced scans through a "pixel trim" (see this link). For SNPP these data cannot be recovered, but they can be estimated by substituting nearest-neighbor pixels using a code package called viirsmend. The viirsmend package developed at the University of Wisconsin – Madison SSEC, and implemented on the NASA VIIRS Atmosphere SIPS, replaces deleted bow-tie pixels with the nearest valid pixel for each reflectance band in VIIRS L1b. This is defined using Earth-Centered, Earth-Fixed (x, y, z) coordinate space, to avoid adverse effects around the poles and international date line. All L2 VIIRS Dark Target products perform viirsmend bow-tie restoral on both imagery and moderate-resolution bands as a first step in the retrieval process.

3.3.   ABI Instrument

Advanced Baseline Imagers (ABI) were launched upon GOES-R (became GOES-16 on orbit) in 2017, GOES-S (GOES-17) in 2019, and GOES-T (GOES-18) in 2022. GOES-16 became NOAA's operational GOES-East (over equator at 75.0°W), whereas GOES-17 became GOES-West (137.0°W). After a period of overlap at GOES-West position between June 2022 and December 2022, GOES-18 became the operational GOES-West, with GOES-17 moving into "storage" near 105°W. All three GOES satellites operated at a "checkout" position (near 87°W) for some time before moving into operational positions. From an altitude of ~36,000 km, each ABI carves out a scan pattern that includes mesoscale, continental, and full-disk (FD) defined areas. Prior to April 2019, the scan pattern

took 15 minutes, but is now 10 minutes (see [this link](#)). Each ABI makes 144 FD scans per day, observing hemisphere with radius approximately 82° in longitude/latitude (local zenith angle). Currently, DT runs on FD,

ABI observes at 16 wavelength bands, covering a range of VIS though TIR. Table 3b lists the wavelengths used for DT. Analogous to MODIS or VIIRS, GOES-ABI has blue, NIR and SWIR1 bands (G1, G3 and G5) at 1 km resolution, red band (G2) at 0.5 km resolution, and the remaining bands at 2 km resolution. There is no Green or NIR1 bands, so the DT algorithm must include compensations.

Each FD image is approximately 10848 × 10848 pixels (for the 1 km resolution). Pixel-overlap (bow tie) is not a problem for a GEO imager, however, pixel sizes toward FD limbs increase greatly (For details of ABI pixel size change please refer to [this link](#)).

3.4.   AHI Instrument

Advanced Himawari Imagers (AHI) were launched on Japan's Himawari-8 (H08) satellite in 2015 and on Himawari-9 (H09) in 2016. Both are located near 140.7°E. H08 was operational until December 2022 when it was replaced by H09. H08 is currently in storage, standby orbit. Like ABI, AHI carves out a scan pattern that includes FD imagery every 10 minutes.

Like ABI, AHI also observes 16 wavelength bands, however instead of the 1.37 μm "cirrus" band AHI included a 0.51 μm Green band. All other bands are similar to ABI. Thus DT retrieval uses H1, H2, H4 and H5 at 1 km resolution, H3 (Red) at 0.5 km resolution, and the remainder at 2 km resolution. The FD is slightly larger, covering 11000 × 11000 pixels (for the 1km resolution).

3.5.   eMAS Instrument

The Enhanced MODIS Airborne Simulator (eMAS; https://asapdata.arc.nasa.gov/emas/index.html) is an airborne scanning spectrometer that acquires high spatial resolution imagery of cloud and surface features from a NASA ER-2 high-altitude research aircraft. Used primarily during field campaigns, the eMAS spectrometer acquires high spatial resolution imagery in 50 bands, within the range of 0.47 to 14.3 μm. From the nominal airborne vantage of 20 km, eMAS observes a 37.5 km swath with nadir pixel resolution of 50 meters. An eMAS "flight track" image is created from a segment of level and straight-line flying during a campaign flight. Although always 716 pixels wide (across-track), flight track granules vary in length. As the gratings and mechanics may be reset due to shipping or flight, eMAS is calibrated by NASA's Ames Research Center (ARC) for each campaign. As a result, the spectral response of each band may shift by ~5 nm from campaign to campaign and noted accordingly in **Table 3-2**. Note that like the GEO sensors, there is no NIR1 band near 1.24 μm. Also, there is no 1.37 μm band. However, as noted by Meyer et al. [*2016*], measurements near 1.88 μm provides a very good alternative for detecting cirrus.

3.6.   Aggregation vs Signal to Noise (SNR)

Passive imagers measure electronic photon counts, that when calibrated against known reflective sources, one can convert to reflectance units (Eq. $\rho_\lambda = L_\lambda \frac{\pi}{E_{0,\lambda} \cos \theta_0}$.   Eq. 2-25). To be useful for aerosol retrieval, the instrument must be spectrally stable and sufficiently sensitive. For MODIS, the spectral stability for each instrument is said to better than 2 nm ($0.002 \ \mu m$). The 'Noise Equivalent Differential Spectral Radiance' is a property of the instrument, which can be converted to reflectance units as $Ne\Delta\rho$. 'Signal to Noise Ratio' (SNR) is defined as the ratio of the 'typical scene reflectance" to its noise. The $Ne\Delta\rho$ and the SNR specifications for MODIS B1-7 (at their nominal resolution) are

typically in the range of 3×10^{-4}. To be understood in the framework of aerosol remote sensing, the definition of SNR should be based on the expected aerosol signal. Therefore, a 'Noise Equivalent Differential optical depth' ($Ne\Delta\tau$) is:

$$N_e\Delta\tau = \pi N_e\Delta\rho \frac{4\cos(\theta_0)\cos(\theta)}{\omega_0 P(\Theta)} \qquad \text{Eq. 3-1}$$

where θ_0 and θ are the solar and view zenith angles, ω_0 is the aerosol single scattering albedo and $P(\Theta)$ is the aerosol phase function as a function of scattering angle. The least sensitivity to aerosol scattering optical depth (largest noise) is expected when both sun and satellite are at nadir views ($\theta_0 = \theta = 0.0$), the phase function is a minimum ($\Theta \sim 120°$) and the channel used is the least sensitive to the aerosol (generally the longest wavelength e.g. SWIR2). With a typical phase function value of 0.08 at 120°, a typical aerosol scene has $N_e\Delta\tau \sim 1.5 \times 10^{-2}$. The SWIR2 channel is also where the 'typical scene τ' is (τ^{ts}) is 0.01 or less. Therefore, the SNR ratio defined by the ratio of $\tau^{ts}/N_e\Delta\tau$ is about 0.65. If one requires SNR > 10, then the single 0.5 km pixel is insufficiently sensitive to characterize aerosol. However, if individual pixels are aggregated to larger areas, say to a box of 10 × 10 km² (20 × 20 pixels) then the SNR is increased significantly (SNR = 260). However, in many cases not all pixels are suitable for retrieval (clouds, glint, not dark surface), so SNR is usually less. For noise reduction, the DT aerosol retrieval is performed at N × N pixel aggregation. For MODIS specifically, increase of SNR and the need to keep scan lines together leads to 20 × 20 aggregation (or 10 × 10 km). In general, VIIRS has better SNR than MODIS (see this link), so that 8 × 8 aggregation (or 6 × 6 km) keeps scan lines together, and is sufficient for DT retrieval. In fact, DT uses N × N aggregations of native resolution for all sensors as shown in **Table 3-1**.

4. Inputs and Processing Environment for DT aerosol Retrieval

4.1.   Level 1B Calibrated Radiances / Reflectances and Geolocation

The DT aerosol algorithms rely on calibrated reflectance and radiance data (known as 'Level 1B' or 'L1B'), provided in files that represent a specific location and time length. For the GEO imagery, this means Full Disk with 10-minute cadence. For the LEO imagery (MODIS and VIIRS), along-orbit swath data are chunked into granules which represent 5 and 6 minutes, respectively (**Table 3-1**, **Table 3-2**). For the airborne (eMAS), data are chunked into flight tracks with variable time lengths. For MODIS, VIIRS and eMAS, the L1B includes both the reflectances/radiances as well as geolocation (latitude/longitude, observation geometry, land/sea mask, and diagnostic information). For the fixed-projection geostationary (ABI and AHI), we compute the geolocation information as part of the retrieval.

MODIS

MODIS raw data are provided as 5-minute granules, which represent an along-track path of 2030 km (203 "scans"). A nominal granule size of 2300 km swath by 2030 along track is thus 2708 by 4060 pixels at 0.5 km (1354 × 2030 at 1km and 5416 × 8120 at 0.25 km). These raw data are calibrated by the MODIS Characterization Support Team (MCST) and processed into L1B by NASA's MODIS Adaptive Processing System (MODAPS). The MODIS L1B data can be found in archives at NASA's Land and Atmosphere Distribution System (LAADS). These are identified as products MOD02 for Terra and MYD02 for Aqua (MCST 2000; MCST 2002). Here, either 'MOD' or 'MYD' will be denoted by 'MxD'. DT uses L1B reflectances at three resolutions (MxD021KM, MxD02HKM and MxD02QKM for 1km, 0.5km and 0.25km resolution channels, respectively). Currently, all L1B data

are served in 'Hierarchical Data Format version 4' (HDF4 - http://hdf.ncsa.uiuc.edu). However, there are plans for future L1B to be served in Network Common Data Format version 4 (NetCDF-4) which is compatible with HDF5. Details of MODIS L1B are found in this link.

MODIS Geolocation files are known as MxD03 and represent the MxD021KM (1 km) pixels. Information includes latitude/longitude, observation angles (satellite and sensor, zenith and azimuth), as well as information about the MODIS sensor and the spacecraft. Additionally, the MxD03 files provide categorical description of the surface type known as the EOS Land/Sea Mask, and estimates of the land terrain height. The EOS Land/Sea Mask, which can be found here, is based on the Global 250m Water Map [*Carroll et al, 2017*], and takes on these values:

   0: Shallow Ocean (Ocean < 5k from coast OR < 50m deep).
   1: Land (not anything else).
   2: Ocean Coastlines and Lake Shorelines.
   3: Shallow Inland Water (Inland Water < 5km from shore OR < 50m deep).
   4: Ephemeral (intermittent) Water.
   5: Deep Inland Water (Inland water > 5km from shoreline AND > 50m deep).
   6: Continental Ocean (Ocean > 5km from coast AND > 50m deep AND < 500m deep).
   7: Deep Ocean (Ocean > 500m deep).

Note that EOS Land/Sea Masks and terrain heights are static for the entire Terra and Aqua missions. DT uses this information to select whether to head down the DT-O or DT-L paths. To determine geolocation information for higher resolution (e.g., 500 m or 250 m), one can interpolate using the MODIS "point spread function" described in the MxD03 ATBD (see this link)

VIIRS

VIIRS raw data are initially processed by NOAA's ground systems. However, for compatibility with the Cross-track Infrared Sounder (CrIS) data products (which is on SNPP and every JPSS mission), NASA's implementation of VIIRS granularity is 6 minutes. In addition, NASA has developed their own algorithms for calibration, geolocation and diagnostics (via the VIIRS Characterization Support Team or VCST), leading to differences between NASA's L1B (archived at LAADS) and NOAA's versions (accessed via their Comprehensive Large Array-Data Stewardship System-CLASS). Details about NASA's VIIRS L1B are here. The M-band resolution (0.75 km) geolocation and radiance, known as Vx03MOD and Vx02MOD (VNP for SNPP and VJ1 for JPSS1/NOAA20), have nominal resolution of 3200 × 3232 pixels. The I-band (Vx03IMG and Vx02IMG) files are also used by DT. All files are archived in NetCDF-4 format at LAADS. The VIIRS geolocation (Vx03) use the same upstream EOS Land/Sea Mask and terrain height upstream information as MODIS. Note that with both Vx03MOD and Vx03IMG, there is no need to interpolate geolocation information from lower resolution (M-Bands) to higher resolution (I-bands).

ABI

ABI data (from raw to L1B) are processed entirely by NOAA's ground systems, with standard availability through NOAA's CLASS system. Duplicate data are copied to NASA's systems from which DT can process. L1B files are in NetCDF-4 format, and rather than grouped by resolution as MODIS or VIIRS, they are single channel only as 'OR_ABI-L1b-RadF-M6Ccc_Gxx' where 'cc' is the GOES-ABI band number and 'xx' is '16', '17', or '18'. Note that there is no specific "geolocation" file as there is for MODIS or VIIRS, so that the geolocation (latitude/longitude, observation geometry/angles) is calculated for each FD image. Although the projection on the Earth is fixed (e.g. 75.0°W or 137.0°W for GOES-East and GOES-West, or 87.5°W for checkout position), the actual

subsatellite longitude may vary by ~ 0.2°. That value is noted in the L1B files, and a NOAA-provided code (fgf_to_earth) is used for the geolocation calculations.

AHI

AHI data are processed via JMA's ground system, leading to files in Himawari Standard Data (HSD) format. Through agreements between NOAA, NASA and JMA, these HSD are available for U.S. research and forecasting. Based on readers provided by JMA, the University of Wisconsin's Space Science and Engineering Center (SSEC) has developed a tool (nominally known as HSD2NC), that converts to NetCDF-4 files analogous to those provided via NOAA-CLASS known as 'OR_AHI-L2-CMIPF-M1Ccc_GHx' (where the cc is the AHI band number and 'x' is '8' or '9'). Using the Himawari projection longitude (140.7° E) and the actual subsatellite longitude point, the same code is used to derive the geolocation information.

EMAS

The Enhanced MODIS Airborne Simulator (eMAS) is an airborne sensor that is very similar to the MODIS sensor [*King et al., 1996*] and flies on a NASA ER-2 high-altitude research aircraft. The sensor is maintained and operated by the Airborne Sensor Facility (ASF) at NASA Ames Research Center under EOS Project Science Office at NASA Goddard. eMAS Level 1 and Level 2 data are distributed via MODIS science team via LAADS web portal.

4.2.   Upstream Cloud Mask

The primary strategy for cloud masking (discussed in Appendix 3) is based on assessing the magnitude and variability of reflectance in 3 × 3 pixel groupings. However, there is significant information about clouds in the TIR wavelengths. Therefore, DT makes use of that information. For both MODIS and VIIRS, cloud mask files produced by the "Wisconsin" cloud mask team are available. For MODIS, we use the selected tests (Thin Cirrus Detected (infrared), Cloud Flag - IR Temperature Difference, high Cloud Flag - 6.7 μm Test) provided by the MxD35 cloud mask (Cloud Mask MODIS user guide) and for VIIRS, we use the CLDMSK_L2 file (MVCM user guide). For VIIRS only two tests are applied: Thin Cirrus Detected (infrared) and Cloud Flag – IR, due to missing channels within VIIRS. These Level 2 (L2) cloud mask files are at nadir resolution of 1 × 1 km for MODIS and 0.75 × 0.75 for VIIRS. If available, DT uses cloud mask files that are created as part of the eMAS processing. DT retrievals for ABI and AHI do not use an upstream cloud mask file.

4.3.   Ancillary Meteorological Data for Gases and Wind Speed.

Although the DT algorithm uses wavelength bands that are considered "window" wavelengths, absorption by gases is not zero. Depending on sensor response, different trace gases may more or less influence the total absorption, and that the total absorption is correlated with the total column concentrations of the individual trace gas. Patadia et al. [*2018*] introduced a strategy to parameterize trace gas absorption, which yields formulas with coefficients contained in a LUT. Essentially, the correction assumes that except for water vapor and ozone, most other trace gases are relatively homogenous on a global scale, and therefore the global average correction is applied. However, as H2O and O3 columns can vary widely (by 50% for ozone and by order of magnitude for H2O), accurate corrections require knowledge of these values.

At the same time, DT-O requires accurate estimate of the ocean's surface reflectance.   Over the open ocean (far from coastlines and land surfaces), reflectance from whitecaps, foam, and glitter (Cox & Munk, 1954, Koepke, 1984) is highly correlated with surface wind speed.

Values of column water vapor, ozone and surface wind speed can be supplied my ancillary meteorological datasets. For Collection 6.1 of MODIS (C61 = current version), this ancillary information comes from the Global Data Assimilation System (GDAS) run by the NCEP (National Center for Environmental Prediction), specifically, the GDAS1 1° × 1° 6-hourly re-analysis in WGRIB format (see this link). For standard VIIRS products, and all MEaSUREs XAERDT products (MODIS, VIIRS, ABI and AHI), this ancillary data comes from the Goddard Earth Observing System Model-Version 5 (GEOS-5) run by the Goddard Modeling and Assimilation Office (GMAO). The specific GEOS-5 data is known as FP-IT (Forward Processing for Instrument Teams, Lucchesi, 2013) and is provided at 0.5°×0.625° and 3-hourly intervals. The DT team intends to use GMAO-provided data for future MODIS versions (e.g. Collection 7).

For all standard processing, DT uses the meteorological re-analysis closest in time to the start time of the granule, FD or flight track. However, if there is no re-analysis available, DT can be run using climatology (e.g., US-76 atmosphere and assumed 6 m/s wind speed). DT also can use "forecast" fields instead of re-analysis. Currently, both MODIS (C61 algorithm) and VIIRS (Version 2 algorithm) can be run in Near-Real-Time (NRT), thus using the most recent forecast available for the granule's start time.

4.4.   DT-specific LUTs

The DT algorithm requires pre-computed lookup tables (LUTs), including some that are sensor specific.

4.4.1. Coefficients for Trace Gas Corrections

Satellite-measured TOA radiance comes from the atmosphere as well as the underlying surface. Atmospheric contribution of TOA radiance comes from the interaction of solar radiation with atmospheric constituents such as aerosols, clouds, and atmospheric gases. AOD retrievals based on satellite measured TOA radiance require isolating the aerosol contributions from the total observed signal.

Multispectral AOD retrieval algorithms use signals from carefully selected wavelength bands in the "atmospheric window" region where absorption by atmospheric gases is minimal. Even though little, the absorption of radiation by atmospheric gases in these wavelength regions can't be ignored and therefore need to be corrected. High-resolution TRANsmission (HITRAN) database and Line-By-Line Radiative Transfer Model (LBLRTM) are used to derive atmospheric gas correction coefficients at specific wavelength bands to address absorption by water vapor, carbon dioxide, ozone, and other trace gases. The empirical gas correction constructed for one sensor cannot be applied to another sensor even when the wavelength bands of the two sensors are similar. Please see Appendix 1 for details.

4.4.2. Reflectance-versus-Aerosol (RvA) for DT-L and DT-O

The core of the DT retrieval algorithm is the Reflectance-versus-aerosol (RvA) tables, which are sensor-specific. These are created separately for DT-L and DT-O, using different combinations of aerosol scattering and radiative transfer (RT) codes. Each RvA table is similar in content, in that they provide Top-of-Atmosphere (TOA) reflectance (or normalized radiance) for different combinations of molecular scattering (Rayleigh) aerosol "types" (optical models), aerosol loading (vertical profiles of particle concentrations), and surface properties (e.g., land or ocean surface reflectance). The DT-O LUT has an additional dimension of surface wind speed (which defines the surface reflectance). Calculations are provided at discrete observation angles (combinations of solar zenith, sensor zenith and relative azimuth angles), and for the specific wavelengths of the given sensor. Each LUT is

presented as an ASCII file which must be read by formatted "read" statements. Details about the creation and content of the RvA LUTs are presented under DT-O and DT-L separately.

4.4.3. Prescribed Aerosol Type and Urban Percentage for DT-L

Due to having less information content than DT-O, the DT-L retrieval uses two additional LUTs. The first is an assignment of aerosol type. Based on cluster analysis of ground-based sunphotometer retrievals, Levy et al., [*2007*] derived a prescription of expected aerosol "type", based on season and location on a 1° x 1° latitude/longitude grid. This information is used to subset the RvA table during the DT-L retrieval. This aerosol-type LUT was modified for use for MODIS Collection 6 (circa 2013) and is currently used for DT-L retrieval on all sensors.

The second LUT used for DT-L is an assignment of urban percentage (UP). A natural surface (e.g., vegetation and dark soil) has a well-defined relationship between surface reflectance in different wavelengths. That relationship changes with urbanization. Based on a study by Gupta et al. [*2016*], one can parameterize change of land of surface reflectance as a function of UP. Currently, the UP table is used for retrieval for MODIS C61 only, but can be used for later versions of AERDT/XAERDT on different sensors. During retrieval, the algorithm reads in the UP and modifies its estimate of surface reflectance.

4.4.4. Land Surface Elevation and Land/Sea Mask

For MODIS and VIIRS land surface and elevation are included within the L1B files. For GEO, we use offline files which were generated for the appropriate projection. Land/Sea masks and elevations for GOES satellites are provided by NOAA. Altitude data used for AHI is from standard global database while land/sea masks are re-gridded using MODIS's land product. These are static files stored in the package (ABI_EAST_GEO_TOPO_LOMSK.nc, ABI_WEST_GEO_TOPO_LOMSK.nc and static_AHI_congrid)

4.5. Retrieval Code and Production Environments

The core of the DT retrieval code (for comparing observations with LUTs) is written in Fortran (mostly -77 and -90 conventions). The DT-Package and standard MODIS C61 codes are similar, but DT-Package tends to be more modular (separated into separate routines and functions) and cleaner in terms of variable-naming conventions and efficiency. The major differences between codes are in handling inputs and outputs. For standard (C61), the MODIS L1B and L2 outputs are read and written into the heritage 'Hierarchical Data Format version 4' (HDF4 – see [link](#)). DT-Package can read files in HDF format as well as the more widely accepted Network Common Data format version 4 (NetCDF4) that are used for VIIRS, ABI and AHI. For all sensors (including MODIS), DT-Package writes as NetCDF. To read/write HDF and NetCDF files, the respective libraries must be installed within the system.

Routine standard processing is performed within auspices of one of NASA's Science Investigation Processing and Support (SIPS) centers, with MODAPS producing MODIS (C61) and the Wisconsin A-SIPS producing VIIRS (V2). Data are archived at the LAADS-DAAC. Within MODAPS, MODIS files are generated using a special set of libraries (known as the MODIS-Toolkit) which simplifies some of the common procedure calls. The DT-Package, used for all other processing, calls libraries directly.

When a SIPS or LANCE runs MODIS or VIIRS standard processing, they use their own logic for determining time stamps and staging input files (L1B, ancillary meteorology, LUTs, etc.). When run offline (on our own servers), we use scripts or other codes to determine this information. Based on

small samples of data, outputs created offline show negligible differences between files produced by a SIPS. This provides confidence that if inputs are identified and presently accessible, DT-Package can be run on any machine.

5. DT Aerosol Retrieval: Overview of Mechanics and Assumptions

Whether being used for standard routine processing of MODIS or VIIRS (via MODAPS or A-SIPS) or for catered retrieval (as applied for XAERDT, eMAS, or case studies), the DT aerosol retrieval has a generic "Main" core which includes the following major steps. These are outlined with the flowchart (Figure 5-1).
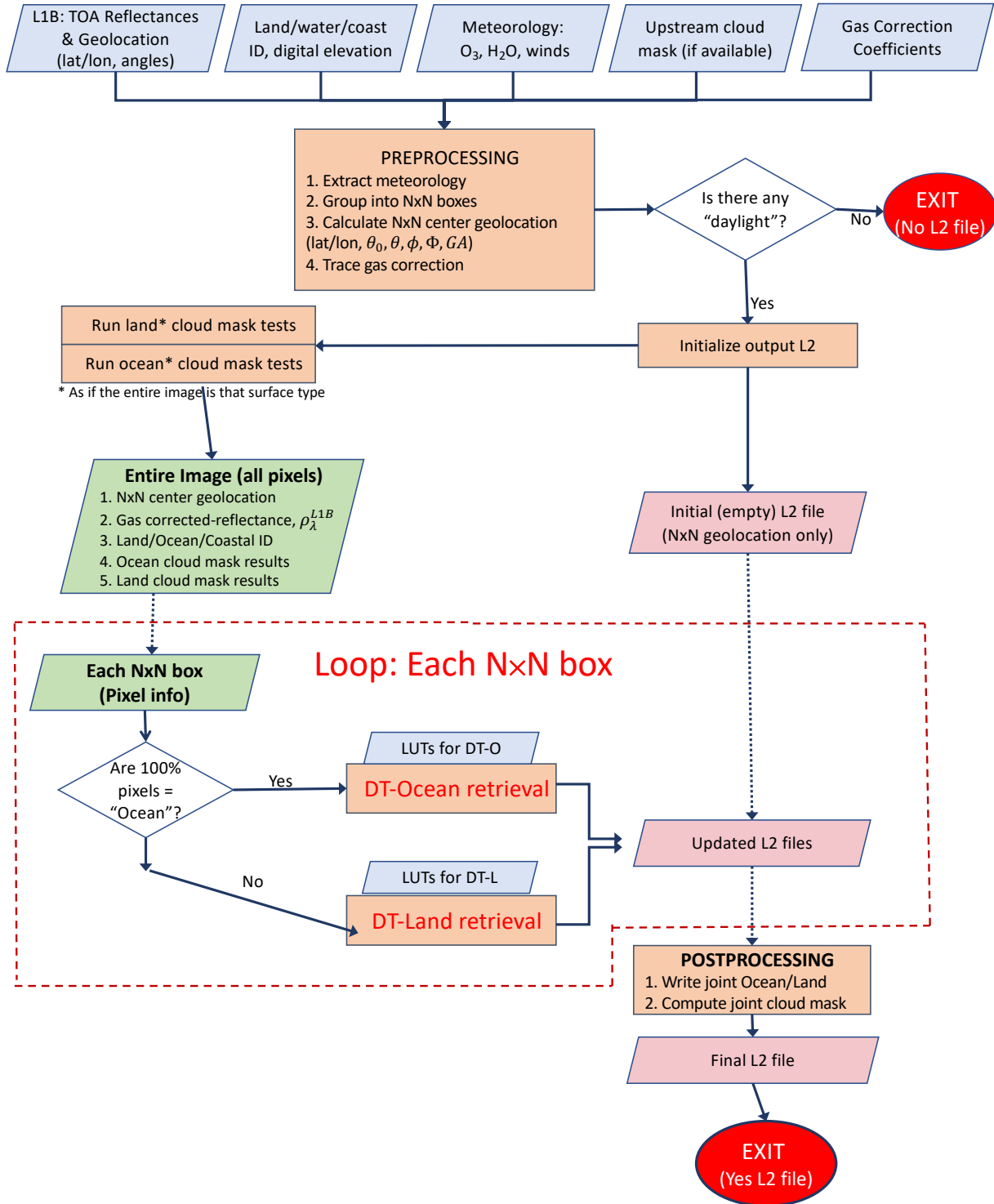
Figure 5-1. Flow chart of DT algorithm.

5.1.   Identifying Inputs and Pre-Processing

The first steps are to identify and stage the relevant inputs including L1B and ancillary (meteorological files). In general, the required meteorological analysis file is the re-analysis nearest in GMT time to the satellite observation time. Assuming all input L1B and ancillary files are valid and available, DT performs several pre-processing steps. First it reads in the required L1B, L2 and ancillary data into memory. For MODIS, this means reading in the reflectance / radiance data at 1 km, 0.5 (half) km, and 0.25 (quarter) km along with the geolocation (latitude, longitude, angles, land/sea/coast identification, land surface elevation) at 1 km. For VIIRS this means the reflectance/radiance at 0.75 km (M-band) and 0.375 km (I-band) along with similar geolocation. For MODIS and VIIRS, this also includes the cloud mask. For ABI and AHI, this means reading in the individual channels at their native resolution (whether 2 km, 1 km or 0.5 km), and using projection information to calculate their geolocation. For AHI, this also includes using the HSDtoNC code to reformat the data. Since ABI and AHI do not include a land/sea/coast flag or surface elevation within the projection, we also read in the relevant static maps (DEM) that is produced by NOAA at 100-meter resolution for elevation. The land/sea mask used for ABI/AHI is described in Section 5.4.

For MODIS C61, all input L1B data are used "as is". However, when used in the DT-Package (for XAERDT), the MODIS L1B undergo some additional processing. This includes interpolation of the 1 km resolution geolocation to 0.5 km, as well as similar interpolation of two of the 1 km resolution reflectance/radiance bands. Interpolation follows the point-spread function of MODIS focal plane views, meaning that if subsequent 0.5 km bands are represented by *a*, *b*, and *c*, and a 1 km band is represented by *B*, then *B = 0.25a + 0.5b + 0.25c*. Within the DT-Package, the GEO data (AHI and ABI), reflectance/radiance in relevant 2 km resolution bands is interpolated to 1 km. Here the interpolation is simpler, in that the value of a 2 km pixel is reported as four equal values at 1 km. No interpolation for geolocation is necessary, since it is computed via the projection algorithm. There is no interpolation required for VIIRS processing since all M-bands and geolocation are already at the same spatial resolution. There is no interpolation for eMAS, as all bands have the same spatial resolutions.

Original MODIS processing (C61 and prior) reads one scan line at a time, where each scan is made up of ten 1 km pixels along track. The 1354 swath pixels are also collected into 10-pixel boxes, so that there are 135 '10km' boxes in a swath (last 4 pixels are neglected). Each of these boxes is separately considered for aerosol retrieval. Note that each 10 km box contains $10 \times 10 = 100$ '1 km' pixels and $20 \times 20 = 400$ '0.5km' pixels (at nadir resolution). At the scan edges the number of pixels in each box remains the same, but the area encompassed in each box is more than eight times the area encompassed at nadir.

5.1.1. L1B Interpolation, Gas Correction

The DT-package reads in all pixels for the entire granule and then the data are split into N × N boxes, where the N varies depending on sensor and resolution of the individual band (**Table 3-1**). Here, regardless of sensor, the latitude, longitude, and observation geometry (angles) represent the center of a retrieval box, where the center is assumed to be the average of the values in the four middle pixels.

For each of the N × N boxes, the total water vapor, total ozone, and surface wind speed are acquired from the ancillary meteorological analysis fields from the nearest grid (or interpolated). For MODIS, there are slight differences between C6.1 and DT-Package, where for C6.1 all reflectances are used at native resolution, but for DT-Package, the 1 km resolution is interpolated into 500-meter resolution using the MODIS point-spread function. For retrieval on GEO sensors, the 2 km bands are interpolated onto 1 km. For VIIRS, there is no interpolation required. All reflectance are corrected for water vapor, ozone, and carbon dioxide (Appendix 1). Let us denote ρ_λ^{L1B} as the reflectance of a L1B

pixel, in a particular wavelength band after interpolation and trace-gas correction. These are pixels that will later be aggregated and used for N × N retrieval.

5.2.   Initial Cloud Mask

In addition to the L1B, both MODIS and VIIRS read the upstream Level 2 cloud mask file MxD35_L2 or CLDMSK_L2). Results of three "high cloud" tests are used for assessing clouds over ocean. The GEO sensors (ABI or AHI) do not have upstream cloud masks.

Without knowing the specifics of the surface type, DT runs one set of tests appropriate for detecting clouds over ocean, and a second set of tests appropriate for detecting clouds over land. These tests include "intensity" tests (reflectance, radiance or reflectance ratios compared with a value), as well as "variability" (standard deviation of 3x3 aggregates compared with a value). The results of all tests are stored in memory.   For the standard MODIS C61 (and prior MODIS Collections), these tests are run scan line by scan line, with no knowledge of the pixels from the previous or subsequent scan lines. For standard VIIRS Version 2, and all other instances using DT-Package (MODIS, ABI, AHI), the cloud mask is performed on the whole granule at once. Details of the cloud mask tests are given in Appendix 3.

5.3.   Check for Daylight and Initialize L2 File

Daylight condition is using upstream L1B data provided daylight flag for both MODIS and VIIRS. For ABI and AHI, solar zenith angle (θ_0) is calculated. Pixels with $\theta_0 < 84^{\circ}$ is considered daylight.

5.4.   Surface Selection and Flow into Retrieval

After all the preprocessing and the initial cloud masking, we have a full image (granule, full disk, or flight track) containing N × N groupings of geolocated, calibrated, gas-corrected reflectances. Looping through each N × N box, the next important decision is whether to go to land (DT-L) or ocean (DT-O). If MODIS or VIIRS, based on the EOS Land/Sea Mask, DT assumes that pixels marked 0, 3, 5, 6 or 7 are likely to be "water", whereas pixels marked 1, 2 or 4 are likely to be "non-water". If all pixels (100%) within the N × N box are considered water, the algorithm proceeds with the over-ocean retrieval. The rest pixels goes to the over-land algorithm. Note that there are opportunities within DT-Land to filter out pixels that appear to be water, and within DT-O to filter out pixels that appear to be land, sedimented, or otherwise too shallow to be retrieved as ocean. Eventually, "how many pixels are valid?" will influence the expected quality or confidence in the retrieval.

For AHI imager, the land/water masks are derived from MODIS Land Cover Type product (MCD12Q1) at 1 km resolution. For ABI, the masks are generated from GOES-R IP data which is based on 1km MODIS global land cover product produced by University of Maryland (see this link).

Details of the individual retrieval paths (DT-O versus DT-L) are presented in Sections 6 and 7.

5.5.   Postprocessing: Quality Assurance and Level 2 'Combined'

During aerosol retrieval on a particular N × N box, the algorithm may proceed normally, proceed with non-fatal errors, or quit because of a fatal error. The 'quality assurance' (QA) of the retrieved products is assigned based on the behavior of the algorithm. Individual QA flags are assigned particular values when any errors (fatal or non-fatal) are encountered and stored within the L2 HDF/NETCDF aerosol product files. In MODIS C6.1 the QA flags are composed of data 'bits' that can be decoded to determine these errors, and in products of VIIRS, MEaSURES, and future MODIS C7, these errors are recorded as numbers. For example, one QA data flag warns the user to any 'water'

pixels within the box, even when the land retrieval is still performed. Details are provided in the Appendix 2.

Whether ocean or land aerosol retrieval was performed, the products are assigned a quality assurance 'confidence' flag (QAC) that represents the aggregate of all the individual QA flags. This QAC flag reflects our subjective appraisal of the quality of the retrieval based on a consistent set of rules within the algorithm. The QA value is also used to derive downstream products, either by its use as a filter for expected quantitative value of the retrieval, or to provide weighting for aggregating/averaging computations. The QAC value ranges from 3 to 0, where 3 means 'good' quality and 0 means 'bad' quality. Presumably, there is more quantitative value to a 'good' quality retrieval, rather than one that is 'fair', 'poor' or 'bad'. Appendix 2 describes the individual QA flags and how they are used to assign QAC.

The QAC flag is used to decide which land or ocean τ values go into a combined land and ocean product, known here as the *joint* L2 product. There are in fact two joint τ products. The unconstrained product, known as the 'Image_Optical_Depth_Land_And_Ocean', has no QAC threshold and is intended for evaluating plume locations, and creating attractive imagery with fewer holes. The other, known as the 'Optical_Depth_Land_And_Ocean', is constrained by QAC, in order to filter out lower confidence data with presumably less quantitative value. The constrained joint SDS requires QAC ≥ 1 over ocean (QAC = 1, 2, or 3), and QAC = 3 over land.

6. Algorithm Description: Ocean

6.1. Strategy

Let us assume that from the Main core, we have received an N × N worth of gas-corrected pixels, $\rho_\lambda^{\text{L1B}}$, along with the geolocation, cloud mask results (assuming the entire N×N box is ocean), and the ancillary wind speed information. The mechanics of the ocean algorithm are illustrated in Figure 6-1. The basic strategy of the dark target aerosol retrieval over the ocean (DT-O) is described in in Tanré et al. [*1997*], Levy et al. [*2003*], Remer et al. [*2005*] with the dynamic wind speed addition explained in Kleidman et al. [*2012*]. It follows the DT strategy presented in Section 2.2, in that one fine "*f*" and one coarse "*c*" aerosol model can be combined with FMW (η) to represent the ambient aerosol properties and TOA spectral reflectance (Eq. $\rho_\lambda^* = \eta\rho_\lambda^{*,\text{f}} + (1-\eta)\rho_\lambda^{*,\text{c}}$ Eq. 2-27; rewritten here),

$$\rho_\lambda^* = \eta\rho_\lambda^{*,\text{f}} + (1-\eta)\rho_\lambda^{*,\text{c}} \qquad\qquad \text{Eq. 6-1}$$

Spectral reflectance from the LUT is compared with MODIS-measured spectral reflectance to find the 'best' (least-squares) fit across multiple wavelengths. This best fit, or an 'average' of a set of the best fits is the solution to the inversion. Although the core inversion remains similar to the process described in Tanré, et al. [*1997*], the algorithm has evolved over time to include sediment masking, the special handling of heavy dust over glint, minor updates to masking of clouds, and the inclusions of multiple wind speed look-up tables. In this section, we describe the over-ocean LUTs, the cloud masking and pixel selection logic, the retrieval strategy details, and over-ocean product description.

DT-Ocean retrieval

NxN box worth of pixels
1) NxN geolocation
2) Gas corrected-reflectances
3) Ocean cloud mask results
4) Wind speed (from meteorology)

Meanwhile

LUTs for DT-O

Mask, Sort, Filter
1) Discard pixels marked "cloud"
2) Discard sediment pixels
3) Sort remainder by NIR band reflectance
4) Discard brightest 25% and darkest 25%
5) nPix = number of remaining pixels / NxN

Reduce aerosol LUT
1) Interpolate LUT for wind speed
2) Interpolate LUT for geolocation angles (θ_0, θ, ϕ)

Enough pixels left?

No

Yes

1) Calculate mean reflectance ρ_λ^{obs}
2) Perform glint / dust tests

Fill Values

Heavy dust over glint?

No

No

Is GA < 40°?

Yes

Yes

"Clear sky" reflectance
1) Mean reflectance in 7 bands (ρ_λ^{obs})

Reduced LUT
1) Fine: $\rho_\lambda^{LUT',f}$ (4 modes, 7 AODs)
2) Coarse: $\rho_\lambda^{LUT',c}$ (5 modes, 7 AODs)

Inversion
1) For each of 20 combinations ($4f \times 5c$): Find FMF (η) and interpolated AOD (τ), that minimizes the sum of differences ε between LUT-derived reflectance and observations ρ_λ^{obs}.
2) "Best" solution is combination of f, c, η, τ_λ with minimum ε
3) "Average" solution is $\overline{\tau}_\lambda$ for all combinations which meet criteria for ε.

Success?

No

Fill Values

Yes

Final Steps
1) Identify failure points (if any)
2) Determine QAC (function of ε, nPix, etc.)
3) Compute additional properties (AE, r_eff)
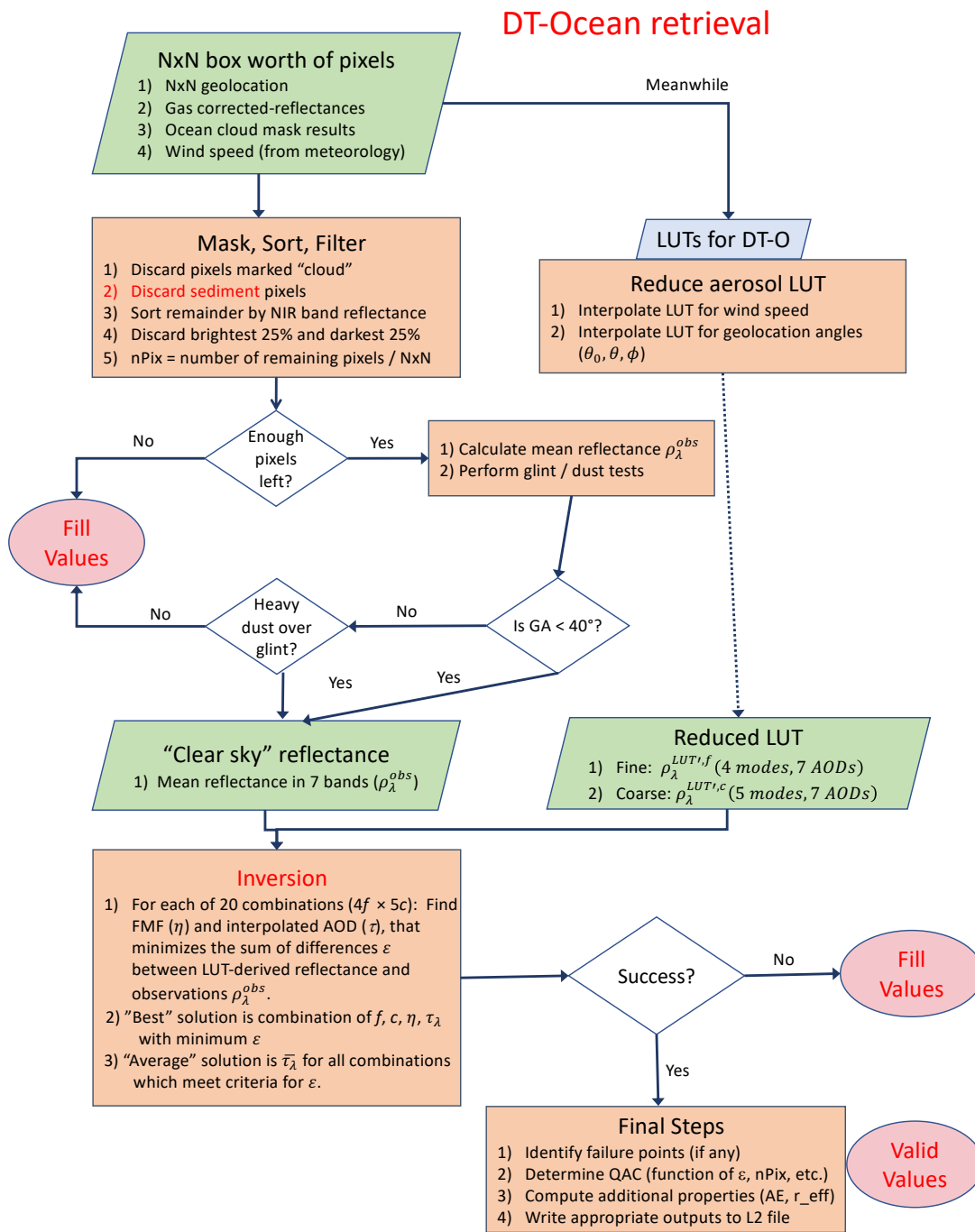4) Write appropriate outputs to L2 file

Valid Values

Figure 6-1. Flow chart of DT over ocean algorithm.

6.2.   LUTs for DT Ocean:

6.2.1. Aerosol Models

The aerosol optical models for DT-O are derived mainly from data gleaned from sun/sky photometers (e.g. AERONET; Holben et al., [*1998*]), and from analysis of errors in the products from previous versions of the algorithm. For DT in general, there are four fine modes and five coarse modes, with spectral refractive indices and lognormal size parameters computed via a Mie code. **Table 6-1** to **Table 6-4** describe spectral properties of the aerosol modes for the exact MODIS wavelengths (**Table 3-2**), for unit AOD =1.0 (at 0.55 μm). Other sensors will have similar spectral properties, although different exact values at their respective wavelengths. Figure 6-2 illustrates the properties of 4 fine and 5 coarse modes for the DT-O, plotted at MODIS and VIIRS wavelengths, computed for AOD = 1.0 at 0.55 μm.

TABLE 6-1: REFRACTIVE INDICES, NUMBER MEDIAN, STANDARD DEVIATION AND EFFECTIVE RADIUS FOR THE AEROSOL MODES USED IN THE MODIS LOOKUP TABLE FOR THE OCEAN ALGORITHM. MODELS 1-4 ARE FINE MODES AND MODELS 5-9 ARE COARSE MODES. ALL MODES LISTED HERE ARE ASSUMED SPHERICAL.

F	λ=blue, green, red, NIR	λ =NIR1	λ =SWIR1	λ =SWIR2	r_g	σ	r_{eff}	Comments
1	1.45-0.0035i	1.45-0.0035i	1.43-0.01i	1.40-0.005i	0.07	0.40	0.10	Water Soluble
2	1.45-0.0035i	1.45-0.0035i	1.43-0.01i	1.40-0.005i	0.06	0.60	0.15	Water Soluble
3	1.40-0.0020i	1.40-0.0020i	1.39-0.005i	1.36-0.003i	0.08	0.60	0.20	Water Soluble + humidity
4	1.40-0.0020i	1.40-0.0020i	1.39-0.005i	1.36-0.003i	0.10	0.60	0.25	Water Soluble + humidity

C	λ=blue, green, red, NIR	λ =NIR1	λ =SWIR1	λ =SWIR2	r_g	σ	r_{eff}	Comments
5	1.35-0.001i	1.35-0.001i	1.35-0.001i	1.35-0.001i	0.40	0.60	0.98	Wet sea salt type
6	1.35-0.001i	1.35-0.001i	1.35-0.001i	1.35-0.001i	0.60	0.60	1.48	Wet sea salt type
7	1.35-0.001i	1.35-0.001i	1.35-0.001i	1.35-0.001i	0.80	0.60	1.98	Wet sea salt type
8	1.53-0.003i (blue) 1.53-0.001i (green) 1.53-0.000i (red, NIR)	1.46-0.000i	1.46-0.001i	1.46-0.000i	0.60	0.60	1.48	Dust-like type
9	1.53-0.003i (blue) 1.53-0.001i (green) 1.53-0.000i (red, NIR)	1.46-0.000i	1.46-0.001i	1.46-0.000i	0.50	0.80	2.50	Dust-like type

TABLE 6-2: SPECTRAL AOD DEPENDENCE FOR THE NINE SPHERICAL AEROSOL MODES FOR MODIS WAVELENGTHS. RIGHT TWO COLUMNS ARE ÅNGSTROM EXPONENT

λ (μm) Mode	0.466	0.554	0.645	0.857	1.241	1.628	2.113	AE	0.86 0.55	2.11 0.86
1 F	1.539	1	0.66	0.285	0.086	0.047	0.016		2.877	3.183
2 F	1.305	1	0.764	0.426	0.17	0.081	0.03		1.957	2.927
3 F	1.247	1	0.796	0.481	0.213	0.105	0.042		1.677	2.696
4 F	1.187	1	0.832	0.547	0.269	0.14	0.06		1.385	2.449
5 C	0.966	1	1.022	1.026	0.918	0.764	0.586		-0.058	0.619
6 C	0.967	1	1.033	1.093	1.118	1.058	0.927		-0.204	0.182
7 C	0.977	1	1.026	1.087	1.166	1.179	1.124		-0.191	-0.037
8 C	0.977	1	1.026	1.087	1.185	1.192	1.127		-0.19	-0.04
9 C	0.982	1	1.019	1.059	1.118	1.137	1.126		-0.131	-0.069

TABLE 6-3: SPECTRAL SINGLE SCATTERING ALBEDOS FOR THE NINE SPHERICAL AEROSOL MODES FOR MODIS WAVELENGTHS

λ (μm) Mode	0.466	0.554	0.645	0.857	1.241	1.628	2.113
1 F	0.974	0.968	0.961	0.94	0.879	0.541	0.499
2 F	0.978	0.977	0.976	0.97	0.956	0.817	0.822
3 F	0.987	0.986	0.986	0.984	0.978	0.921	0.916
4 F	0.986	0.987	0.987	0.985	0.982	0.94	0.941
5 C	0.978	0.982	0.985	0.989	0.991	0.992	0.993
6 C	0.966	0.972	0.976	0.983	0.988	0.991	0.992
7 C	0.955	0.962	0.967	0.976	0.984	0.988	0.99
8 C	0.901	0.967	1	1	1	0.99	1
9 C	0.867	0.953	1	1	1	0.983	1

TABLE 6-4: SPECTRAL ASYMMETRY PARAMETERS FOR THE NINE SPHERICAL AEROSOL MODES FOR MODIS WAVELENGTHS

λ (μm) Mode	0.466	0.554	0.645	0.857	1.241	1.628	2.113
1 F	0.576	0.511	0.447	0.321	0.178	0.105	0.063
2 F	0.683	0.66	0.635	0.575	0.468	0.369	0.265
3 F	0.735	0.718	0.699	0.651	0.559	0.472	0.372
4 F	0.751	0.74	0.726	0.69	0.618	0.546	0.458
5 C	0.785	0.786	0.789	0.794	0.795	0.787	0.769
6 C	0.795	0.788	0.786	0.787	0.794	0.796	0.792
7 C	0.81	0.8	0.793	0.786	0.788	0.794	0.796
8 C	0.753	0.72	0.697	0.679	0.713	0.72	0.719
9 C	0.78	0.746	0.723	0.706	0.722	0.722	0.715

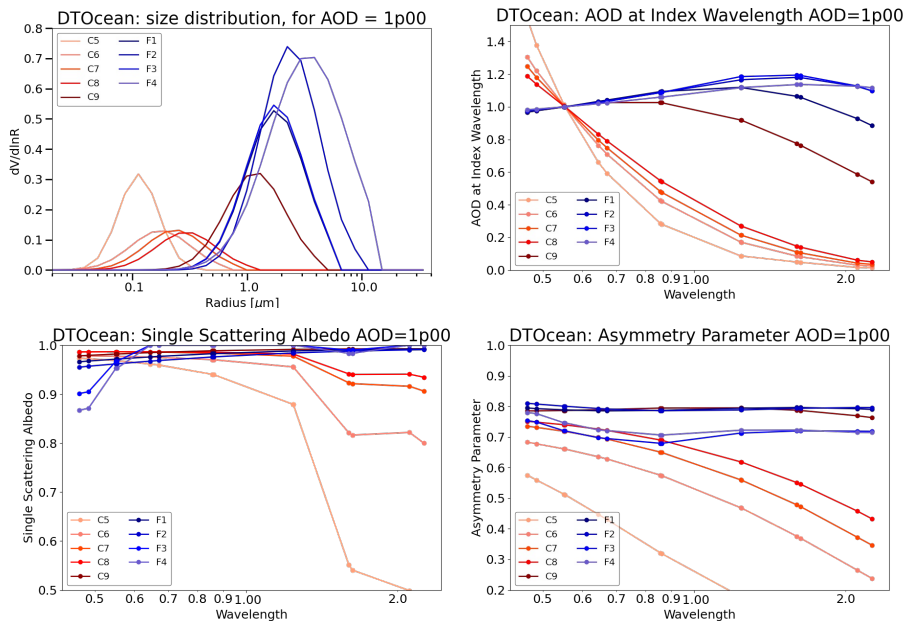## Properties of Aerosol Modes for DT-O

33

Figure 6-2: Properties of 4 Fine and 5 Coarse modes for the DT-O, plotted at MODIS and VIIRS wavelengths, computed for AOD = 1.0 at 0.55 µm.

The DT-O LUT employs the Ahmad and Fraser (1981) vector radiative transfer (AFRT) code to simulate TOA reflectance for a coupled ocean/atmosphere. AFRT includes toggles for whether to include polarization (turned on), trace gas coupling (turned off) and pseudospherical atmosphere (turned on). AFRT includes an internal Mie code (for calculating scattering properties of spherical particles) but can be set up to use external calculations of scattering properties (if non-spherical). For spherical modes 1F to 9C all Mie calculations are performed internally.

6.2.2. Reflectance-versus-Aerosol LUT

The spectral reflectance at the satellite level is the coupled combination of radiation from the surface and the atmosphere. The ocean surface calculation includes sun glint reflection off the surface waves [*Cox and Munk, 1954*], reflection by foam and whitecaps [*Koepke, 1984*] and Lambertian reflectance from underwater scattering (sediments, chlorophyll, etc). The LUT includes simulations for four wind speeds, 2 m/s, 6 m/s, 10 m/s, and 14 m/s, having foam fractions of 0.01%, 0.16%, 1% and 3%, respectively (e.g. Monahan and Muircheartaigh, [*1980*]). Zero water leaving radiance is assumed for all compared wavelengths, except for the green, where a fixed reflectance of 0.005 is used. The atmospheric contribution includes multiple scattering by gas and aerosol, as well as reflection of the atmosphere by the sea surface. Central wavelengths, Rayleigh optical depths and molecular depolarization factors (also known as King factors) are prescribed in the AFRT, based on the exact characteristics of the sensor's wavelength bands.

Thus, TOA spectral reflectance is computed for each of the nine spherical aerosol models (combined with Rayleigh and surface) described in the **Table 6-1**. Six values of total aerosol loading (AOD at 0.55 μm, denoted as t number of AOD) are considered for each mode, ranging from a pure molecular (Rayleigh) atmosphere ($\tau = 0.0$) to a highly turbid atmosphere ($\tau = 3.0$), with intermediate values of 0.2, 0.5, 1.0 and 2.0. For each model and aerosol optical depth at 0.55 μm, the associated aerosol optical depths are stored for all the sensor's seven wavelengths, including the blue, which is not used in the least squares fit to spectral reflectance. Also stored are aerosol optical depth values for the sensor's green channel, which may or may not be the same as the reference wavelength of 0.55 µm. Computations are performed for combinations of 11 solar zenith angles (6°, 12°, 24°, 36°, 48°, 54°, 60°, 66°, 72°, 78° and 84°), 16 satellite view zenith angles (0° to 72°, increments of 6°) and 16 relative sun/satellite azimuth angles (0° to 180°, increments of 12°) for a total of 2816 angular combinations. Again, note that scattering and LUT calculations are specific for a given sensor's wavelength band, however always normalized to AOD = 1.0 at 0.55 µm. Also note that for sensors that do not include a particular band (e.g., no NIR1 on ABI or AHI), placeholders are included so that the LUT will always be indexed for 7 wavelengths. Let us denote the spectral reflectance in the LUT as $\rho_\lambda^{\text{LUT}''}(v, j, t, \theta_0, \theta, \phi)$, where $v, j, t, \theta_0, \theta, \phi$ are indices for windspeed, aerosol model, aerosol loading (defined by AOD at 0.55 µm), and angles. During the retrieval, this LUT spectral reflectance is interpolated to represent the actual wind speed (provided by ancillary information) and angles.

6.3. Selection of Pixels: Cloud, Glint and Sediment Masking

6.3.1. Masking Overview:

The masking of clouds and sediments and the selection of pixels are described in Remer et al., [*2005*] and Levy et al., [*2013*]. Much attention has been paid in the algorithm to the difficult task of separating usable "clear" pixels from cloudy or cloud contaminated pixels [*Remer et al., 2012*]. Most

standard cloud masks, e.g. the Continuity MODIS-VIIRS cloud mask [*Frey et al., 2020*] includes using the brightness in the visible channels to identify clouds. This procedure can incorrectly identify heavy aerosol as 'cloudy', and will thereby miss retrieving significant aerosol events over ocean. On the other hand, relying on IR-tests alone permits low altitude, warm clouds to escape and be misidentified as 'clear', introducing cloud contamination in the aerosol products. Thus, our cloud mask over ocean combines spatial variability tests (e.g. Martins et al. [*2002*]) along with tests of brightness in visible and infrared channels. Appendix 3.1.1 describes the cloud mask over ocean. Underwater sediments have proved to be a problem in shallow water (near coastlines) as the sediments can easily have land-like surface properties. Thus, the sediment mask is used in addition to the cloud mask, using all available wavelength described in Li et al. [*2003*] (Appendix 3.1.2).

   The algorithm sorts the remaining pixels that have evaded all the cloud masks and the sediment mask according to their ρ_{NIR}^{L1B} value, discards the darkest and brightest 25%, and thereby leaves the middle 50% of the data. The filter is used to eliminate residual cloud contamination, cloud shadows, or other unusual extreme conditions in the box. Because the ocean cloud mask and the ocean surface are expected to be less problematic than their counterparts over land, the filter is less restrictive than the one used in the land retrieval. A minimum number of pixels remaining after masking and filtering is needed for the algorithm to continue. The algorithm also requires a minimum of 5% pixels at NIR channel over ocean with at least 10% pixels distributed over the other five channels. If the minimum number of pixels is not met, no retrieval is attempted, and fill values are given for the aerosol products in the retrieval box. If the minimum is met, the mean reflectance and standard deviation are calculated for the remaining 'good' pixels at the pertinent wavelengths. Let us denote the vector of observed mean spectral reflectance as ρ_{λ}^{obs}. By this point it is assumed to be suitable for inversion, meaning free of clouds, cloud edges, and sediments.

TABLE 6-5 RETRIEVAL BOX AGGREGATION SCHEME, NOMINAL BOX SIZE AT NADIR AND MINIMUM NUMBER OF PIXELS NEEDED IN THE BOX AFTER MASKING AND FILTERING TO PROCEED WITH A RETRIEVAL BY SENSOR.

Sensor	MODIS-Terra	MODIS-Aqua	VIIRS-SNPP	VIIRS-NOAA20	ABI-GOES16	ABI-GOES17	ABI-GOES18	AHI-H08/H09	eMAS-SEACR4s	eMAS-FIREX
N×N aggregation (of blue band)	20×20 or 6×6**	20×20 or 6×6**	8×8	8×8	10×10	10×10	10×10	10×10	10×10	10×10
DT Product resolution at nadir (km)	10×10 km or 3×3 km**	10×10 km or 3×3 km**	6×6 km	6×6 km	10×10 km	10×10 km	10×10 km	10×10 km	0.5×0.5 km	0.5×0.5 km
Minimum number of unmasked pixels to proceed with retrieval	10% over land & 5% over ocean after mask and filtering 5**	10% over land & 5% over ocean after mask and filtering 5**	10% over land & 5% over ocean after mask and filtering	10% over land & 5% over ocean after mask and filtering	10% over land & 5% over ocean after mask and filtering	10% over land & 5% over ocean after mask and filtering	10% over land & 5% over ocean after mask and filtering	10% over land & 5% over ocean after mask and filtering	10% over land & 5% over ocean after mask and filtering	10% over land & 5% over ocean after mask and filtering

   ** MODIS is produced at both 10 km and 3 km nominal resolution, with each requiring a different minimum number of pixels to proceed.

6.3.2. Ocean Glint and Internal Consistency:

   The ocean algorithm was designed to retrieve only over dark ocean, (i.e. away from glint). There is a special case when we retrieve over glint, and that is described below. The algorithm calculates the glint angle, which denotes the angle of reflection, compared with the specular reflection angle. The glint angle Θ_{glint} was defined via Equ 23B. Note that Fresnel reflection corresponds to $\Theta_{glint} = 0$. If

$\Theta_{glint} > 40°$, we can avoid glint contamination and proceed with the retrieval. The algorithm performs several consistencies checks of the spectral reflectances. Depending on the outcome of these consistency checks, the algorithm may either declare the reflectances to be beyond the range necessary for a successful inversion and exit the procedure or continue onto the inversion after assigning a quality assurance 'confidence' flag (QAC) to each wavelength (See Section 5.2).

6.4.   Retrieval Algorithm

6.4.1. Algorithm Overview

Following Tanré et al. [*1996*], we know that the measured multi-channel spectral radiance ρ_λ^{obs}, spanning visible through SWIR (green, red, NIR, SWIR2), contains almost three pieces of independent information about the aerosol loading and size properties. With assumptions that limit the choices of possible aerosol types to those in Table 6-1, the algorithm can derive three parameters: the total AOD defined at 0.55 µm, ($\tau_{\lambda=0.55}$), the 'reflectance weighting parameter' (the over-ocean definition of Fine Model Weighting - η), and the choice of which combination of 'fine' (*f*) and single 'coarse' (*c*) aerosol modes that lead to the solution. The combination of η and mode choices translate to the ''effective radius' (r_e), which is the ratio of the 3rd and 2nd moments of the aerosol size distribution.

We note that the retrieval of η is determined based on *reflectance* weighting, but that by knowing how the spectral dependence of reflectance is related to each model's AOD within the LUT (indexed at 0.55 µm), we also uniquely derive Fine Mode Weighting in terms of AOD, $\eta_{0.55}$. This means that in addition to total AOD at any wavelength, τ_λ, we can also estimate the fine and coarse models' contributions to total AOD at 0.55 µm ($\tau_{\lambda=0.55}^f$ and $\tau_{\lambda=0.55}^c$). Since we know the spectral extinction of each model, we can also report fine and coarse AOD any wavelength (τ_λ^f and τ_λ^c).

The trick is to determine "which" fine and coarse models represent the best solutions. The first step is to interpolate the LUT, removing the dependencies of the LUT reflectance on wind speed and angles, resulting in $\rho_\lambda^{LUT'}(j,t)$. Models *j* are assumed to be split into four fine modes *f*=1,4 and *c*=5,9. The difficulty is in determining which of the $(4 \times 5 = 20)$ twenty combinations of fine and coarse modes and their relative optical contributions η and τ that best mimics the observed spectral reflectance ρ_λ^{obs}. The retrieval proceeds via iteration. Each combination of f and c is tested (e.g. $\rho_\lambda^{LUT',f}(t)$ and $\rho_\lambda^{LUT',c}(t)$, with simultaneous interpolation between values of η (between 0.0 and 1.0) and aerosol loading values (indexed by *t*) within the LUT. The result for each combination

$$\rho_\lambda^{LUT\_com}(\tau_{0.55}^{com}) = \eta^{com}\rho_\lambda^{LUT'\_f}(\tau_{0.55}^{com}) + (1 - \eta^{com})\rho_\lambda^{LUT'\_c}(\tau_{0.55}^{com}) \qquad \text{Eq. 6-2}$$

where $\rho_\lambda^{LUT\_com}(\tau_{0.55}^{com})$ is a weighted average reflectance of an atmosphere with a pure fine mode 'f' and optical thickness $\tau_{0.55}^{com}$ and the reflectance of an atmosphere with a pure coarse mode 'c' also with the same $\tau_{0.55}^{com}$. Thus, the inversion finds the pair of $\tau_{0.55}^{com}$ and η^{com} that minimizes the 'fitting error' (ε) defined as

$$\varepsilon = \sqrt{\left(\sum_{\lambda=1}^{N_{wav}} N_\lambda \left(\frac{\rho_\lambda^{obs} - \rho_\lambda^{LUT\_com}}{\rho_\lambda^{obs} - \rho_\lambda^R + 0.01}\right)^2\right)\Big/\left(\sum_{\lambda=1}^{N_{wav}} N_\lambda\right)} \qquad \text{Eq. 6-3}$$

where N_{wav} is the number of pertinent wavelengths for the retrieval. Note that the blue channel is never used in the retrieval to avoid uncertainty in ocean color, Therefore, the maximum value of N_{wav} is six, but specific sensors may use fewer pertinent wavelengths. N_λ is the sum of good pixels at

wavelength λ, ρ_λ^{obs} is the measured MODIS reflectance at wavelength λ, ρ_λ^{R} is the reflectance contributed by Rayleigh scattering, and $\rho_\lambda^{LUT\_com}$ is calculated from the combination of modes in the LUT and defined by $\boldsymbol{\rho\lambda LUT\_com}(\tau_{0.55}^{com}) = \boldsymbol{\eta^{com}}\rho_\lambda^{LUT'\_f}(\tau_{0.55}^{com}) + (\mathbf{1} - \boldsymbol{\eta^{com}})\rho_\lambda^{LUT'\_c}(\tau_{0.55}^{com})$ Eq. **6-2**. The 0.01 is to prevent a division by zero for the longer wavelengths under clean conditions [*Tanré et al. 1997*]. The inversion requires $\rho_{NIR}^{LUT\_com}$ to exactly fit the observations at that wavelength and then finds the best fits to the other five or fewer wavelengths via

Eq. $\varepsilon = \sqrt{\left(\sum_{\lambda=1}^{N_{wav}} N_\lambda \left(\frac{\rho_\lambda^{obs} - \rho_\lambda^{LUT\_com}}{\rho_\lambda^{obs} - \rho_\lambda^{R} + 0.01}\right)^2\right) \bigg/ \left(\sum_{\lambda=1}^{N_{wav}} N_\lambda\right)}$ Eq. **6-3**. The NIR channel was chosen to be the

primary wavelength because it is expected to be less affected by variability in water leaving radiances than the shorter wavelengths, yet still exhibit a strong aerosol signal, even for aerosols dominated by the fine mode By emphasizing accuracy in this channel variability in chlorophyll will have negligible effect on the optical thickness retrieval and minimal effect on $\eta_{0.55}$. For each combination (f, c, $\tau_{0.55}^{com}$ and η^{com}) one can use the LUT to infer a variety of parameters, including spectral optical depth, fine-mode AOD, coarse-mode AOD, effective radius, spectral flux, mass concentration, etc.

This iterative fitting process occurs for each of the twenty fine/coarse mode combinations, which are then sorted according to values of ε. The combination of modes with accompanying $\tau_{0.55}^{combo}$ and $\eta_{0.55}$, with the minimum ε, is known as the 'best' solution. Let us denote this 'best' solution combination as f^{best}, c^{best}, τ_λ^{best} and $\eta_{0.55}^{best}$, and we record the inferred 'best' parameters associated this combination (spectral AOD, fine/coarse AOD, effective radius, etc.). A study exploring the sensitivity of the basic retrieval to perturbations in calibration, surface assumptions, glint and to situations not well-represented in the LUT. The results of this study are given in Tanré et al. [*1997*].

This 'best' solution might be a poor solution (large fitting error), or it may be one of multiple "good" solutions that have similar fitting error less than a threshold (currently set as ε < 3.7%). Therefore, the DT retrieval also calculates a more robust 'average' solution τ_λ^{avg} and $\eta_{0.55}^{avg}$. How the 'avg' is calculated, depends on the number of good solutions. If the 'best' solution is the only good one, then all 'avg' are set to the same values as the 'best'. If there are at least two good solutions, then 'avg' is the simple average of those. However, if there are no good solutions (all combinations have ε ≥ 3.7%), then the top three combinations are used to calculate a weight-based 'avg', where the weights are based on a modified epsilon, e.g $\varepsilon' = (1/\varepsilon)^2$. Regardless of the method used for calculating the average solutions, we record the derived spectral AOD, fine/coarse AOD, effective radius, etcetera.

6.4.2. Final Checking.

Before the final results are output, additional consistency checks are employed. In general, if $-0.01 < \tau_{0.55} \leq 5$, then the results are output. There are exceptions and further checking for heavy dust retrievals made over the glint. The final QAC flag may be adjusted during this final checking phase.

6.4.3. Special Case: Heavy Dust Over Glint.

If $\Theta_{glint} \leq 40°$, a case where we normally do not retrieve, we check for heavy dust in the glint. Since heavy dust has a distinctive spectral signature because of light absorption at blue wavelengths, we use a similar technique during the masking operations by designating all values of $\frac{\rho_{green}}{\rho_{red}} < 0.95$ to be heavy dust. If heavy dust is identified in the glint, the algorithm continues with the retrieval, although it sets QAC=0. This permits the retrieval but prohibits the values from being included in the Level 3

statistics [*Remer et al., 2005*]. If heavy dust is not identified in the glint, then the algorithm writes fill values to the aerosol product arrays and exits the procedure.

6.5.   Retrieved Ocean Products

All products of DT-O are reported in output Level 2 files as Scientific Data Sets (SDSs), and the MODIS C6.1 SDSs are listed in **Error! Not a valid bookmark self-reference.**. These include the *primary retrieved* products, *derived* products, and *diagnostic* products. Where possible, the Table connects symbols from the text above, to the SDS names and their dimensions. For MODIS C6.1, many SDSs have both 'best' and 'avg' values, sometimes noted as separate SDSs (e.g., $\tau_\lambda^{best}=$ 'Effective_Optical_Depth_Best_Ocean' and $\tau_\lambda^{avg}=$ 'Effective_Optical_Depth_Average_Ocean'), and sometimes noted as one SDS having two dimensions ($\eta_{0.55}^{best}, \eta_{0.55}^{avg}=$ 'Optical_Depth_Ratio_Small_Ocean_0.55micron'). A few SDSs only refer to 'best' solutions, including the choice of which fine and coarse modes ('Solution_Index_Small' and 'Solution_Index_Large'), and the 'Optical_Depth_by_Models' $\tau_{0.55}^{best,j}$ which refers to the values of fine and coarse mode AODs, $\tau_{0.55}^{best,f}$ and $\tau_{0.55}^{best,c}$, but with two values of j filled with values, j1 = Solution_Index_Small, and j2 = Solution_Index_Large.

In addition to the retrieved and derived parameters, DT-O also provides a number of diagnostic products. The most important is the 'Quality_Assurance_Ocean' (QA), which is a qualitative estimate of the overall retrieval's quality and confidence. Details about QA are given in the Appendix 2. Other parameters related to the direct retrieval include the vector of TOA reflectance ρ_λ^{obs} and its standard deviation, which is denoted as 'Mean_Reflectance_Ocean' and 'STD_Reflectance_Ocean'. Finally, there are a number of SDSs related to the suitability of the retrieval box in the first place, including the number of L1B pixels used ('Number_Pixels_Used_Ocean') the estimated cloud fraction ('Aerosol_Cloud_Fraction_Ocean'). More details about these are given in Section 10.

Table 6-7 lists the side-by-side comparison of DT ocean products for MODIS C6.1 versus products for VIIRS/ABI/AHI. Note that due to long-term confusion, nearly all SDSs related to the 'best' are removed for the continuity products. Only the SDS named Optical_Depth_By_Models remains to describe the result of the 'best' solution.

Some of the ocean products are combined with products from land (discussed in the next section) as the *Joint* products. For τ, two joint products are reported, the 'Optical_Depth_Land_And_Ocean' and the 'Image_Optical_Depth_Land_And_Ocean'. The first product is constrained by QAC whereas the "Image" product includes all QAC values in order to provide the most complete visualization of the AOD.

TABLE 6-6: CONTENTS OF MODIS C61 AEROSOL LEVEL 2 FILE (MOD04/MYD04): OCEAN PRODUCTS

Symbol	Name of Product (SDS)	Dimensions: 3rd Dimension	Type of product
τ_λ^{avg}	Effective_Optical_Depth_Average_Ocean	X,Y,7: 0.47,0.55,0.65,0.86,1.2,1.6,2.11μm	Retrieved Primary
τ_λ^{best}	Effective_Optical_Depth_Best_Ocean	X,Y,7: 0.47,0.55,0.65,0.86,1.2,1.6,2.11μm	Retrieved Primary
$\eta_{0.55}^{best}, \eta_{0.55}^{avg}$	Optical_Depth_Ratio_Small_Ocean_0.55micron	X,Y,2: best, average	Retrieved Primary
F^{best}	Solution_Index_Ocean_Small	X,Y,2: best, best	Retrieved Primary
c^{best}	Solution_Index_Ocean_Large	X,Y,2: best, best	Retrieved Primary
$\varepsilon^{best}, \varepsilon^{avg}$	Least_Squares_Error_Ocean	X,Y,2: best, average	Retrieved Diagnostic
$\tau_{0.55}^{avg}$	Effective_Optical_Depth_0p55um_Ocean	X,Y: 0.55 μm	Duplicate for Level 3
r_e^{best}, r_e^{avg}	Effective_Radius_Ocean	X,Y,2: best, average	Derived
$\tau_\lambda^{best,f}$	Optical_Depth_Small_Best_Ocean	X,Y,7: 0.47,0.55,0.65,0.86,1.2,1.6,2.11μm	Derived
$\tau_\lambda^{avg,f}$	Optical_Depth_Small_Average_Ocean	X,Y,7: 0.47,0.55,0.65,0.86,1.2,1.6,2.11μm	Derived
$\tau_\lambda^{best,c}$	Optical_Depth_Large_Best_Ocean	X,Y,7: 0.47,0.55,0.65,0.86,1.2,1.6,2.11μm	Derived
$\tau_\lambda^{avg,c}$	Optical_Depth_Large_Average_Ocean	X,Y,7: 0.47,0.55,0.65,0.86,1.2,1.6,2.11μm	Derived
	Mass_Concentration_Ocean	X,Y,2: best, average	Derived
	PSML0003_Ocean*	X,Y,2: best, average	Derived
	Asymmetry_Factor_Best_Ocean	X,Y,7: 0.47,0.55,0.65,0.86,1.2,1.6,2.11μm	Derived

	Asymmetry_Factor_Average_Ocean	X,Y,7: 0.47,0.55,0.65,0.86,1.2,1.6,2.11μm	Derived
	Backscattering_Ratio_Best_Ocean	X,Y,7: 0.47,0.55,0.65,0.86,1.2,1.6,2.11μm	Derived
	Backscattering_Ratio_Average_Ocean	X,Y,7: 0.47,0.55,0.65,0.86,1.2,1.6,2.11μm	Derived
	Ångstrom_Exponent_1_Ocean (0.55/0.86 micron)	X,Y,2: best, average	Derived
	Ångstrom_Exponent_2_Ocean (0.86/2.1 micron)	X,Y,2: best, average	Derived
$\tau_{0.55}^{best,j}$	Optical_Depth_by_models_ocean	X,Y,9: 9 models (best only)	Derived
	Aerosol_Cloud_Fraction_Ocean	X,Y:	Diagnostic
	Number_Pixels_Used_Ocean	X,Y,10: 0.47,0.55,0.65,0.86,1.2,1.6,2.11,0.41,0.44,0.76 μm	Diagnostic
ρ_{λ}^{obs}	Mean_Reflectance_Ocean	X,Y,10: 0.47,0.55,0.65,0.86,1.2,1.6,2.11,0.41,0.44,0.76 μm	Diagnostic
	STD_Reflectance_Ocean	X,Y,10: 0.47,0.55,0.65,0.86,1.2,1.6,2.11,0.41,0.44,0.76 μm	Diagnostic
	Wind_Speed_Ncep_Ocean	X,Y:	Diagnostic
	Quality_Assurance_Ocean	X,Y,5 bytes	Diagnostic
	Optical_Depth_Land_And_Ocean	X,Y: 0.55 μm	Joint (QA≥1)
	Image_Optical_Depth_Land_And_Ocean	X,Y: 0.55 μm	Joint (QA≥0)

TABLE 6-7: SIDE BY SIDE COMPARISON OF THE DATASETS IN EACH DARK TARGET PRODUCT (MODIS AQUA AND TERRA) AND VIIRS/ABI/AHI FOR OCEAN

MODIS	VIIRS/ABI/AHI
Optical_Depth_Land_And_Ocean	Optical_Depth_Land_And_Ocean
Image_Optical_Depth_Land_And_Ocean	Image_Optical_Depth_Land_And_Ocean
Effective_Optical_Depth_Best_Ocean	
Effective_Optical_Depth_Average_Ocean	Effective_Optical_Depth_Average_Ocean
Optical_Depth_Small_Best_Ocean	
Optical_Depth_Small_Average_Ocean	Optical_Depth_Small_Average_Ocean
Optical_Depth_Large_Best_Ocean	
Optical_Depth_Large_Average_Ocean	Optical_Depth_Large_Average_Ocean
Mass_Concentration_Ocean	Mass_Concentration_Ocean
Aerosol_Cloud_Fraction_Ocean	Aerosol_Cloud_Fraction_Ocean
Effective_Radius_Ocean	Effective_Radius_Ocean
PSML003_Ocean	PSML003_Ocean
Asymmetry_Factor_Best_Ocean	
Asymmetry_Factor_Average_Ocean	Asymmetry_Factor_Average_Ocean
Backscattering_Ratio_Best_Ocean	
Backscattering_Ratio_Average_Ocean	Backscattering_Ratio_Average_Ocean
Angstrom_Exponent_1_Ocean	Angstrom_Exponent_1_Ocean
Angstrom_Exponent_2_Ocean	Angstrom_Exponent_2_Ocean
Least_Squares_Error_Ocean	Least_Squares_Error_Ocean
Optical_Depth_Ratio_Small_Ocean_0.55micron	Optical_Depth_Ratio_Small_Ocean_0p55micron
Optical_Depth_by_models_ocean	Optical_Depth_By_Models_Ocean
Number_Pixels_Used_Ocean	Number_Pixels_Used_Ocean
Mean_Reflectance_Ocean	Mean_Reflectance_Ocean
STD_Reflectance_Ocean	STD_Reflectance_Ocean
Quality_Assurance_Ocean	
Glint_Angle	
Wind_Speed_Ncep_Ocean	Wind_Speed_GMAO_Ocean
Effective_Optical_Depth_0p55um_Ocean	
	Error_Flag_Land_And_Ocean
Solution_Index_Ocean_Small	
Solution_Index_Ocean_Large	

39

7. Algorithm Description: Land

7.1.   Theory and Flow Chart

Like the ocean algorithm (DT-O), the DT-L algorithm uses a Lookup table (LUT) approach, but only uses three wavelengths (blue, red & SWIR2) to retrieve three (nearly) independent pieces of information: total AOD (τ), Fine Model Weighting FMW (η), and the surface reflectance (ρ^s). Both AOD and FMW are defined in a green wavelength $\lambda = 0.55\ \mu m$ regardless of sensor. The main difference is that while DT-O explicitly includes the reflection of the ocean surface in its LUT, the DT-L algorithm assumes a relationship for surface reflectance in the blue, red, and SWIR2 known as the Surface Reflectance Parameterization (SRP). In addition, the aerosol model optical properties are prescribed based on season and location.

DT-L LUTs are pre-computed via RT, with the aerosol scattering properties a function of aerosol optical models (size distribution, shape properties and complex refractive index) used as inputs for the RT. Unlike the DT-O ocean which matches single aerosol "modes", the DT-L aerosol model types are each comprised of multiple lognormal modes. For the standard DT-L retrieval, three models are dominated by fine-sized aerosol particles (i.e. *fine-dominated*), whereas one model is *coarse-dominated*. All four models are based on climatology of AERONET sky-inversions, and prescription of fine-dominated aerosol type is contained as $1° \times 1°$ global map. The fine-dominated models are assumed to represent aerosol types with varying single scattering albedo (SSA) and 'dynamic' dependence on loading. They are known as *weakly-absorbing*, *moderately-absorbing*, and *highly-absorbing* respectively, and moderate loadings (AOD = 0.5 at 0.55 μm), have SSA (at 0.55 μm) of approximately $\omega_0 = 0.95$, 0.92, and 0.87 respectively. Details of the aerosol model derivation and calculations of LUTs are presented in Section 7.2.

To perform the inversion in the three channels simultaneously (blue, red & SWIR2) DT-L assumes that the SWIR2 (e.g. MODIS 2.1 μm) channel contains information about coarse mode aerosol as well as the surface reflectance. In turn, the surface reflectance in the visible is a function of the surface reflectance at SWIR2, as well as a function of the scattering angle and the "greenness" of the surface based on a SWIR – based Normalized Difference Vegetation Index (NDVI)-like parameter. Nominally, the NDVI$_{SWIR}$ is computed based on NIR1 and SWIR2, but NIR could be substituted for NIR1 if NIR1 is unavailable for a given sensor (as for ABI or AHI). The estimation of surface reflectance in DT-L is described via the SRP and is used as a constraint during the retrieval.

For MODIS C61 specifically, the DT-L algorithm also accounts for urban or built-up surfaces that modify the natural state of dark vegetation. The original SRP is modified to account for the Urban Percentage (UP) of the N × N retrieval box, for which the UP is contained in a map with $0.1° \times 0.1°$ resolution. Details of the derivation and formulas for SRP are presented in Section 7.3.

Even in a fine-dominated aerosol regime, τ is non-zero in a SWIR2 band. Under the moderately absorbing ($\omega_0 \sim 0.92$) model, $\tau_{0.55}$ of 1.0 corresponds to $\tau_{2.1}$ of 0.114, which corresponds to reflectance difference about 0.012. Via the RedvsSWIR2 reflectance relationship, the reflectance error in Red and Blue are on the orders of 0.006 of 0.003, leading to ~0.05 error in retrieved τ and large errors in spectral dependence (e.g. α) and Fine-model fraction η. If the SWIR2 channel is assumed to contain *both* surface and aerosol information, and we use the SRP, then from the three channels (Blue, Red, and SWIR2), we can derive AOD, FMF and surface reflectance.

Let us simplify Eq. $\rho_\lambda^*(\tau_\lambda^a, \theta_0, \theta, \phi) = \rho_\lambda^a(\tau_\lambda^a, \theta_0, \theta, \phi) + \dfrac{T_\lambda^\downarrow(\tau_\lambda^a, \theta_0) T_\lambda^\uparrow(\tau_\lambda^a, \theta) \rho_\lambda^s}{1 - s_\lambda(\tau_\lambda^a) \rho_\lambda^s}$,   Eq. 2-26.

$$\rho_\lambda^* = \rho_\lambda^a + \frac{T_\lambda^\downarrow T_\lambda^\uparrow \rho_\lambda^s}{1 - s_\lambda \rho_\lambda^s}, \qquad\qquad \text{Eq. 7-1}$$

where the first term ρ_λ^a represents the atmospheric path reflectance (for the sum of aerosol and Rayleigh), and the second term represents the interaction of the atmosphere and the surface. $T_\lambda^\downarrow(\theta_0)$ and $T_\lambda^\uparrow(\theta)$, are the atmospheric transmissions (function of zenith angles) from TOA "down" to surface and from surface "up" to observation, s_λ is the 'atmospheric backscattering ratio' (diffuse reflectance of the atmosphere for isotropic light leaving the surface), and ρ_λ^s is the 'surface reflectance' [*Kaufman et al., 1997a*], which for now we assume to be Lambertian. Since our light source is the sun (outside of the TOA), we recognize that the downward transmission (direct + diffuse) is the also the downward flux received at the surface, which might be referred to as F_{dn}. Also, note that when our observation is also the TOA (e.g., a satellite), the surface is Lambertian, and the satellite and sensor zenith angles are equal ($\theta_0 = \theta$), then $T_\lambda^\downarrow = T_\lambda^\uparrow$ (known as reciprocity). Reciprocity does not hold when our sensor is on an aircraft below the TOA.

Using Eq. $\rho \; \lambda \quad * \quad = \rho_\lambda^a + \frac{T_\lambda^\downarrow T_\lambda^\uparrow \rho_\lambda^s}{1 - s_\lambda \rho_\lambda^s},$ Eq. **7-1**, the TOA reflectance is theoretically the sum of *fine* and *coarse* contributions weighted by η.

$$\rho_\lambda^* = \eta \rho_\lambda^{*,\mathbf{f}} + (1 - \eta)\rho_\lambda^{*,\mathbf{c}} \qquad\qquad \text{Eq. 7-2}$$

where $\rho_\lambda^{*,f}$ and $\rho_\lambda^{*,c}$ are each composite of the *same* surface reflectance ρ_λ^s, but the aerosol model-dependent atmospheric path reflectances and up/down transmissions. That is

$$\rho_\lambda^{*,\mathbf{f}} = \rho_\lambda^{a,f} + \frac{T_\lambda^{\downarrow,f} T_\lambda^{\uparrow,f} \rho_\lambda^s}{1 - s_\lambda^f \rho_\lambda^s} \text{ and } \rho_\lambda^{*,\mathbf{c}} = \rho_\lambda^{a,c} + \frac{T_\lambda^{\downarrow,c} T_\lambda^{\uparrow,c} \rho_\lambda^s}{1 - s_\lambda^c \rho_\lambda^s} \qquad \text{Eq. 7-3}$$

whereas the other terms on the right are a function of the aerosol and are contained within the lookup tables, the surface reflectance is unknown. However, its spectral dependence is constrained by the SRP.

Due to the limited set of aerosol optical properties in the lookup table, the equations may not have exact solutions, and solutions may not be unique. Therefore, we find the aerosol solution most closely resembling the set of satellite-measured reflectances. In order to reduce the possibility of non-unique retrievals we only allow discrete values of η. During the retrieval, the algorithm tests whether certain criteria are met for consistency and valid retrieval steps. Results of these tests are encoded into a product called the 'Quality_Assurance_Land'. Upon completion, the retrieval is assigned a final QAC value that ranges from 0 (bad quality) to 3 (good quality). Details of the QA and QAC are given in the Appendix 2.

Figure 7-1 is a flowchart that describes the basics of the DT-L algorithm. Prior to DT-L, the N × N retrieval boxes have been created and corrected for gas absorption, the initial cloud mask has been determined, and the box has been assigned to "Land" (see Section 5.1). This information is captured within the top green box. At the same time, DT-L reads in the aerosol reflectance lookup tables (LUTs), and maps that prescribe the aerosol type and urban percentage (UP). In the following subsections, we describe procedures and elements needed for generating the LUT, following by explaining the filtering/mask requirements needed before inversion taken place. After that, we explain the mechanics of the inversion algorithm in more detail.
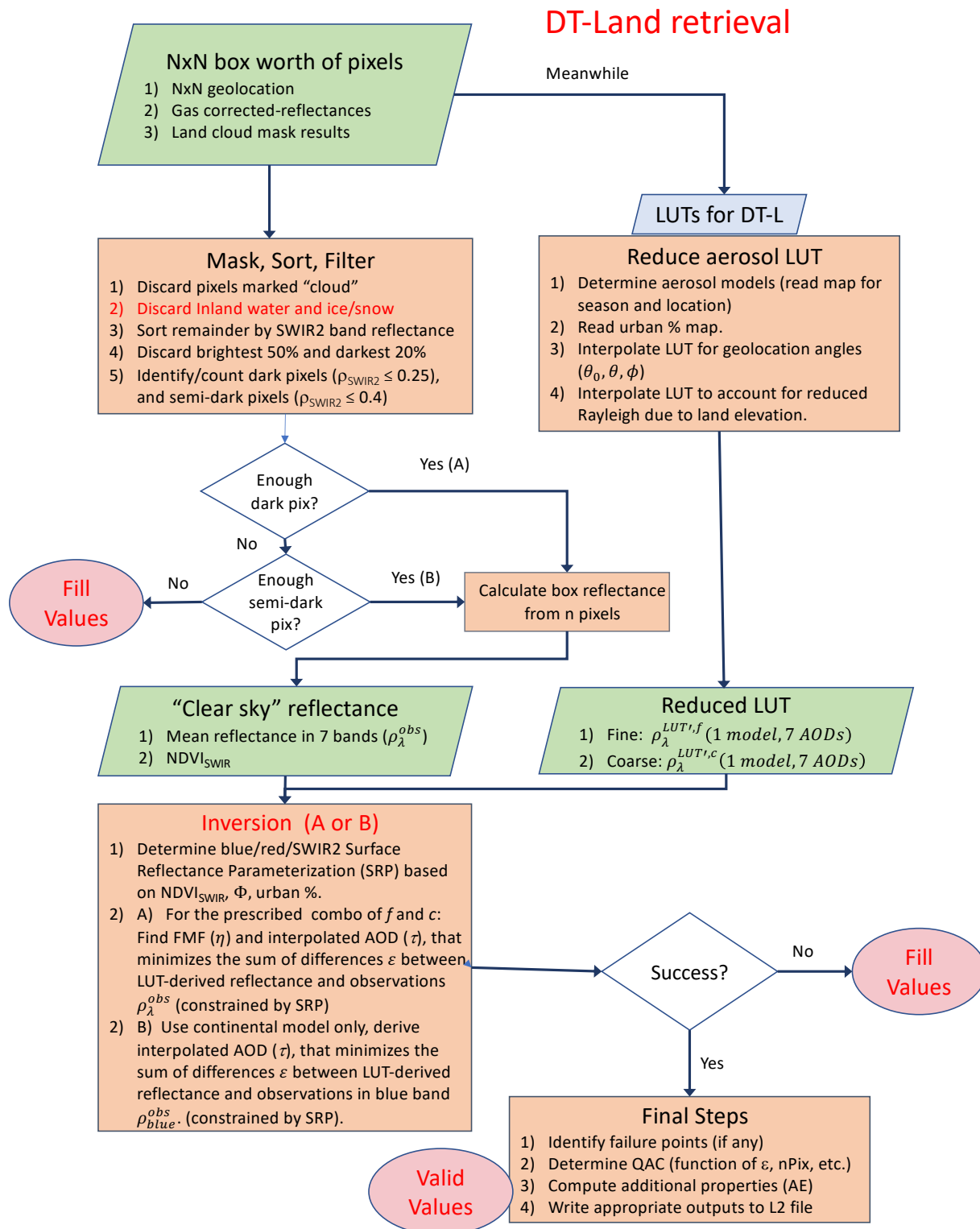
DT-Land retrieval

NxN box worth of pixels
1) NxN geolocation
2) Gas corrected-reflectances
3) Land cloud mask results

Meanwhile

LUTs for DT-L

Mask, Sort, Filter
1) Discard pixels marked "cloud"
2) Discard Inland water and ice/snow
3) Sort remainder by SWIR2 band reflectance
4) Discard brightest 50% and darkest 20%
5) Identify/count dark pixels ($\rho_{SWIR2} \leq 0.25$), and semi-dark pixels ($\rho_{SWIR2} \leq 0.4$)

Reduce aerosol LUT
1) Determine aerosol models (read map for season and location)
2) Read urban % map.
3) Interpolate LUT for geolocation angles (θ_0, θ, ϕ)
4) Interpolate LUT to account for reduced Rayleigh due to land elevation.

Enough dark pix? — Yes (A)

No

Enough semi-dark pix? — Yes (B)

No

Fill Values

Calculate box reflectance from n pixels

"Clear sky" reflectance
1) Mean reflectance in 7 bands (ρ_λ^{obs})
2) NDVI$_{SWIR}$

Reduced LUT
1) Fine: $\rho_\lambda^{LUT',f}$ (1 model, 7 AODs)
2) Coarse: $\rho_\lambda^{LUT',c}$ (1 model, 7 AODs)

Inversion (A or B)
1) Determine blue/red/SWIR2 Surface Reflectance Parameterization (SRP) based on NDVI$_{SWIR}$, Φ, urban %.
2) A) For the prescribed combo of f and c: Find FMF (η) and interpolated AOD (τ), that minimizes the sum of differences ε between LUT-derived reflectance and observations ρ_λ^{obs} (constrained by SRP)
2) B) Use continental model only, derive interpolated AOD (τ), that minimizes the sum of differences ε between LUT-derived reflectance and observations in blue band ρ_{blue}^{obs}. (constrained by SRP).

Success? — No — **Fill Values**

Yes

Final Steps
1) Identify failure points (if any)
2) Determine QAC (function of ε, nPix, etc.)
3) Compute additional properties (AE)
4) Write appropriate outputs to L2 file

Valid Values

Figure 7-1: Flowchart for the DT-Land retrieval.

7.2. Aerosol Models and Lookup Tables

7.2.1. Aerosol Model Derivation

The current aerosol models used in DT-L are built upon cluster analysis of a large data set of AERONET Level 2 (quality assured) sunphotometer (http://aeronet.gsfc.nasa.gov) sun observations and sky retrievals. AERONET provides direct 'sun' measurements of spectral AOD in four or more wavelengths (at least 0.44, 0.67, 0.87 and 1.02 μm) and indirect 'sky' measurements of almucantur radiance that are inverted into aerosol optical properties and size distributions. Sun measurements are made approximately every 15 minutes, whereas almucantar sky measurements are performed approximately every hour. An early analysis of AERONET data was performed by Omar et al., [*2005*], finding that six aerosol models (composed of desert dust, biomass burning, background/rural, polluted continental, marine, and dirty pollution, respectively) generally represented the entire AERONET dataset. The models varied mainly by their aerosol scattering and absorption qualities expressed as single scattering albedo ω_0 and size distribution (asymmetry parameter, *g*). Out of these six models, two models were representative of very clean conditions (marine and background/rural), such that coupled with uncertainties of surface properties, would not be resolvable by passive satellite.

To derive aerosol models representing higher-loading aerosol types that could be separatable via passive satellite, we (Levy et al. [*2007a*]) performed a "supervised" cluster analysis of the Version 1 AERONET sky retrievals, including only retrievals with the minimum quality parameters suggested by the AERONET team, including: τ at 0.44 μm greater than 0.4, solar zenith angle greater than 45°, 21 symmetric left/right azimuth angles, and radiance retrieval error less than 4%. We found that 4 clusters were generally representative and could be separated into those dominated by spherical particles and those dominated by non-spherical (assumed spheroids) particles. Since AERONET-derived volume concentrations tended to be dominated by fine-sized particles (radius = $r \ll 1.0 \, \mu m$) for spherical cases, and coarse-sized particles ($r > 1.0 \, \mu m$) for the spheroids, we assumed that the fine-spheres were non-dust and the coarse-spheroids were dust.

Each of these categories were separated by bins of AOD (e.g., $0.3 - 0.5, \ 0.5 - 0.7, \ 0.7 - 1.0, \ 1.0 - 2.0, \ < 3.0, \ > 5.0$). These subgroups were then clustered by two optical parameters, single scattering albedo ω_0 at 0.67 μm and asymmetry parameter, *g* at 0.44 μm. The result was that the dust/non-spherical retrievals, regardless of AOD bin, did not clearly separate into clusters. However, the non-dust (spherical) retrievals tended to consistently fall into three clusters, regardless of AOD bin. Assuming that one could connect the clusters across the AOD bins, the result was three "models" for which the size distribution and optical properties varied with AOD. In other words, the semi-objective clustering led to "dynamic" models resembling those already within the literature (e.g., Remer et al., [*1998*]). Note that the cluster analysis performed by Levy et al. [*2007a*] was repeated by Levy et al., [*2013*] to include Version 2 of the AERONET database, and that the results were similar enough to retain the C5 aerosol types for C6 and the current DT retrieval. We have not updated with Version 3 AERONET [*Giles et al, 2019*] which includes more sites, longer time series, and hybrid (principal plane) retrievals.

Under the DT-L framework, these models are currently known as

- Model 2 = "generic" or "moderately-absorbing, fine-dominated"
- Model 3 = "smoke" or "strongly-absorbing, fine-dominated"
- Model 4 = "urban/industrial" or "weakly-absorbing, fine-dominated".
- Model 5 = "dust" or "coarse-dominated"

All 4 models are represented by two lognormal modes (fine/accumulation + coarse: each having characteristic radius and standard deviation) with relative volume concentrations, and complex

refractive index. The values for each are reported in **Table 7-1**, where each parameter is dynamic (function of AOD loading). Again the three fine-modes are considered to be spherical particles, whereas the dust is based on spheroid particles, specifically having the same 11-node axis ratio distribution (1.0 = spherical) as used in the Version 1 AERONET retrieval algorithm and defined by Dubovik et al. [*2000*]. The axis ratio is listed in **Table 7-2**.

TABLE 7-1: DISPLAYS THE OPTICAL PROPERTIES AND SIZE DISTRIBUTIONS FOR THE THREE SPHERICAL (MODERATELY ABSORBING, ABSORBING AND NON-ABSORBING) FINE-DOMINATED MODELS AND THE ONE SPHEROID COARSE AEROSOL (DUST) MODEL (MODELS 2-5), AND THE CONTINENTAL MODEL (MODEL 1). THE "CONTINENTAL MODEL" (E.G. VERMOTE ET AL. [*1997*]; LENOBLE AND BROGNIEZ, [*1984*]) IS ONLY USED FOR "PROCEDURE B: ALTERNATIVE RETRIEVAL FOR BRIGHTER SURFACES" DESCRIBED IN SECTION 7.5.2.

Indx	Model	Mode	r_v (μm)	σ	V_0 (μm³/μm²)	Refractive Index: k	ω_0 / g (Blue/Green/Red/SWIR2) for $\tau_{0.55}$ = 0.5
1	Continental						0.90/0.89/0.88/0.67 0.64/0.63/0.63/0.79
		Soluble	0.176	1.09	3.05	1.53-0.005i; Blue 1.53-0.006i; Green 1.53-0.006i; Red 1.42-0.01i; SWIR2	
		Dust	17.6	1.09	7.364	1.53-0.008i; Blue 1.53-0.008i; Green 1.53-0.008i; Red 1.22-0.009i; SWIR2	
		Soot	0.050	0.693	0.105	1.75-0.45i; Blue 1.75-0.44i; Green 1.75-0.43i; Red 1.81-0.50i; SWIR2	
2	Moderately absorbing / (Default)						0.93/0.92/0.91/0.87 0.68/0.65/0.61/0.68
		Fine	$0.0203\tau + 0.145$	$0.1365\tau + 0.3738$	$0.1642\ \tau^{0.7747}$	$1.43+0.05\tau - (0.002\tau+0.008)i$	
		Coarse	$0.3364\tau + 3.101$	$0.098\tau + 0.7292$	$0.1482\ \tau^{0.6846}$	$1.43+0.05\tau - (0.002\tau+0.008)i$	
3	Strongly Absorbing (Smoke)						0.88/0.87/0.85/0.70 0.64/0.60/0.56/0.64
		Fine	$0.0096\tau + 0.1335$	$0.0794\tau + 0.3834$	$0.1748\ \tau^{0.8914}$	$1.51 - 0.02i$	
		Coarse	$0.9489\tau + 3.4479$	$0.0409\tau + 0.7433$	$0.1043\ \tau^{0.6824}$	$1.51 - 0.02i$	
4	Weakly-absorbing (Urban/Industrial)						0.95/0.95/0.94/0.90 0.71/0.68/0.65/0.64
		Fine	$0.0434\tau + 0.1604$	$0.1529\tau + 0.3642$	$0.1718\ \tau^{0.8213}$	$1.42 - (-0.0015\tau+0.007)i$	
		Coarse	$0.1411\tau + 3.3252$	$0.1638\tau + 0.7595$	$0.0934\ \tau^{0.6394}$	$1.42 - (-0.0015\tau+0.007)i$	
5	Spheroid/ Dust						0.94/0.95/0.96/0.98 0.71/0.70/0.69/0.71
		Fine	$0.1416\ \tau^{-0.0519}$	$0.7561\ \tau^{0.148}$	$0.0871\ \tau^{1.026}$	$1.48\tau^{-0.021} - (0.0025\ \tau^{0.132})i$; Blue $1.48\tau^{-0.021} - 0.002i$; Green $1.48\tau^{-0.021} - (0.0018\ \tau^{-0.08})i$; Red $1.46\tau^{-0.040} - (0.0018\ \tau^{-0.30})i$; SWIR2	
		Coarse	2.2	$0.554\ \tau^{-0.0519}$	$0.6786\ \tau^{1.0569}$	$1.48\tau^{-0.021} - (0.0025\ \tau^{0.132})i$; Blue $1.48\tau^{-0.021} - 0.002i$; Green $1.48\tau^{-0.021} - (0.0018\ \tau^{-0.08})i$; Red $1.46\tau^{-0.040} - (0.0018\ \tau^{-0.30})i$; SWIR2	

Listed for each model are optical and physical properties for individual lognormal modes. Listed for each mode are the mean radius r_v, standard deviation σ of the volume distribution, and total volume of the mode, V_0. The complex refractive index is assumed constant all wavelengths (Blue, Green, Red, and SWIR2) unless otherwise noted, and the same values are assumed regardless of sensor's exact wavelength. The Absorbing and Moderately absorbing model parameters (r_v, σ, and k) are defined for $\tau \leq 2.0$; for $\tau > 2.0$, we assume $\tau = 2.0$. Likewise, the Non-absorbing and Spheroid model parameters are defined for $\tau \leq 1.0$. V_0 (for all models) is defined for all τ. The last column represents final spectral SSA (ω_0) and asymmetry parameter (g) for the combined modes, defined for $\tau = 0.5$, reported at MODIS wavelengths.

TABLE 7-2: AXIS RATIO DISTRIBUTION ASSUMED FOR DT-L COARSE/DUST MODEL

Axis Ratio	Frequency		Axis Ratio	Frequency
0.4019	0.14707		1.2	0
0.4823	0.10779		1.44	0.09063
0.5787	0.10749		1.728	0.14186

0.6944	0.06362		2.0736	0.16846
0.8333	0		2.48832	0.17308
1.0	0			

 Figure 7-2 shows the size distribution for the five AERONET-derived models for $\tau_{0.55} = 1.0$. Note the dynamic nature (function of τ) of the size properties of the fine models, especially the non-absorbing model. Figure 7-3 plots the phase function at 0.55 μm for each model as well as spectral dependence of three parameters (τ, ω_0, and g_0), for $\tau_{0.55} = 1.0$.
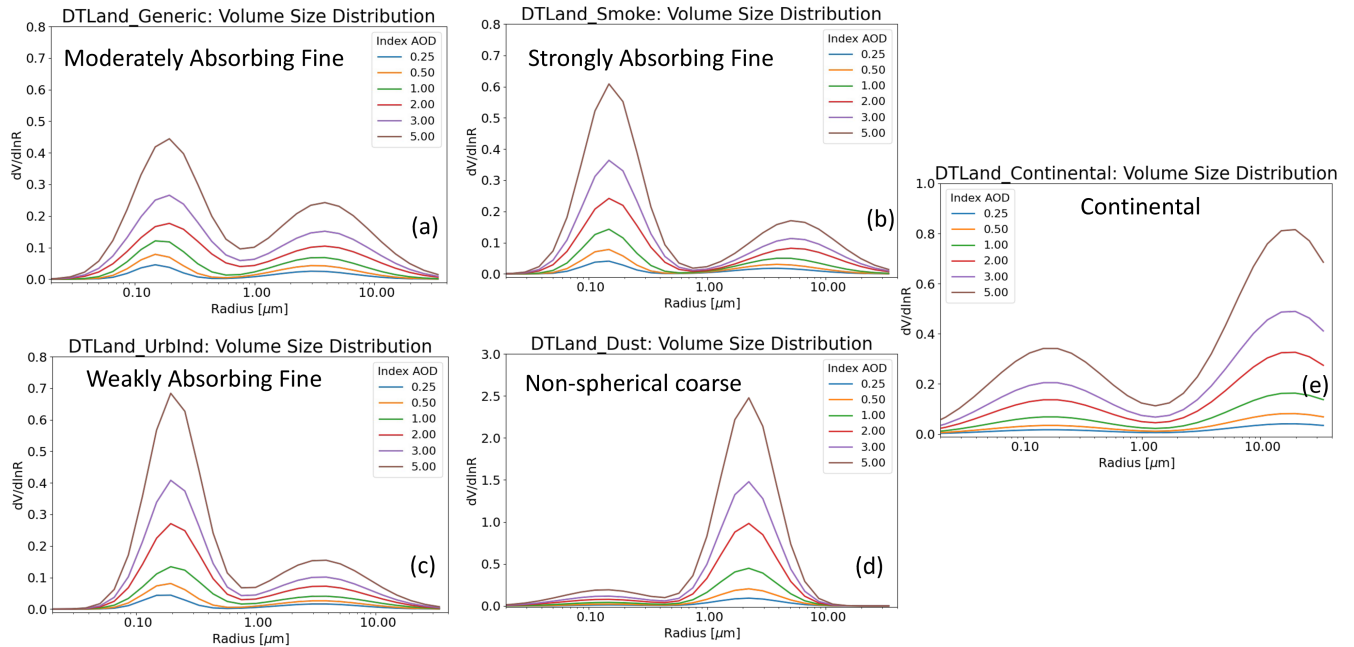
Figure 7-2: Plot of size distribution for the 5-aerosol model of the LUT as function of $\tau_{0.55}$. Note same y-scales for fine models (panels a-c), and different scales for coarse models (d) and Continental (e).

45
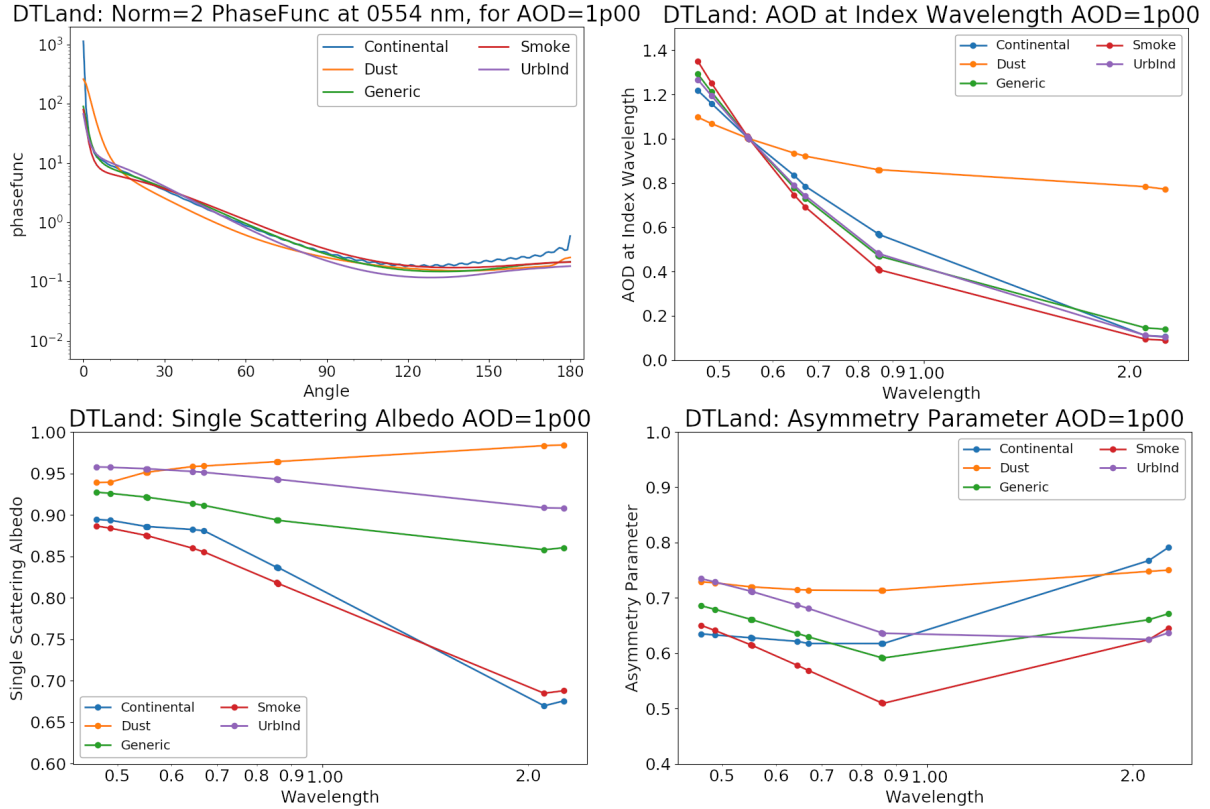
Figure 7-3: Plot of optical properties for the 5 aerosol models of the LUT, for $\tau_{0.55} = 1$. a) phase function at 0.55 μm (as a function of angle) b) optical depth spectral dependence, c) single scattering albedo spectral dependence and d) asymmetry parameter spectral dependence.

7.2.2. Reflectance-versus-Aerosol LUT

Our goal is to use Radiative Transfer (RT) code to simulate the TOA reflectance at a given wavelength, ρ_λ^*, which is a function of the atmospheric path reflectance ρ_λ^a, the up and down flux transmissions, $T_\lambda^\uparrow$ and $T_\lambda^\downarrow$, upscattering ratio $s_\lambda^\uparrow$ and surface reflectance, ρ_λ^s. The variables ρ_λ^a, $s_\lambda^\uparrow$, $T_\lambda^\uparrow$ and $T_\lambda^\downarrow$ are properties of the atmosphere, which depend on the coupling of the (vertical) profiles of the scattering of aerosols and air molecules. These all dependent on the angles, as well as the properties of the aerosols, and the profiles of the aerosols and Rayleigh contributions.

The at-launch MODIS lookup table (LUT) used a non-polarized (scalar) RT code [*Dave et al., 1970*]. Levy et al., [*2004*] demonstrated that under some geometries, neglecting polarization could lead to significant errors. Since MODIS Collection 5, we have used the vector (includes polarization) code known as RT3 [*Evans and Stephens, 1991*]. As described above, the fine-dominated aerosol models are assumed to be spherical particles, whereas the non-spherical particles are assumed as spheroid. For the spheres, we use MIEV [*Wiscombe, 1980*] to calculate the particle scattering properties (per size-parameter), and use the logic provided by Colarco et al. [*2003*] to integrate over size distribution. To calculate the scattering properties of the spheroids, we use the same T-matrix approximation code as used in Dubovik, Sinyuk, Lapyonok et al., [*DSL; 2006*], thus being consistent with the calculations used in AERONET retrieval. For each of the *j = 5* types, aerosol scattering properties are calculated for seven aerosol loadings defined by AOD at 0.55 *μm* (*t =1-7* representing $\tau_{0.55}$ = 0.0, 0.25, 0.5, 1.0, 2.0 3.0, and 5.0), and at four wavelengths (Blue, Green, Red, and SWIR2). The specific wavelengths

represent the centroid wavelengths based on reflectance spectral response (RSR) for the particular sensor's wavelength band (**Table 3-2**).

Whether from MIEV or DSL, we apply an external code to integrate over aerosol size distribution, define the vertical profile of both air molecules and aerosol, and couple the profiles of aerosol scattering with molecular (Rayleigh) scattering. Rayleigh optical depths are estimated via integrating Bodhaine et al. [*1999*] over sensor RSR, with U.S.-76 atmosphere (www.ngdc.noaa.gov) assumed as the profile. For the aerosol vertical profile, fine-dominated models are assumed to be exponential having scale height of 2km, whereas the dust/coarse model is assumed Gaussian at 3km.

For each of the 4 wavelengths and 35 aerosol type/loading combinations, RT is performed for combinations of 9 solar zenith angles (THET0 = θ_0 = *0°, 12°, 24°, 36°, 48°, 54°, 60°, 66°, 72°, 78° and 84°*), 16 sensor zenith angles (THETA = θ = *0° to 84°*; intervals of 6°), and 16 relative azimuth angles (PHI = ϕ = 0 to 180° increments of 12°).

The LUT is written into ASCII format. For example, the LUT's spectral path reflectances (aerosol plus Rayleigh over a black surface) $\rho_\lambda^{a,LUT''}$ are stored in arrays like

$$\boldsymbol{\rho^{a,LUT''}} = \boldsymbol{\rho_\lambda^{a,LUT''}(j, t, \theta_0, \theta, \phi)} \qquad\qquad \text{Eq. 7-4}$$

7.2.3. Prescribed aerosol type

For any retrieval, we assume the total aerosol will include a coarse-dominated model (dust) component and a fine-dominated model component. Since DT-L information content is insufficient for identifying "which" fine-model is present, we choose to prescribe it. Our method was laid out in Levy et al. [*2007a*], which essentially determined which of the three fine-dominated (spherical) aerosol types are most likely at each AERONET site for a given season. The default assignment is "generic/moderately absorbing" ($\omega_0 \sim 0.90$), but could be updated to either the "highly-absorbing" ($\omega_0 \sim 0.85$) or the "weakly-absorbing" ($\omega_0 \sim 0.95$) type if one of them dominated the AERONET retrievals at that site during the season. As expected, we found that the weakly-absorbing model (presumably urban/industrial aerosol) dominated the U.S. East Coast and far western Europe, and the highly-absorbing model (presumably incomplete biomass burning) dominated the savannas of South America and Africa. Most other sites were either dominated by moderately-absorbing type or were a mix of all clusters. Based on analysis of Version 1 AERONET data, simple boxes were drawn to be used in MODIS C5. Later analysis of Version 2 AERONET data led to some updates in model prescription, and contours that were hand-drawn. These Version 2 -derived maps were used to assign aerosol type for MODIS C6 and are used for all current DT-L retrieval versions.

Figure 7-4 prescribes the fine-dominated aerosol types around the globe, as a function of season. Red designates regions where the highly-absorbing aerosol is chosen, whereas green represents weakly-absorbing aerosol type. The moderately absorbing ($\omega_0 \sim 0.90$) model is assumed everywhere else. Note that where possible the selections represent the AERONET clustering. For some regions, however, subjectivity and/or intuition was required. For example, even though insufficient data exists for Africa north of the equator, the known surface types and seasonal cycles suggest that highly-absorbing aerosol should be produced during the biomass burning season. These hand-drawn contours are mapped onto a 1° longitude × 1° latitude grid, such that a fine aerosol model is assumed based on location and season.
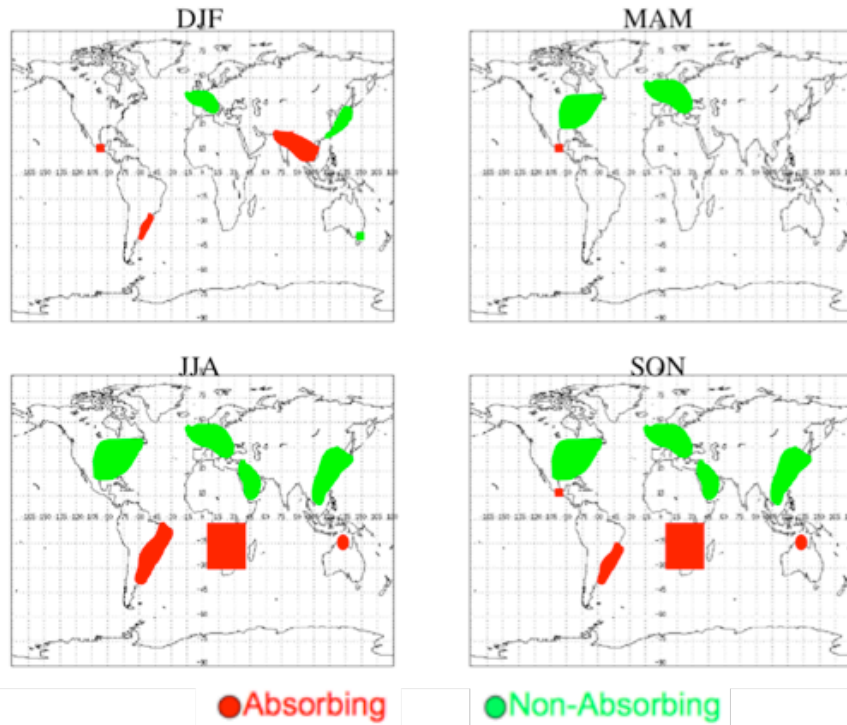
Figure 7-4: Final spherical aerosol model type designated at 1° × 1° gridbox per season. Red and green represent strongly-absorbing ($\omega_0 \sim 0.85$) or weakly-absorbing ($\omega_0 \sim 0.95$) models, respectively. Moderately absorbing ($\omega_0 \sim 0.90$) is assumed everywhere else.

7.3.   Surface Reflectance Parameterization (SRP) and Urban Correction:

When performing atmospheric retrievals from satellite observation, the major challenge is separating the contributions from the atmosphere and the surface. Over the ocean, the surface is nearly black (non-reflecting) at red wavelengths and longer, so that assuming negligible surface reflectance in these channels is a good approximation. Over land, however, the surface reflectance in the visible and SWIR may be far from zero and varies over surface type. As the land surface and the atmospheric signals are often comparable, errors of 0.01 in assumed surface reflectance will lead to errors on the order of 0.1 in τ retrieval. Errors in multiple wavelengths can lead to poor retrievals of spectral τ, which in turn would be useless for estimating size parameters. Fortunately, over vegetated, and dark soiled regions, the surface is generally "dark" and offers contrast for aerosol scattering. We may not be able to assume the surface reflectance, but Kaufman et al, [*1997b*] suggested how it could be constrained.

7.3.1. Background

Using aircraft observations, Kaufman and colleagues (e.g. *Kaufman et al., 1997b*) observed that over vegetated and dark soiled surfaces, the surface reflectance in some visible wavelengths (Blue and Red) were correlated with the surface reflectance in SWIR bands, specifically SWIR2 near 2.1 µm. Parallel simulations by vegetation canopy models showed that the physical reason for the correlation was the combination of absorption of visible light by chlorophyll and infrared radiation by liquid water in healthy vegetation [*Kaufman et al., 2002*]. Thus, the at-launch MODIS algorithm assumed that surface reflectance in the Blue (0.47µm) and the Red (0.65 µm) channels were one-quarter and one-half,

respectively, of the surface reflectance in the SWIR2 (2.11µm) channel *[Kaufman et al., 1997b]*. These relationships were noted as the VISvsSWIR surface reflectance ratios.

Earth's surface is not Lambertian, and some surface types exhibit strong angular dependence in its reflectance known as bi-directional reflectance functions (BRDF) [*Zhou et al. 2001*; *Lyapustin et al., 2001*]. Gatebe et al. [*2001*] flew the Cloud Absorption Radiometer (CAR) low over vegetated surfaces and found that the VISvsSWIR surface ratios varied as a function of angle. Remer et al., [*2001*] also noted that the VISvsSWIR surface ratios varied as a function of scattering geometry. When compared to ground-truth AERONET data, some of the MODIS product's biases appeared to be related to VISvsSWIR assumptions.

Atmospheric correction [AC; Kaufman and Sendra, 1988] can be used to theoretically "subtract the atmosphere" from the TOA signal and derive the surface. In other words, AC is equivalent to inverting

Eq. $\rho_\lambda^*(\tau_\lambda^a, \theta_0, \theta, \phi) = \rho_\lambda^a(\tau_\lambda^a, \theta_0, \theta, \phi) + \frac{T_\lambda^\downarrow(\tau_\lambda^a, \theta_0)T_\lambda^\uparrow(\tau_\lambda^a, \theta)\rho_\lambda^s}{1 - s_\lambda(\tau_\lambda^a)\rho_\lambda^s}$,   Eq. 2-26 and deriving ρ_λ^s. For the

purposes of DT retrieval, we are interested in deriving ρ_{Blue}^s, ρ_{Red}^s and ρ_{SWIR2}^s, and then determine if there are equations that describe global scenes. Levy et al., [*2007a*] performed AC using MODIS observations over AERONET sites (in clean conditions $\tau_{0.55} < 0.2$) to find that the VISvsSWIR relationships were more complicated than simple ratios. VISvsSWIR surface reflectance relationships appeared to have y-offsets, and there were dependencies on scene "greenness" and scattering angle. The resulting equations we denoted as the Surface Reflectance Parameterization (SRP).

7.3.2. Derivation of MODIS SRP

SRP derivation essentially is the act of inverting Eq. $\rho_\lambda^*(\tau_\lambda^a, \theta_0, \theta, \phi) = \rho_\lambda^a(\tau_\lambda^a, \theta_0, \theta, \phi) + \frac{T_\lambda^\downarrow(\tau_\lambda^a, \theta_0)T_\lambda^\uparrow(\tau_\lambda^a, \theta)\rho_\lambda^s}{1 - s_\lambda(\tau_\lambda^a)\rho_\lambda^s}$,   Eq. 7-5, to derive surface reflectance in multiple wavelength bands and finding relationships.

$$\rho_\lambda^*(\tau_\lambda^a, \theta_0, \theta, \phi) = \rho_\lambda^a(\tau_\lambda^a, \theta_0, \theta, \phi) + \frac{T_\lambda^\downarrow(\tau_\lambda^a, \theta_0)T_\lambda^\uparrow(\tau_\lambda^a, \theta)\rho_\lambda^s}{1 - s_\lambda(\tau_\lambda^a)\rho_\lambda^s},$$ Eq. 7-5,

For the TOA reflectance, we can use the equivalent to "Level 2 reflectances"– that is, the "Masked, sorted, and filtered within an N × N box" used for aerosol retrieval. The aerosol loading and optical properties are observed and/or assumed. Since AC is generally performed over AERONET ground sites, we know the actual AOD and can estimate the Rayleigh (molecular) optical depth (ROD) from the elevation/air pressure of the site.

While we know the AOD in specific sunphotometer wavelengths, we must interpolate or extrapolate to the specific satellite wavelengths. For that we need a description of aerosol type/model. Because LEO satellites (MODIS and VIIRS) both pass the equator within ±1.5 hours of noon, the sun often has a low zenith angle, and is not suitable for full sky (almucantar, Sinyuk et al. *[2020]*) inversions of AERONET observations. Therefore, without explicit knowledge of optical properties (size distribution, complex refractive index), AC must rely on sun-mode observations of AOD and AE and assume optical properties. Therefore, to minimize errors arising from unknown aerosol type and multiple scattering, we generally limit to conditions where $\tau_{0.55} < 0.2$. From the AERONET-derived Ångstrom exponent, we can decide whether to assume a fine model or a coarse model. Since ω_0 is not known, we assume the moderately-absorbing aerosol type ($\omega_0 \sim 0.9$) if AE suggests fine-dominated aerosol ($\alpha > 1.6$). When $\alpha < 0.6$ we can assume the coarse-dominated model. Co-locations where $0.6 < \alpha < 1.6$ should be considered "mixed" aerosol and were ignored for this exercise. Errors of aerosol type may not have too large an impact in visible wavelengths, but do their size differences,

coarse-dominated dust and fine-dominated smoke and pollution have huge differences when scattering SWIR.

For example, for $\tau_{0.55} = 0.2$, τ_{SWIR2} ranges from 0.03 to 0.16, depending on which aerosol model is assumed. Thus, assuming the wrong aerosol size in the correction procedure will lead to errors in estimating SWIR2 surface reflectance. An alternative method is to use only the Continental model, which is a default assumed by traditional atmospheric correction exercises, such as Vermote et al [*1997*] and 6S [*Kotchenova et al., 2007, Kotchenova and Vermote et al., 2006*]. However, there may be errors under both fine-dominated and coarse-dominated aerosol conditions.

Figure 7-5 shows the results from performing AC using Collection 4 MODIS data from both Terra and Aqua (colocations from 2000-2006), and then regressing derived surface reflectance for each of the VIS wavelengths to SWIR2 (Left) and then Blue to Red (Right). While not included here, also considered were the regressions if they were forced through zero, thereby assuming that zero SWIR reflectance is zero reflectance over the entire spectrum (which would be equivalent to deriving simple ratios). Correlation (R) values are 0.93 for the red, but only about 0.75 for the blue. Fitting Blue to Red has a higher correlation and less scatter than fitting Blue to SWIR directly. Therefore, the decision was to use two equations; one to derive Red from SWIR, and the second to derive Blue from Red.
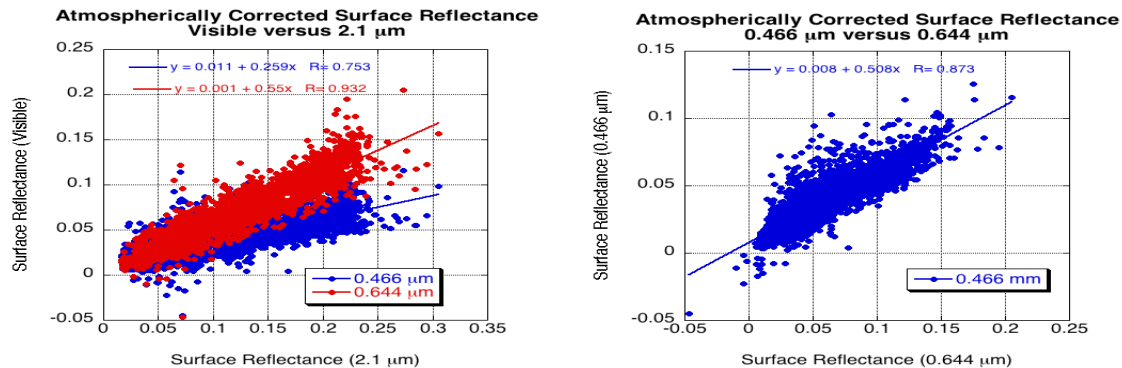

Figure 7-5: Atmospherically corrected surface reflectance in the visible (blue [0.466 µm] and red channels [0.644 µm]) compared with SWIR2 (2.1 µm) channel (a), and the blue compared with that in the red channel (b). Results from these plots were used for deriving SRP for MODIS Collection 5 [*Levy et al., 2009*].

Clearly, Figure 7-5 shows large scatter, so based on suspicion of angle dependencies and surface type, the SRP was further fine-tuned. Figure 7-6 plots the slope, y-offset, and correlation of the surface reflectance relationships, as a function of scattering angle. The RedSWIR regression slope shows dependence on scattering angle, whereas the BlueRed regression slope shows nearly none. The regressed y-intercept shows strong dependence on scattering angle for both relationships. Especially interesting is that the RedSWIR y-offset goes from positive to negative with increasing scattering angle, with a value of zero near $\Theta = 135°$. Note that current DT algorithm uses the SRPs analyzed from the MODIS Collection 5. The SRP analysis with VIIRS and GEO sensors are shown in Appendix 7.
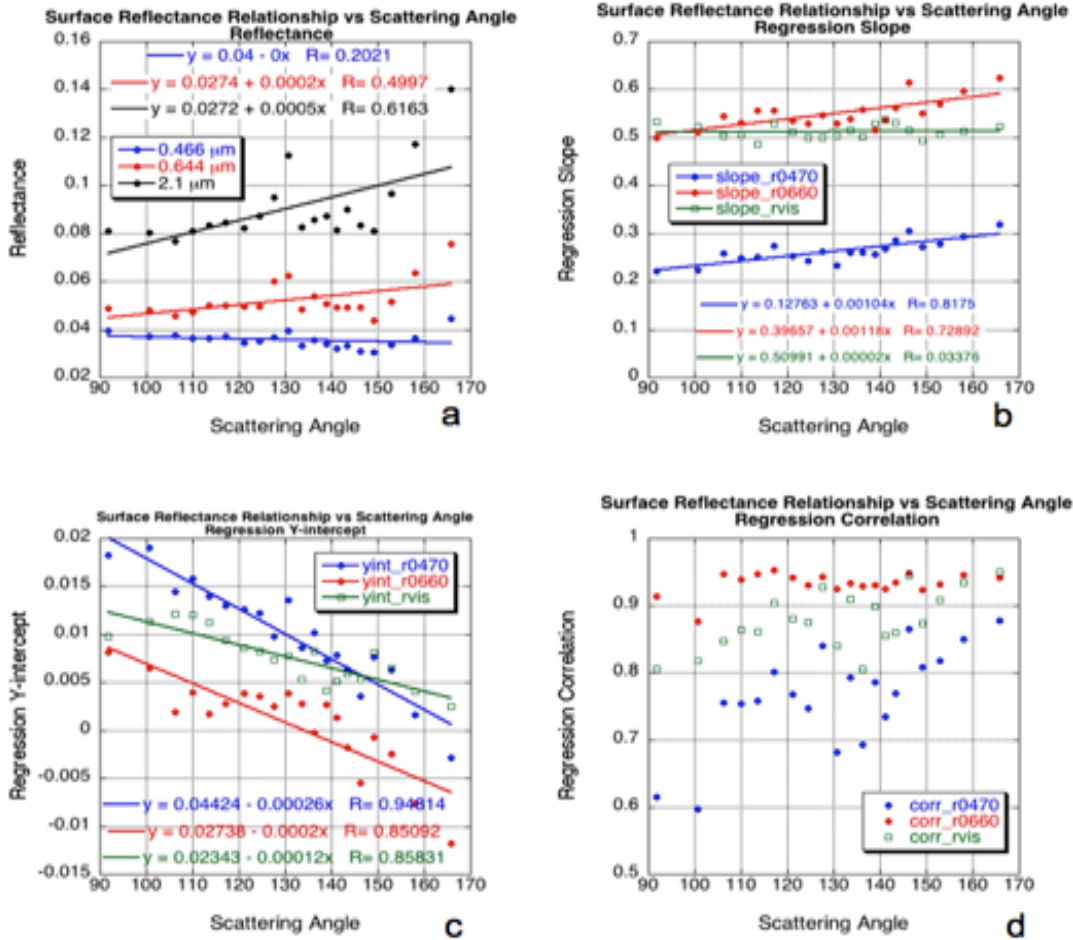
Figure 7-6: VISvsSWIR surface reflectance relationships as a function of scattering angle, originally used for deriving SRP used for MODIS, Collection 5. The data were sorted according to scattering angle and put into 20 groups of equal size (about 230 points for each scattering angle bin). On all subplots, each point is plotted for the median value of scattering angle in the bin. Part (a) plots median values of reflectance at each channel as a function of the scattering angle. Linear regression was calculated for the 230 points in each group. The slope of the regression (for each angle bin) is plotted in (b), the y-intercept is plotted in (c) and the regression correlation is plotted in (d). Note for (b), (c) and (d) that 0.47 μm vs 2.11 μm (r0470) is plotted in blue, 0.65 μm vs 2.11 μm (r0660) is plotted in red and 0.47 vs 0.65 μm (rvis) is plotted in green.

Because AERONET sites are located in different surface type regimes, it was suspected that the VISvsSWIR surface relationships may vary based on surface type and/or season. A strong indicator of vegetation/surface condition is its Normalized Difference Vegetation Index (NDVI). Often NDVI is estimated based on comparing satellite-observed (TOA) reflectance values in Red and NIR wavelength bands, however [*Karnieli, et al., 2001*] noted that using longer wavelength bands helps to reduce uncertainties due to aerosols (what we are trying to measure!). Therefore, we define the $NDVI_{SWIR}$ based on measured (gas-corrected) NIR1 and SWIR2:

$$NDVI_{SWIR} = \left(\rho_{NIR1}^{obs} - \rho_{SWIR2}^{obs}\right)/\left(\rho_{NIR1}^{obs} + \rho_{SWIR2}^{obs}\right) \qquad \text{Eq. 7-6}$$

This index is also known as $NDVI_{SWIR}$ (Mid-InfraRed). In aerosol free conditions $NDVI_{SWIR}$ is highly correlated with regular *NDVI*. A value of $NDVI_{SWIR} > 0.6$ is active vegetation, whereas $NDVI_{SWIR} < 0.2$ is representative of dormant or sparse vegetation. Figure 7-7 plots the relationship of

Red and SWIR (atmospherically corrected) surface reflectance relationship, for nonurban sites, as a function of low, medium and high values of $NDVI_{SWIR}$. Clearly, as the $NDVI_{SWIR}$ increases, the ratio between Red and SWIR surface reflectance increases, and we use this relationship in the final VISvsSWIR surface reflectance parameterization. Since the BlueRed relationship does not strongly vary as a function of $NDVI_{SWIR}$, we assumed it to be constant.
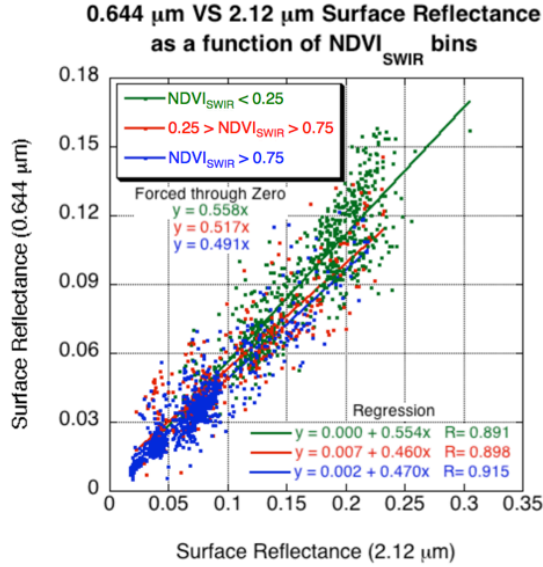

Figure 7-7: 0.65 μm versus 2.12 μm surface reflectance as a function of bins of NDVI_SWIR values (low, medium, and high). Both standard regression and "forced through zero" are plotted.

Results of the global atmospheric correction exercise imply they have a strong dependence on both geometry and surface greenness. For MODIS, the VISvsSWIR surface reflectance relationship is parameterized as a function of both $NDVI_{SWIR}$ and scattering angle Θ:

$$\rho^s_{Red} = \rho^s_{SWIR2} \times slope_{RedSWIR2} + yint_{RedSWIR2},$$

$$\rho^s_{Blue} = \rho^s_{Red} \times slope_{BlueRed} + yint_{BlueRed}, \qquad \text{Eq. 7-7}$$

where

$$slope_{RedSWIR2} = slope^{NDVI_{SWIR}}_{RedSWIR2} + 0.002\Theta - 0.27,$$

$$yint_{RedSWIR2} = -0.00025\Theta + 0.033,$$

$$slope_{BlueRed} = 0.49,$$

and

$$yint_{BlueRed} = 0.005, \qquad \text{Eq. 7-8}$$

where in turn

$$slope^{NDVI_{SWIR}}_{RedSWIR2} = 0.58, if\ NDVI_{SWIR} < 0.25,$$

$$slope^{NDVI_{SWIR}}_{RedSWIR2} = 0.48, if\ NDVI_{SWIR} > 0.75,$$

$$slope^{NDVI_{SWIR}}_{RedSWIR2} = 0.58 - 0.2(NDVI_{SWIR} - 0.25), if\ 0.25 \leq NDVI_{SWIR} \leq 0.75. \text{Eq. 7-9}$$

Note that while the above parameterization was based on the results of Figure 7-5 through Figure 7-7, the coefficients are not identical to those in the figures. The atmospherically corrected data set is the broadest and most comprehensive representation of global surface reflectance relationships available to us. However, it is limited to AERONET site locations, which are in turn are most concentrated in certain geographical regions. Trial and error were used to modify the basic results from the AERONET-based atmospheric correction, to give more realistic retrievals globally, especially in areas with few or no AERONET sites.

7.3.3. Urban Percentage Map and Urban SRP

Beginning with MODIS C61 product, Gupta et al., [2016] noted that DT could be improved if it could account for urban surfaces in an otherwise "dark" scene. Using the International Geosphere/Biosphere Programme's (IGBP) scene map of USGS surface types, which is provided by MODIS Land Cover Type product (MCD12Q1) for the year 2011, at 500 m resolution, we determined the scene type of the MODIS/AERONET co-location box. The land cover class defined as "urban and built-up" has been extracted and urban percentage (UP) at $0.1° \times 0.1°$ resolution (approximately equivalent to the 10 km MODIS AOD products resolution) is reported as a fixed map.

Figure 7-8 provides the surface reflectance spectral relationships between VIS and SWIR, defined for the four different categories based on the combinations of NDVI$_{SWIR}$ and UP. The four regression lines in the figures are calculated for each of the four categories using bins of equal number of points. We still derive the regression coefficients from the cloud of points (shown as gray color) but bin the data to help visualize the differences from regime to regime. We note that the slopes of the regression between the blue and red wavelengths are not strongly dependent on differences in the UP or the NDVI$_{SWIR}$, as long as UP > 20%. However, the regressions between the red and SWIR wavelengths are indeed dependent on the nuances of the urban surface.
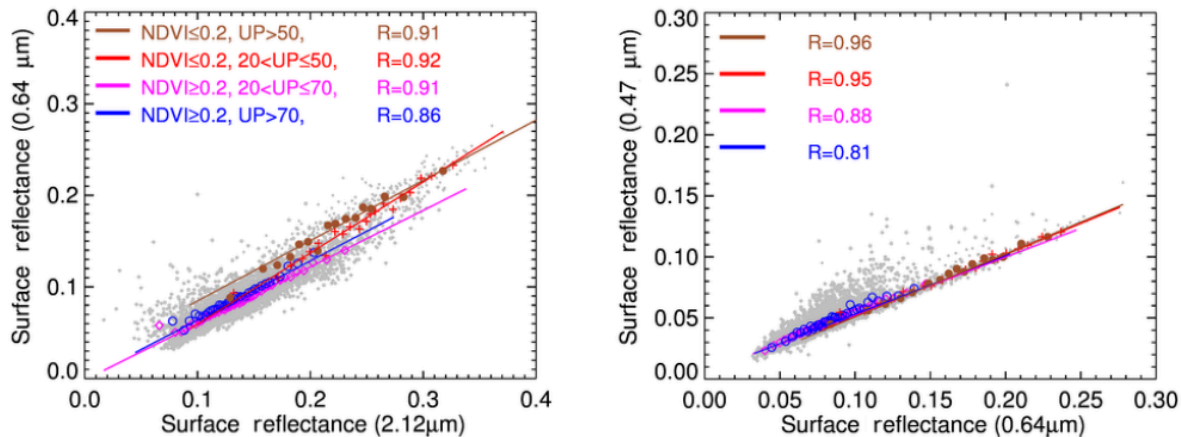

Figure 7-8: The red (0.65 µm) vs. SWIR2 (2.11 µm) surface reflectance (left panel) and the blue (0.47 µm) vs. red (0.65 µm) surface reflectance (right) for four different combinations of NDVISWIR and UP values. Each combination of NDVISWIR and UP values is color-coded and plotted as a different symbol. The standard regression using least absolute deviation method applied and the resulting regression lines are plotted. The linear correlation coefficient (R) is presented in the figure. [*Gupta et al., 2016*; Figure2]

Taking into account the regression changes in UP and NDVI$_{SWIR}$, we apply the urban to the pixel with UP larger than 20% as follows:

$$slope_{RedSWIR2}^{NDVI_{SWIR}} = 0.78 \text{ and } yint_{RedSWIR2}^{NDVI_{SWIR}} = -0.02, \text{ if } 20\% \leq UP < 50\%,$$

53

$$slope_{RedSWIR2}^{NDVI_{SWIR}} = 0.66 \text{ and } yint_{RedSWIR2}^{NDVI_{SWIR}} = 0.02, \text{ if } UP \geq 50\%, \qquad \text{Eq. 7-10}$$

$$slope_{BlueRed}^{NDVI_{SWIR}} = 0.51, \qquad \text{if } 20\% \leq UP < 50\%,$$
$$slope_{BlueRed}^{NDVI_{SWIR}} = 0.52, \text{ if } UP \geq 50\% \qquad \text{Eq. 7-11}$$

and where $NDVI_{SWIR} \geq 0.20$,

$$slope_{RedSWIR2}^{NDVI_{SWIR}} = 0.62 \text{ and } yint_{RedSWIR2}^{NDVI_{SWIR}} = 0.0, \text{ if } 20\% \leq UP < 70\%,$$
$$slope_{RedSWIR2}^{NDVI_{SWIR}} = 0.65 \text{ and } yint_{RedSWIR2}^{NDVI_{SWIR}} = 0.0, \text{ if } UP \geq 70\%. \qquad \text{Eq. 7-12}$$

$$slope_{BlueRed}^{NDVI_{SWIR}} = 0.47, \qquad \text{if } 20\% \leq UP < 70\%$$
$$slope_{BlueRed}^{NDVI_{SWIR}} = 0.48, \text{ if } UP \geq 70\% \qquad \text{Eq. 7-13}$$

7.3.4. Applying DT SRP for Other Sensors

In order to continue the aerosol data record after the decommissioning of the MODIS missions on both Terra and Aqua, the DT algorithm is being ported to other sensors, VIIRS [*Levy et al., 2015; Sawyer et al., 2020*], AHI [*Gupta et al., 2019*], and ABI [*Kim et al., 2024*]. The DT surface assumption on VIIRS, ABI, and AHI generally follows the MODIS-based SRP. However, it seems an adjustment of SRP is necessary according to the sensor specifications.

Although the new advanced imagers observe a similar spectral range (visible through thermal infrared) as MODIS, there are generally fewer bands in total, and the wavelength range of analogous bands are shifted as described in **Table 3-2**. For VIIRS, the wavelength shifts in blue, red, and SWIR channel increase the regression slope in both Red-SWIR2 and Blue-Red relation to 0.56 and 0.65, respectively. Levy et al. [*2015*] and Sawyer et al. [*2020*] showed that the minimal change to SRP and slight adjustments for wavelength band, one could derive a VIIRS AOD product that had error/bias statistics similar to the MODIS product. For ABI and AHI, due to the lack of a NIR1 = 1.24 μm channel, we defined NDVI$_{GEO\_SWIR}$ to use NIR (~0.86 μm) instead. While not as "aerosol-free", vegetation reflects NIR similarly to NIR1 [*Miura et al., 1998*].

$$NDVI_{GEO\_SWIR} = (\rho_{NIR}^{obs} - \rho_{SWIR2}^{obs})/(\rho_{NIR}^{obs} + \rho_{SWIR2}^{obs}) \qquad \text{Eq. 7-14}$$

There are much larger differences in ground sampling and viewing geometry between LEO and GEO. Therefore, the SRPs optimized for MODIS or similar LEO sensors do not appear be appropriate for GEO. For example, Gupta et al. [*2019*] finds biases in the DT-algorithm applied to AHI. Also, when analyzing NOAA's aerosol products created from ABI in the GOES-East position (e.g. ABI-E), Zhang et al. [*2020*] shows the need for an empirical correction to improve mean bias and Root Mean Squared Error (RMSE). Kim et al. [*2024*] finds that using MODIS-based SRP leads to higher biases and artificial diurnal signatures in aerosol retrievals from ABI-E. We hypothesize that the diurnal signature in bias between each ABI and AERONET arises because the viewing geometry of the GEO sensor has different features than from the LEO one. For GEO sensors, a particular ground site is always observed with the same viewing angle while the sun angles change throughout the day. GEO sensor observes each ground pixel with a fixed VZA, and therefore each VZA matches up to a specific land cover type according to location. In contrast, since MODIS has a 16-day orbit repeat cycle (https://ladsweb.modaps.eosdis.nasa.gov/missions-and-measurements/modis/), a particular ground target will be observed from a variety of VZA, while the SZA is relatively constant during a season.

Thus, any residual bias escaping the LEO SRP's compensation for anisotropic surface reflectance by assuming a dependency on scattering angle will be averaged out over MODIS's 16-day repeat cycle but be reinforced day after day with GEO. From this point of view, we suspect that while assuming that the scattering angle represents the anisotropic reflectance pattern may work for MODIS on average, it would induce a large bias to GEO retrievals at local noon and/or dawn and dusk. This means we should consider a new SRP for ABI observations that covers the new geometry. Kim et al., [*2024*] tests a new SRP considering its change with land cover type, and then shows that it reduces biases and mitigates the bias's diurnal signature in retrieved AOD.

7.4. Retrieval Algorithm Mechanics

7.4.1. Mask, Sort, Filter the N × N Pixels

Referring back to the flowchart in Fig 7.1, If there are any "land" pixels within the N × N box, the DT-L subroutine receives relevant observation and geolocation data. These include the gas-absorption-corrected Blue, Red, and SWIR2 reflectances directly used in the aerosol retrieval, the NIR and/or NIR1 reflectances for inland water masking and deriving the SRP, as well as thermal IR radiances for snow/ice masking. Appendix 3.2 describes details in over land masking, including cloud mask, snow/ice mask, and inland water mask. Inputs also include observation angles (θ, θ_0 and ϕ), latitude/longitude, surface elevation, and day of year. Finally, DT-L receives the pre-computed cloud mask and defined land/sea mask.

From the N × N box of reflectances, ρ_λ^{L1B}, all pixels pre-determined as "permanent inland water", "ice/snow" or "clouds" are discarded. Next applied are additional tests for determining inland water. Appendix 3.2 describes all masks applied to over land pixels. All failed pixels are discarded.

The remaining pixels are sorted by their SWIR2 measured reflectance (ρ_{SWIR2}^{L1B}). The brightest 50% and darkest 20% are discarded, which is intended to reduce uncertainty due to clouds, bright surfaces, and shadows within the box. Assuming no pixels were masked already (clouds, ice/snow, water) by the initial screening this leaves at most 30% of the original N × N pixels for retrieval. Of course, there may be fewer.

After the SWIR2 sorting, the remaining pixels are separated into two groups, 'dark' pixels having $0.01 \le \rho_{SWIR2}^{L1B} \le 0.25$ and 'less dark' pixels with $0.25 < \rho_{SWIR2}^{L1B} < 0.4$. If at least 3% of the original N×N (10% of the 30%) are considered 'dark', the aerosol retrieval continues down the standard path, which is known as Procedure A (ProA). If fewer 'dark' pixels are available, but there are sufficient 'less dark' pixels to get to 3%, Procedure B (ProB) is followed.

In either case, the remaining pixels are collected and counted, so that the average (and standard deviation) of reflectance is calculated for each wavelength band. This means Blue, Red, SWIR2 and NIR bands for all sensors, and Green, and SWIR1 for sensors with these bands. We also carry forward the statistics of SWIR1 (e.g. 1.6 μm). Let us denote this set of spectral reflectance as Mean_Reflectance_Land, with the symbols ρ_λ^{obs}. NDVI$_{SWIR}$ is calculated from the ρ_λ^{obs}, using SWIR1 if available and NIR if not.

7.4.2. Reduce Aerosol LUT

Assuming sufficient N × N pixel availability, computer memory requires that the aerosol reflectance LUTs are reduced. The first step is to select the appropriate aerosol model types and (if MODIS C6.1 version) identify Urban Percentage (UP) from maps. If following ProA, the Fine-dominated aerosol model type is selected from the 1° × 1° map, and the Coarse-dominated model is

already chosen. If following ProB, only the Continental model is selected. All other types are discarded.

Next, the Fine and Coarse (or Continental only) LUTs are interpolated to the exact angles of the observation, leaving $\rho_\lambda^{a,LUT\prime}$ for fine and coarse models.

$$\boldsymbol{\rho^{a,LUT\prime} = \rho^{a,LUT\prime,f}(t = 7\ loadings)} \text{ and } \boldsymbol{\rho_\lambda^{a,LUT\prime,c}(t = 7\ loadings)} \qquad \text{Eq. 7-15}$$

where the 4 wavelengths are Blue, Green=0.55 μm, Red, and SWIR2 for the specific sensor. The other parameters which are function of models and angles (Up/down fluxes, upscattering albedos $T_\lambda^\downarrow, T_\lambda^\uparrow, s_\lambda$) are also interpolated accordingly.

7.4.3. Correcting the LUT for Elevation

The LUTs are defined to include the molecular reflectance for the entire atmospheric column, which is defined for the sea-level Rayleigh Optical Depth (ROD). For an elevated surface such as a mountain, there is less atmosphere, lower ROD, and less molecular scattering. Also the phase functions for aerosol and Rayleigh scattering are different. Thus, the errors to estimating TOA reflectance can be significant. While the most accurate solution is to derive path reflectance and transmission functions for different elevations and/or RODs, this would require an additional dimension to the LUT. Instead we use an approximation.

The sea-level Rayleigh optical depth (ROD, τ_λ^R) at a wavelength λ (in μm) can be approximated over the visible range (e.g. Dutton et al., [*1994*]; Bodhaine et al., [*1999*]) by:

$$\tau_\lambda^R = 0.00877\ \lambda^{-4.05} \qquad \text{Eq. 7-16}$$

When not at sea level (pressure = 1013 mb), the ROD is a function of pressure (or height, z) so that it can be approximated by:

$$\tau_\lambda^R(z = Z) = \tau_\lambda^R(z = 0)e^{-Z/8.5} \qquad \text{Eq. 7-17}$$

where Z is the height (in kilometers) of the surface target and 8.5 km is the exponential 'scale height' of the atmosphere. The difference between ROD at $z = 0$ and $z = Z$ is $\Delta\tau_\lambda^R$.

The DT-L algorithm makes use of the procedure described in Fraser et al. [*1989*], essentially adjusting the lookup table to simulate different ROD by adjusting the wavelength. Substitution of Eq. $\tau_\lambda^R(z = Z) = \tau_\lambda^R(z = 0)e^{-Z/8.5}$ Eq. 7-17 into Eq. $\tau_\lambda^R = 0.00877\ \lambda^{-4.05}$ Eq. 7-16 yields

$$\lambda(z = Z) = \lambda(z = 0)e^{-Z/34} \qquad \text{Eq. 7-18}$$

For example, at $\lambda = 0.466\ \mu m$ (the Blue MODIS channel) sea-level ROD is about 0.192. For a 1 km mountain, the ROD at this wavelength is only 88% or about 0.170. This is the same ROD is observed at sea-level at $\lambda = 0.481\ \mu m$. In other words, we can approximate the Rayleigh scattering of an elevated surface by adjusting the wavelength. Fortunately, within the framework of the DT LUT, we have available information.

Assuming that gases and aerosols are optically well mixed in altitude, the algorithm substitutes for the parameter values of the Blue channel LUT by interpolating (linearly as functions of log wavelength and log parameter) between the Blue and the next in line, e.g. the Green (= 0.55 μm) wavelength entries. Similar interpolations are performed for the other channels (for example, 0.55 μm could be adjusted to 0.565 μm) using the Red, and Red would be interpolated using SWIR. This means that lower values of TOA atmospheric path reflectance and higher values of transmission would be chosen to represent a given aerosol model's optical contribution. However, also note that since the 0.55 μm channel has also been adjusted, the associated values of the τ indices have been adjusted accordingly. For example, for Green band index of 0.25, τ for fine-dominated, weakly absorbing aerosol, extinction spectral dependence leads to 0.335 at $\lambda = 0.466\ \mu m$. This corresponds to 0.238 at $\lambda = 0.565\ \mu m$

and 0.317 at $\lambda = 0.481\ \mu m$. At the τ entry becomes 0.238. However, uncertainties in aerosol versus Rayleigh phase functions would be at least partially compensated by picking a larger total AOD to fit the TOA reflectance solutions.

Whereas most global land surfaces are at sea level or above, a few locations are below sea level ($Z < 0$). In these cases, the algorithm is allowed to extrapolate below $0.466\ \mu m$. Since the extrapolation is at most for a hundred meters or so, this is not expected to introduce large errors, and these cases can still be retrieved. Due to the extremely low ROD in the $2.11\ \mu m$ channel we do not adjust this value.

The "adjusted" LUTs are sent to the inversion. The wavelength interpolation is assumed for the other parameters (fluxes, transmissions and upscattering albedo)

7.5. Inversion

7.5.1. ProA: Inversion for Darker Surfaces

If following ProA (for darker surfaces), we report the number of "good" pixels that are left over after all discards. While the atmospheric contribution to SWIR2 observation may be small it is not negligible. Thus, we do not know the surface contribution. However, we have the SRP to constrain the total reflectance in the three channels (Blue, Red, and SWIR2). Allowing the Fine Model Fraction η to vary at discrete intervals also helps constrain the solution.

Therefore, ProA proceeds as follows:

For discrete values of η between -0.1 and 1.1 (intervals of 0.1), the algorithm attempts to find the τ at $0.55\ \mu m$ and the surface reflectance in SWIR2 that exactly matches the satellites measured Blue channel reflectance. (Note that the algorithm also tries non-physical values of η (1.1 and -0.1) to allow for uncertainties to either aerosol models or surface reflectance. There will be some error, ε at red. The solution is the one where the error at red is minimized. In other words,

$$\rho_{Blue}^{obs} - \rho_{Blue}^{TOA} = 0$$

$$\rho_{Red}^{obs} - \rho_{Red}^{TOA} = \varepsilon \qquad\qquad \text{Eq. 7-19}$$

$$\rho_{SWIR2}^{obs} - \rho_{SWIR2}^{TOA} = 0$$

where

$$\rho_{SWIR2}^{TOA} = \eta\left(\rho_{SWIR2}^{a,f} + \frac{F_{d,SWIR2}^f T_{SWIR2}^f \rho_{SWIR2}^f}{1 - s_{SWIR2}^f \rho_{SWIR2}^f}\right) + (1-\eta)\left(\rho_{SWIR2}^{a,c} + \frac{F_{d,SWIR2}^c T_{SWIR2}^c \rho_{SWIR2}^c}{1 - s_{SWIR2}^c \rho_{SWIR2}^c}\right)$$

$$\rho_{Red}^{TOA} = \eta\left(\rho_{Red}^{a,f} + \frac{F_{d,Red}^f T_{Red}^f \rho_{Red}^f}{1 - s_{Red}^f \rho_{Red}^f}\right) + (1-\eta)\left(\rho_{Red}^{a,c} + \frac{F_{d,Red}^c T_{Red}^c f(\rho_{Red}^c)}{1 - s_{Red}^c \rho_{Red}^c}\right)$$

and

$$\rho_{Blue}^{TOA} = \eta\left(\rho_{Blue}^{a,f} + \frac{F_{d,Blue}^f T_{Blue}^f \rho_{Blue}^f}{1 - s_{Blue}^f \rho_{Blue}^f}\right) + (1-\eta)\left(\rho_{Blue}^{a,c} + \frac{F_{d,Blue}^c T_{Blue}^c g(\rho_{Blue}^c)}{1 - s_{Blue}^c \rho_{Blue}^c}\right) \qquad \text{Eq. 7-20}$$

where in turn, $\rho^a = \rho^a(\tau)$, $F = F(\tau)$, $T = T(\tau)$, $s = s(\tau)$ are functions of τ indices in the LUT, and $f(\rho_{SWIR2}^s)$, $g(\rho_{Blue}^s)$ are SRP described in Section 7.3. Again, the primary products are τ ($\tau_{0.55}$), η ($\eta_{0.55}$), and the surface reflectance (ρ_{SWIR2}^s). The error ε is also noted.

7.5.2. Procedure B: Alternative Retrieval for Less-dark Surfaces

The derivation of aerosol properties is possible when the 2.11 μm reflectance is brighter than 0.25 but is expected to be less accurate [*Remer et al., 2005*], due to increasing errors in the VISvsSWIR SRP. However, if Procedure A is not possible, and if there are at least 3% (12 out of 400 for MODIS) cloud-screened, non-water pixels, satisfying:

$$0.25 < \rho_{SWIR2}^{obs} < 0.25G < 0.40 \qquad \text{Eq. 7-21}$$

where G is the "air mass factor" defined by:

$$G = \frac{1}{2}\left(\frac{1}{\mu} + \frac{1}{\sqrt{\mu_0}}\right) \qquad \text{Eq. 7-22}$$

then ProB is attempted.

ProB is analogous to 'Path B' described in Remer et al., [*2005*]. Only the Continental aerosol model is assumed, and the SRP is the same. There is no Fine-Model Weighting necessary, so $\eta = 1.0$. The primary products for ProB are $\tau_{0.55}$ and the surface reflectance ρ_{SWIR2}^s. The 'land fitting error' ε is also saved.

7.5.3. Note about Negative AOD Retrievals

DT-L permits small-magnitude negative τ retrievals. Given that there is both positive and negative noise in the MODIS observations, and that surface reflectance and aerosol properties may be under or over-estimated depending on the retrieval conditions, it is statistically useful to allow retrieval of negative τ. In fact, it is necessary for creating an unbiased dataset from any instrument. Without negative retrievals the τ dataset is biased by definition.

The difficulty here is to distinguish between a retrieved τ that is truly close to zero and an erroneous retrieved τ. Since we assume that MODIS should retrieve between the expected error defined by $\pm 0.05 \pm 0.15\tau$, for very clean conditions when $\tau \sim 0$ there is essentially no difference between retrievals in the range of -0.05 to +0.05. All negative values -0.05 to 0 are reported with QAC rated 'good' (QAC = 3). Retrievals in the range -0.10 to -0.05 are reported as -0.05 and assigned to QAC = 0. Retrievals less than -0.10 are regarded as 'out of range' and are not reported. Other products that are retrieved or derived (such as the η) are set to zero or reported as not defined when the retrieved τ is negative.

In cases where low τ is retrieved ($\tau < 0.2$), the η is expected to be too unstable to be retrieved with any accuracy. Therefore, η is reported as un-defined.

7.6.   Derivation of Fine Mode τ, Mass Concentration and Other Secondary Parameters

Following the derivation of primary products by ProA ($\tau_{0.55}, \eta_{0.55}, and \ \rho_{SWIR2}^s$) a number of secondary products can also be calculated. These include the fine and coarse model optical depths $\tau_{0.55}^f$ and $\tau_{0.55}^c$

$$\tau_{0.55}^f = \tau_{0.55}\eta_{0.55} \ \text{ and } \ \tau_{0.55}^c = \tau_{0.55}(1 - \eta_{0.55}) \qquad \text{Eq. 7-23}$$

the 'mass concentration', *M* is

$$M = M_c^f \tau_{0.55}^f + M_c^c \tau_{0.55}^c \qquad \text{Eq. 7-24}$$

the spectral total, fine and coarse model optical thicknesses τ_λ, τ_λ^f, and τ_λ^c show relation:

$$\tau_\lambda = \tau_\lambda^f + \tau_\lambda^c \qquad\qquad \text{Eq. 7-25}$$

where

$$\tau_\lambda^f = \tau_{0.55}^f\left(Q_\lambda^f/Q_{0.55}^f\right) \; and \; \tau_\lambda^f = \tau_{0.55}^c(Q_\lambda^c/Q_{0.55}^c) \qquad\qquad \text{Eq. 7-26}$$

the Ångstrom Exponent α:

$$\alpha = \frac{\ln\left(\tau_{0.55}/\tau_{red}\right)}{\ln\left(0.55/red \text{ wavelength}\right)} \qquad\qquad \text{Eq. 7-27}$$

and the spectral surface reflectance ρ_λ^s, computed by re-arranging Eq. 7-7 – Eq 7-9 and Eq 7-10 – 7-13 if Urban surface with MODIS. M_c^f and M_c^c are mass concentration coefficients for the fine and coarse models (see Appendix 4), whereas Q_λ^f and Q_λ^c represent model extinction coefficients at wavelength, λ. See Appendix 4 for derivation of the extinction coefficients.

If Procedure B was followed, the only secondary products calculated are M and $\tau_{0.55}$, and the QAC is set to 0. The other products are undefined.

7.7. Retrieved Land Products

Two primary retrieved products of the land algorithm are the total AOD at green ($\tau_{0.55}$) and surface reflectance at ρ_{SWIR3}^s). **Table 7-3** lists the aerosol over land products for MODIS C6 and **Table 7-4** lists side by side comparisons of DT over land products parameters between MODIS C6 versus VIIRS/ABI/AHI. For each product, the table lists its name within the file, its dimension, and its "type." All products are at least two-dimensional (nominally 135 x 204 at 10 km x 10 km resolution), and many have three dimensions. If there is a third dimension, the channels (usually wavelengths) are listed. A parameter's type may be Retrieved, Derived, Diagnostic, Experimental, or Joint Land and Ocean. A *Retrieved* parameter is one that is a solution to the inversion (ProA). *Derived* parameters are computed based on products directly retrieved. Products that are *Diagnostic* include QA parameters and those parameters that were calculated during intermediate steps. These diagnostic parameters can be used to understand how the retrieval worked. Note that a parameter's type does not signify that the parameter should be used in a quantitative way. Each parameter should be independently validated through comparison with ground-truth. Validation and evaluation of $\tau_{0.55}$ is shown in Section 9, other parameter are subjects of future studies, and will be appended as needed in that section.

Finally, the *Joint* products are those that are composites of over-land and over-ocean aerosol retrievals. For example, Image_Optical_Depth_Land_And_Ocean includes all $\tau_{0.55}$ data from 'Corrected_Optical_Depth_Land' including those with QAC=0. This product provides a full picture of the aerosol distribution, even if some of the retrievals are more qualitative in nature than the validated quality assured data. The 'Optical_Depth_Land_And_Ocean' product is designed to include the more quantitative data, and is filtered for higher QAC. Based on evaluation of the operational C5-L data stream, the recommended QAC filter used for the 'Optical_Depth_Land_And_Ocean' product is QAC > 0 over ocean and QAC = 3 over land.

TABLE 7-3: CONTENTS OF MODIS C6.1 AEROSOL LEVEL 2 FILE (MOD04/MYD04): DARK TARGET LAND PRODUCTS

Symbol	Name of Product (SDS)	Dimesions: 3rd Dimension	Type of product
τ_λ^{avg}	Corrected_Optical_Depth_Land		Retrieved
		X,Y,3: 0.47, 0.55, 0.65 µm	Primary
$\tau_{2.1}^{avg}$	Corrected_Optical_Depth_Land_wav2p1		Retrieved
		X,Y,1: 2.11 µm	Primary
	Optical_Depth_Ratio_Small_Land		Retrieved
		X,Y: (for 0.55 µm)	Primary

	Surface_Reflectance_Land		Retrieved
		X,Y,3: 0.47, 0.65, 2.11 μm	Primary
ε^{avg}	Fitting_Error_Land		Retrieved By-
		X,Y: (at 0.65 μm)	Product
	Quality_Assurance_Land	X,Y,5: 5 bytes	Diagnostic
	Aerosol_Type_Land	X,Y:	Diagnostic
	Mass_Concentration_Land	X,Y:	Derived
ρ_λ^{obs}	Mean_Reflectance_Land	X,Y,10: 0.47,0.55,0.65,0.86,1.2,1.6,2.11, 0.41, 0.44, 0.76 μm*	Diagnostic
	STD_Reflectance_Land	X,Y,10: 0.47,0.55,0.65,0.86,1.2,1.6,2.11, 0.41, 0.44, 0.76 μm*	Diagnostic
	Aerosol_Cloud_Fraction_Land	X,Y:	Diagnostic
	Number_Pixels_Used_Land	X,Y,10: 0.47,0.55,0.65,0.86,1.2,1.6,2.11, 0.41, 0.44, 0.76 μm*	Diagnostic
	Topographic_Altitude_Land	X,Y	DiagnosticImage
$\tau_{0.55}^{avg}$	Image_Optical_Depth_Land_And_Ocean	X,Y: 0.55 μm	Joint (QAC ≥ 0)
$\tau_{0.55}^{avg}$	Optical_Depth_Land_And_Ocean	X,Y: 0.55 μm	Joint (QAC = 3)

X = 135; Y = 203. If there is a 3rd dimension of the SDS, then the indices of it are given. The "Retrieved" parameters are the solution to the inversion, whereas "Derived" parameters are computed from the choice of solution. "Diagnostic" parameters are derived during the retrieval process. "Experimental" products are unrelated to the inversion but may have future applications. "Joint" products are the combined land and ocean products, with associated QAC constraint (for over land) in parentheses. *Note that DT package products does not provide reflectance_land related parameters in wavelengths 0.41, 0.44, and 0.76 μm

TABLE 7-4: SIDE BY SIDE COMPARISON OF THE DATASETS IN EACH DARK TARGET PRODUCT (MODIS AQUA AND TERRA) AND VIIRS/ABI/AHI FOR LAND

MODIS	VIIRS/ABI/AHI
Aerosol_Type_Land	Aerosol_Type_Land
Fitting_Error_Land	Fitting_Error_Land
Surface_Reflectance_Land	Surface_Reflectance_Land
Corrected_Optical_Depth_Land	Corrected_Optical_Depth_Land
Corrected_Optical_Depth_Land_wav2p1	
Optical_Depth_Ratio_Small_Land	Optical_Depth_Ratio_Small_Land
Number_Pixels_Used_Land	Number_Pixels_Used_Land*
Mean_Reflectance_Land	Mean_Reflectance_Land*
STD_Reflectance_Land	STD_Reflectance_Land*
Mass_Concentration_Land	Mass_Concentration_Land
Aerosol_Cloud_Fraction_Land	Aerosol_Cloud_Fraction_Land
Quality_Assurance_Land	
Solution_Index_Ocean_Small	
Solution_Index_Ocean_Large	
Topographic_Altitude_Land	Topographic_Altitude_Land
	Error_Flag_Land_And_Ocean

*Note that DT package products does not provide reflectance_land related parameters in wavelengths 0.41, 0.44, and 0.76 μm

8. The Special MODIS 3 km Aerosol Product

Unlike the other sensors, the MODIS products are provided at two spatial resolutions, the standard 10 km product derived from 20 × 20 pixels, and the 3 km product derived from 6 × 6 pixels. The 3 km product provides the community with a finer resolution aerosol product, which is helpful for specific applications such as air quality monitoring. No finer resolution product has been developed for the other sensors. The 3 km algorithm and preliminary validation is described in Remer et al. [*2013*]. A more complete analysis and validation is provided in Gupta et al. [*2018*].

8.1.   Algorithmic Adaptations for the 3 Km Product

While the land and ocean algorithms are fundamentally different from each other, the algorithms that produce the MODIS 3 km product are not logically different from those that produce the 10 km product. However, small practical changes had to be made to the land and ocean algorithms to optimize their use for retrieving at a higher spatial resolution. The only differences between the 3 km algorithm and the 10 km algorithm are the way the pixels are organized, and the number of pixels required to proceed with a retrieval after all masking and deselection are accomplished.

For the 10 km (nominal at nadir) retrieval, we organize the entire MODIS granule into groups of 20×20 pixels, which we refer to as "retrieval boxes". The left side of Figure 8-1 illustrates a 10 km retrieval box outlined in magenta. The right side of Figure 8-1 shows a 3 km retrieval box, outlined in red.
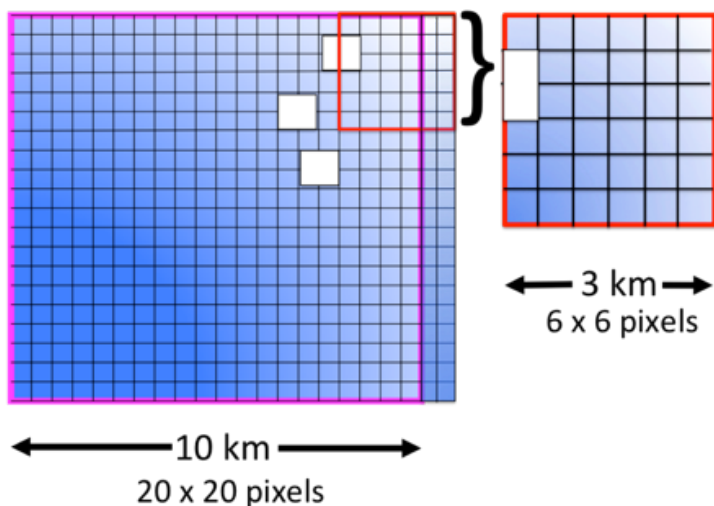

Figure 8-1: Illustration of the organization of the MODIS pixels into retrieval boxes for (left) the 10 km product consisting of 20×20 0.5 km pixels within the magenta square and (right) the 3 km product consisting of 6×6 0.5 km pixels within the red square. The small blue squares represent the 0.5 km pixels. The white rectangles represent pixels identified as cloudy. The 3 km retrieval box is independent of the 10 km box, and is not a subset. Here it is shown enlarged.

Figure 8-2 shows a flow chart showing the separate paths for the 10 km and 3 km retrievals. The black boxes running along the center of chart identify processes that are identical in both retrievals. The inputs are identical, as are the masking procedures. The exact same 0.5 km pixels identified as cloud, sediment etc. in the 10 km algorithm are identified as cloud, sediment etc. in the 3 km algorithm. The difference is in how the two algorithms make use of these 0.5 km designations. Once the 3 km algorithm has identified the pixels suitable for retrieval and decided that a sufficient number of these pixels remain, the spectral reflectances are averaged and the inversion continues exactly the same as in the 10 km algorithm. The same assumptions are used, the same look up tables, the same numerical inversion and the same criteria to determine a good fit.
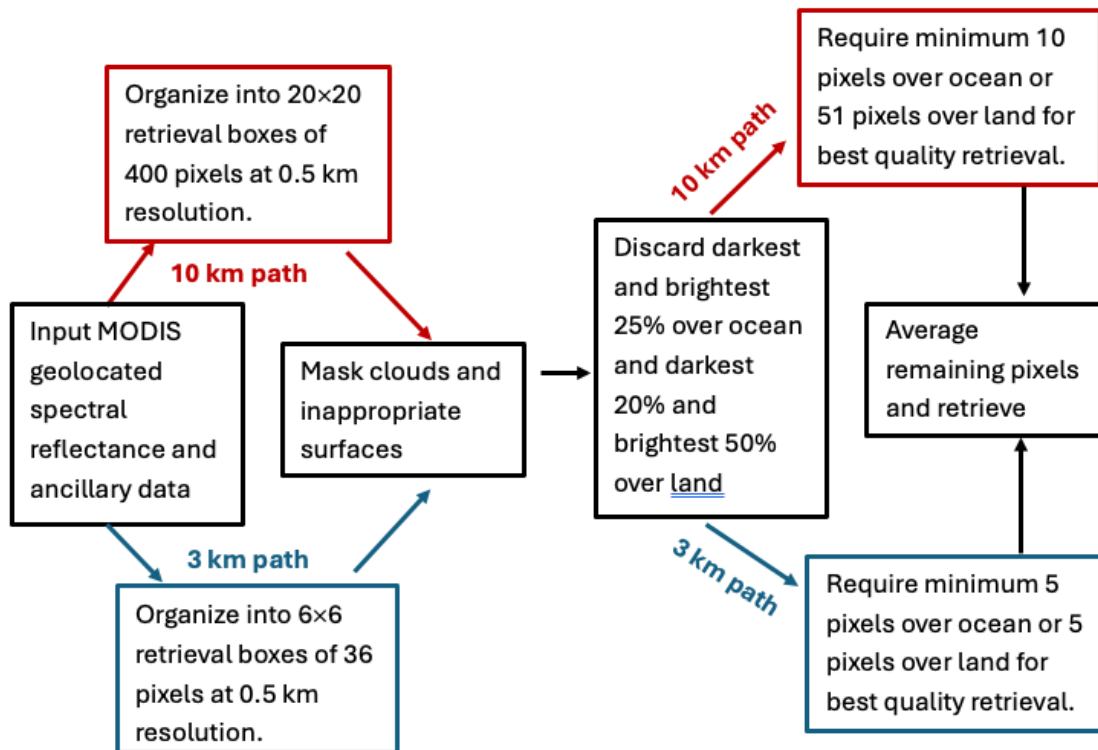
Figure 8-2: Flowchart illustrating the different paths of the 10 km (red) and 3 km (blue) retrievals. The procedures appearing in the black outlined boxes are common to both algorithms.

In the 3 km retrieval the 0.5 km pixels are arranged in retrieval boxes of 6x6 arrays of 36 pixels. Note that in the 3 km retrieval box, the exact same pixels identified as cloudy in the 10 km retrieval box (denoted by the white rectangles) are identified as cloudy in the 3 km box. This is because both algorithms apply identical criteria to mask undesirable pixels. The 3 km retrieval applies a similar deselection of pixels at the darkest and brightest ends of the distribution: 25% and 25% over ocean, and 20% and 50% over land. Once these darkest and brightest pixels are discarded, the algorithm averages the remaining pixels to represent conditions in the 3 km retrieval box. The algorithm requires a minimum of 5 pixels at NIR channel over ocean with at least 12 pixels distributed over the other five channels and 5 pixels are required over land in order to continue and make a retrieval. This is actually a more stringent requirement for ocean (14% of 36), than what is required by the 10 km retrieval (2.5%) for the best quality retrieval. The requirement over land is about the same in the 3 km retrieval as it is in the 10 km retrieval (14% and 13%, respectively).

8.2.   Granules Comparing MODIS 10 km and 3 km Aerosol Products

In this section, we show examples from 15 July 2008 and from 12 January 2010 that illustrate the new 3 km product and how it differs from the 10 km product applied to exactly the same input data.
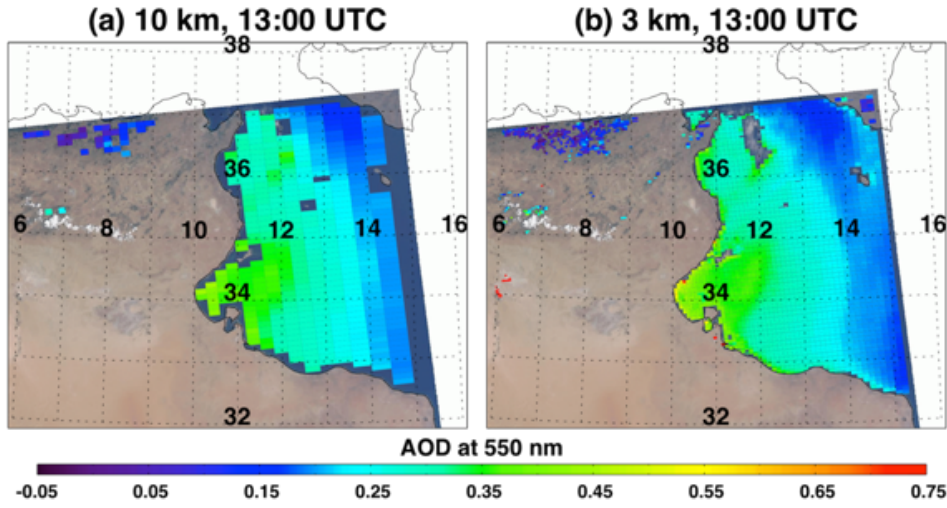
Figure 8-3: Aerosol optical depth at 550 nm retrieved from the 15 July 2010 Aqua-MODIS radiances using the Collection 6 MODIS Dark Target aerosol algorithm. Left: the product at 10 km resolution. Right: the product at 3 km resolution. This is a moderate dust event over the MediTerranean Sea off the costs of Tunisia and Libya. The 3 km retrieval produces values closer to the coastline and to the islands. From Remer et al. [*2013*]

Figure 8-3 compares the 10 km and 3km ocean retrievals over the Mediterranean Sea off the coast of Tunisia and Libya during a moderate dust event. The two resolution products produce almost the exact same aerosol field with the same gradient and same magnitude aerosol optical depth. This is because the two algorithms are essentially the same. The only difference is that the finer resolution product is able to make retrievals closer to the small islands in the image. We find that this is typical of the 3 km product. It offers over-ocean retrievals closer to land, nearer to islands and within narrow waterways and estuaries.
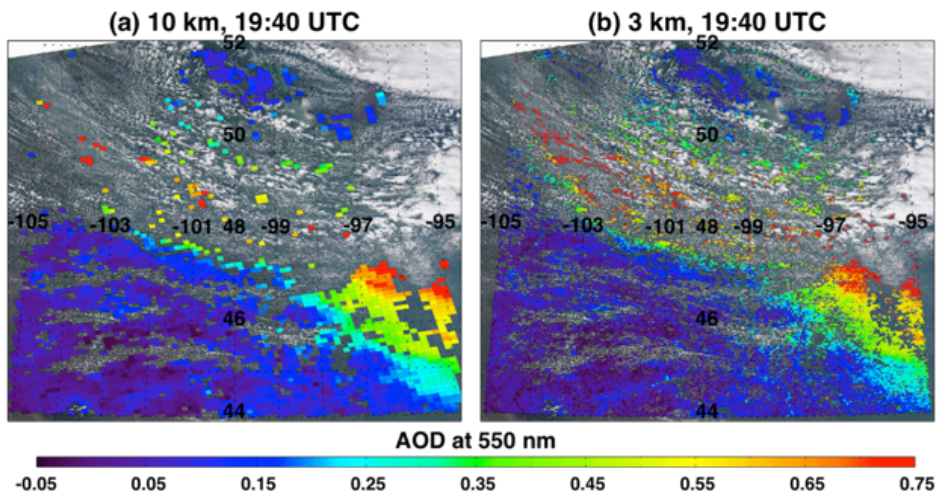
Figure 8-4: 10 and 3 km AOD retrievals for a scene over Canada where the 3 km product better resolves the plume from active wildfires. Note the additional red pixels between the clouds in the upper left corner of the image for the 3 km panel. From Remer et al. [*2013*].

Figure 8-4 illustrates the apparent advantage of the 3 km product to resolve smoke plumes from fires. The fire is a large wild fire burning in Canada. The 10 km product does not capture the long

narrow smoke plume leading towards the northwest, but the 3 km product does. One of the major advantages of the 3 km product is its ability to better resolve smoke plumes than the 10 km product. Even so, because of overzealous masking procedures even the 3 km product will miss the thickest part of the plume [*Shi et al., 2023*].
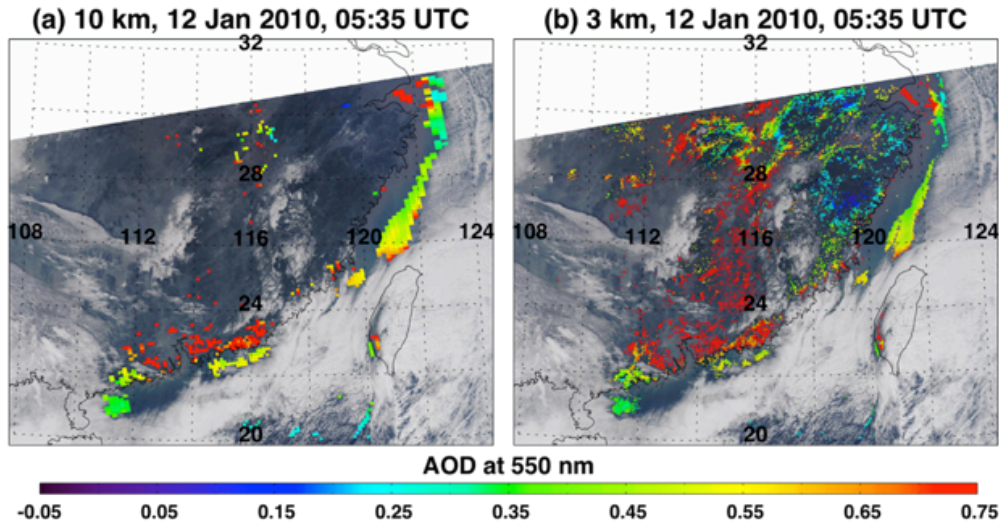
Figure 8-5: 10 and 3 km AOD retrievals for a scene from12 January 2010 during a pollution episode in China. Here the 3 km algorithm is able to make retrievals over a much broader region. The AOD interpolated to 0.55 µm from the only AERONET station in the image (Hong Kong PolyU) is 0.38. The 3 km retrieval there is 0.45, while there is no 10 km retrieval available at that spot during this overpass. From Remer et al, [*2013*].

Figure 8-5 demonstrates the potential for different sampling by the two products. The scene is a highly polluted episode over much of southeastern China. Here the 3km algorithm makes retrievals over a broad area, while the 10 km algorithm finds few opportunities to retrieve. The few places of overlap result in similar values of aerosol optical depth. The only AERONET station in the image is at Hong Kong PolyU (22 18 N, 114 11 E), which reports a collocated AOD interpolated to 0.55 µm at MODIS over- pass time of 0.38. The 10 km algorithm does not produce a retrieval at this station, but the 3 km algorithm does, producing an AOD of 0.45, a reasonable match.

Figure 8-6: 10 and 3 km AOD retrieval comparison over California where the 3 km product introduces widespread

Figure 8-6 illustrates a potential drawback to using the 3 km product. In this retrieval over the highly urbanized surface of Los Angeles and environs, the surface is incompatible with th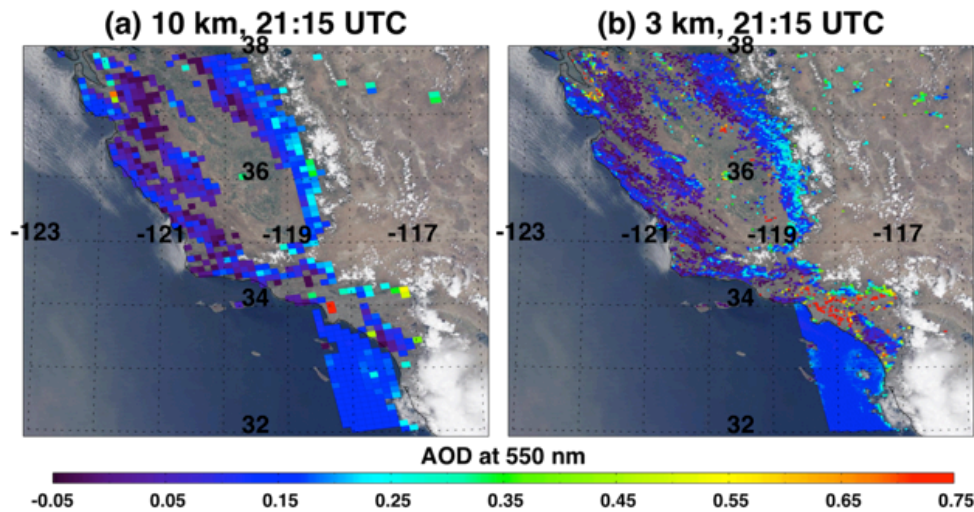e current version of the Dark Target retrieval. The pixel selection process of the 10 km algorithm is able to recognize this incompatibility and makes only two retrievals over Los Angeles. However, the 3 km product does retrieve all through the area, and the result is a scattering of retrieved AOD > 0.8 over the region. Although there is no ground truth to determine whether these points are accurate high AOD situations or noisy artifacts of the retrieval, it is highly likely that they are artifacts that the 3 km retrieval fails to avoid. Although the results of the 3 km product mirror the 10 km retrievals, we do find an increase of noisy artifacts in the finer resolution product. This occurs most frequently over urban surfaces, a type of location of significant interest to the air quality community.

9. File Format and Content

9.1.　　　MODIS C6 MxD04 File Format

The MODIS Level 2 aerosol product files (MOD04_L2 for Terra and MYD04_L2 for Aqua for the 10 km product, MOD04_3K for Terra and MYD04_3K for Aqua for the 3 km product, known commonly as MxD04) are stored in Hierarchical Data Format (HDF). HDF is a multi-object file format for sharing scientific data in multi-platform distributed environments. HDF files can be accessed through HDF library subroutine and function calls, which can be downloaded from the HDF web site (see this link). Proprietary software, such IDL (see this link) and MATLAB (see this link) have built in routines to process IDL files. Also, free tools, including HDFLook (see this link) and Panoply (see this link) are available.

All C61 MxD04 data files (and corresponding L1B and geolocation data files used to create them) are available on-line (at no charge) through the user-friendly Level 1 and Atmosphere Archive and Distribution System (LAADS). MxD04 HDF file names have this naming convention:

MxD04_RR.AYYYYDDD.HHMM.CCC.YEARDAYHRMNSC.hdf

where x is O or Y for Terra or Aqua, RR describes the resolution of the product (L2 for 10 km, 3K for 3 km), YYYY, DDD and HHMM are four digit year, three digit Julian day, and time of day in UTC, CCC is the collection (061 for C61), and YEARDAYHRMNSC represents when the file was processed.

The MxD04_L2 files include many parameters, each stored as a Scientific Data Set (SDS) within the HDF file. Only a subset of these parameters are available in the 3 km files. In addition to the SDSs listed in previous sections of this document (in All products of DT-O are reported in output Level 2 files as Scientific Data Sets (SDSs), and the MODIS C6.1 SDSs are listed in **Error! Not a valid bookmark self-reference.**. These include the *primary retrieved* products, *derived* products, and *diagnostic* products. Where possible, the Table connects symbols from the text above, to the SDS names and their dimensions. For MODIS C6.1, many SDSs have both 'best' and 'avg' values, sometimes noted as separate SDSs (e.g., τ_λ^{best} = 'Effective_Optical_Depth_Best_Ocean' and τ_λ^{avg} = 'Effective_Optical_Depth_Average_Ocean'), and sometimes noted as one SDS having two dimensions ($\eta_{0.55}^{best}, \eta_{0.55}^{avg}$ = 'Optical_Depth_Ratio_Small_Ocean_0.55micron'). A few SDSs only refer to 'best' solutions, including the choice of which fine and coarse modes ('Solution_Index_Small' and 'Solution_Index_Large'), and the 'Optical_Depth_by_Models' $\tau_{0.55}^{best,j}$ which refers to the values of fine

and coarse mode AODs, $\tau_{0.55}^{best,f}$ and $\tau_{0.55}^{best,c}$, but with two values of j filled with values, j1 = Solution_Index_Small, and j2 = Solution_Index_Large.

In addition to the retrieved and derived parameters, DT-O also provides a number of diagnostic products. The most important is the 'Quality_Assurance_Ocean' (QA), which is a qualitative estimate of the overall retrieval's quality and confidence. Details about QA are given in the Appendix 2. Other parameters related to the direct retrieval include the vector of TOA reflectance ρ_λ^{obs} and its standard deviation, which is denoted as 'Mean_Reflectance_Ocean' and 'STD_Reflectance_Ocean'. Finally, there are a number of SDSs related to the suitability of the retrieval box in the first place, including the number of L1B pixels used ('Number_Pixels_Used_Ocean') the estimated cloud fraction ('Aerosol_Cloud_Fraction_Ocean'). More details about these are given in Section 10.

Table 6-7 lists the side-by-side comparison of DT ocean products for MODIS C6.1 versus products for VIIRS/ABI/AHI. Note that due to long-term confusion, nearly all SDSs related to the 'best' are removed for the continuity products. Only the SDS named Optical_Depth_By_Models remains to describe the result of the 'best' solution.

Some of the ocean products are combined with products from land (discussed in the next section) as the *Joint* products. For τ, two joint products are reported, the 'Optical_Depth_Land_And_Ocean' and the 'Image_Optical_Depth_Land_And_Ocean'. The first product is constrained by QAC whereas the "Image" product includes all QAC values in order to provide the most complete visualization of the AOD.

Table 6-6 for ocean and **Table 7-3** for land), the HDF file includes SDSs for location (Latitude, Longitude), geometry (Solar and Sensor zenith and azimuth angles). Additional to DT retrieved parameters, there are SDS involves retrieved $\tau_{0.55}$ from another aerosol algorithm Deep Blue algorithm for MODIS sensors only. SDS regarding merged DT and Deep Blue retrieved parameters are explained in Appendix 5. The full SDS list can be found on the MODIS-atmosphere web site, and may be updated as needed.

The MxD04_L2 product contains data that has a spatial resolution (pixel size) of 10×10 kilometers (at nadir), with larger size closer to swath edges. Each MxD04 product file represents a five-minute time interval of L1B observations (a granule).

9.2. MEaSUREs XAERDT Data Files

As with all Atmosphere discipline products, LAADS groups datasets by "Archive Sets", and the Version 1 XAERDT_L2 files can be found under AS-5019. In general, filenames look like:

XAERDT_L2_SENSOR_PLATFORM.AYYYYDDD.HHMM.001.YearDayHrMnSc.nc

where:

- SENSOR_PLATFORM = ABI_G16, ABI_G17, AHI_H08, AHI_H09, MODIS_Aqua, MODIS_Terra, VIIRS_SNPP or VIIRS_NOAA20
- YYYY, DDD and HHMM are the four-digit year, three-digit Julian day, and time of day (hours and minutes in UTC) of the observation
- CCC is the collection/version (001),
- YearDayHrMnSc is year, Julian day, hour, minute and second when the file was processed.
- .nc = NetCDF format.

As noted above, MODIS granules correspond to 5 minute segments and VIIRS granules are 6 minute segments. Geolocation information is contained within the product files so there are no separate data and metadata files as are found in some satellite products. The Terra, Aqua, S-NPP and NOAA20 satellites have a 16-day orbital cycle. Granules from an individual sensor with the same time designation which are 16 days apart should be observing the same geographic location with the same

geometry unless an orbital maneuver has been performed in the intervening time period. All AHI have a 10-minute cadence, except there are never files at 02:20 or 14:20 daily due to orbital manuevers. ABI on both GOES-16 and GOES-17 began 2019 with 15-minute observation cadence, but switched to 10 minute cadence to match with AHI starting at 16:00 UTC on April 2, 2019 (DDD = 093). There may be missing files due to any number of reasons.

TABLE 9-1: PROPERTIES OF SENSORS USED AND DT PRODUCTS ARCHIVED AS XAERDT_L2

Sensor	LEO (Granule)		GEO (Full Disk)	
	MODIS	VIIRS	ABI	AHI-H08/H09
Dates processed	2019-2022	2019-2022	2019-2022	H08: 2019 - 13 Dec 2022 H09: 14 - 31 Dec 2022
Platform Eq crossing Time for LEO or Longitude for GEO	Terra: 10:30 (descend) Aqua: 13:30 (ascend)	SNPP: 13:30 (ascend) NOAA20: 13:30 (ascend)	G16 (East): 75.0°W G17 (West): 137.0°W	H08: 140.7°E H09: 140.7°E
Altitude (km)	705	820	36K	36K
Orbits/day	14.5	14	N/A	N/A
# obs of Ground target at equator	<1/ day	1/day	144/day	144/day
Swath width (km)	2330	3040	Full Disk	Full Disk
Field of view	±55°	±56°	±8°	±8°
Number of Wavebands	36	22	16	16
Blue / Red band pixel size at nadir (km)	0.5 / 0.25	0.75 / 0.375	1.0 / 0.5	1.0 / 0.5
Granule or FD X × Y size in pixels	2708 × 4080	3200 × 3232	10848 × 10848	11000 × 11000
Granule or FD time length (mins)	5	6	10	10
Scan lines per scan	20	8	1000	1000
BowTie?	Yes	Corrected	No	No
N×N aggregation (of blue band)	20×20	8×8	10×10	10×10
XAERDT_L2 resolution at nadir (km)	10	6	10	10
XAERDT_L2 Product X × Y size	135 × 204	400 x 404	1084 x 1084	1100 x 1100

Product file dimensions are a function of the granule size, swath width, pixel size and viewing geometry. XAERDT_L2 products' approximate spatial dimensions of retrieval boxes (km at nadir) and retrieval box/file pixel size (X × Y) are given in **Table 9-1**. For MODIS and VIIRS granules, "Y" means "Along swath" which refers to the path of the satellite and "X" means "across swath" which is perpendicular to this direction. While MODIS is 10 km × 10 km near nadir, its pixels expand in the across swath direction. The further from nadir the greater the expansion due to the sensor's viewing angle coupled with the curvature of the Earth. At the edge of the swath the product may be closer to 40 km × 20 km. For VIIRS, the product is about 6 km × 6 km at nadir, but due to updates in reduced in VIIRS sensor design and data handling choices, product dimensions at the edge only approximately double. For ABI and AHI, the FD includes the limb, as well as imagery "off" the edge of the Earth! The DT product keeps only when view angles are less than 72°. Nonetheless compared to pixels at 10 km subsatellite, the edge pixels with viewing zenith angle of 72° grow to ~25 km.

The file structure between products from XAERDT_L2 and MODIS C61 is different due to several reasons, including file format changed from HDF to NetCDF and VIIRS Deep Blue is its own product (AERDB_L2_VIIRS_SNPP and related NRT and L3 products) there are no Deep Blue or merged DT/DB datasets in the VIIRS DT file. The remaining differences between the datasets in the level 2 products are shown side by side in **Table 9-2**.

TABLE 9-2. SIDE BY SIDE COMPARISON OF THE DATASETS IN EACH DARK TARGET PRODUCT (DEEP BLUE AND MERGED DT/DB DATASETS FOR MODIS OMITTED).

MODIS C6.1	Other
variables:	group: geolocation_data

Longitude	longitude
Latitude	latitude
Scan_Start_Time	
Solar_Zenith	solar_zenith_angle
Solar_Azimuth	solar_azimuth_angle
Sensor_Zenith	sensor_zenith_angle
Sensor_Azimuth	sensor_azimuth_angle
Scattering_Angle	Scattering_Angle
	Glint_Angle
	group: geophysical_data
Land_sea_Flag	Land_Sea_Flag
Aerosol_Cldmask_Land_Ocean	Aerosol_Cldmask_Land_Ocean
Cloud_Pixel_Distance_Land_Ocean	Cloud_Pixel_Distance_Land_Ocean
Land_Ocean_Quality_Flag	Land_Ocean_Quality_Flag
Optical_Depth_Land_And_Ocean	Optical_Depth_Land_And_Ocean
Image_Optical_Depth_Land_And_Ocean	Image_Optical_Depth_Land_And_Ocean
Average_Cloud_Pixel_Distance_Land_Ocean	Average_Cloud_Pixel_Distance_Land_Ocean
Aerosol_Type_Land	Aerosol_Type_Land
Fitting_Error_Land	Fitting_Error_Land
Surface_Reflectance_Land	Surface_Reflectance_Land
Corrected_Optical_Depth_Land	Corrected_Optical_Depth_Land
Corrected_Optical_Depth_Land_wav2p1	
Optical_Depth_Ratio_Small_Land	Optical_Depth_Ratio_Small_Land
Number_Pixels_Used_Land	Number_Pixels_Used_Land
Mean_Reflectance_Land	Mean_Reflectance_Land
STD_Reflectance_Land	STD_Reflectance_Land
Mass_Concentration_Land	Mass_Concentration_Land
Aerosol_Cloud_Fraction_Land	Aerosol_Cloud_Fraction_Land
Quality_Assurance_Land	
Solution_Index_Ocean_Small	
Solution_Index_Ocean_Large	
Effective_Optical_Depth_Best_Ocean	
Effective_Optical_Depth_Average_Ocean	Effective_Optical_Depth_Average_Ocean
Optical_Depth_Small_Best_Ocean	
Optical_Depth_Small_Average_Ocean	Optical_Depth_Small_Average_Ocean
Optical_Depth_Large_Best_Ocean	
Optical_Depth_Large_Average_Ocean	Optical_Depth_Large_Average_Ocean
Mass_Concentration_Ocean	Mass_Concentration_Ocean
Aerosol_Cloud_Fraction_Ocean	Aerosol_Cloud_Fraction_Ocean
Effective_Radius_Ocean	Effective_Radius_Ocean
PSML003_Ocean	PSML003_Ocean
Asymmetry_Factor_Best_Ocean	

Asymmetry_Factor_Average_Ocean	Asymmetry_Factor_Average_Ocean
Backscattering_Ratio_Best_Ocean	
Backscattering_Ratio_Average_Ocean	Backscattering_Ratio_Average_Ocean
Angstrom_Exponent_1_Ocean	Angstrom_Exponent_1_Ocean
Angstrom_Exponent_2_Ocean	Angstrom_Exponent_2_Ocean
Least_Squares_Error_Ocean	Least_Squares_Error_Ocean
Optical_Depth_Ratio_Small_Ocean_0.55micron	Optical_Depth_Ratio_Small_Ocean_0p55micron
Optical_Depth_by_models_ocean	Optical_Depth_By_Models_Ocean
Number_Pixels_Used_Ocean	Number_Pixels_Used_Ocean
Mean_Reflectance_Ocean	Mean_Reflectance_Ocean
STD_Reflectance_Ocean	STD_Reflectance_Ocean
Quality_Assurance_Ocean	
Glint_Angle	
Wind_Speed_Ncep_Ocean	Wind_Speed_GMAO_Ocean
Topographic_Altitude_Land	Topographic_Altitude_Land
Effective_Optical_Depth_0p55um_Ocean	
	Error_Flag_Land_And_Ocean

9.3.   Recommendations for Use of Data

9.3.1. Total τ

The quantitative DT land and ocean joint τ product (i.e., 'Optical_Depth_Land_And_Ocean') include data of minimum QAC > 1 over ocean and QAC = 3 over land. While we recommend using that SDS for quantitative studies, for some applications it may be more appropriate to only examine the land or ocean separately derived τ SDSs ('Effective_Optical_Depth_Average_Ocean' and 'Corrected_Optical_Depth_Land'). The DT land and ocean joint qualitative SDS 'Image_Optical_Depth_Land_And_Ocean' reports all valid (non-fill value) AOD, over land and ocean, regardless of QAC value. This product can be used to trace aerosol plumes and make aerosol maps but should not be used for quantitative study.

It also should be repeated that over land, the algorithm permits retrieval of small negative τ values in order to avoid arbitrary biases in long-term statistics. Due to not enough sensitivity over land to retrieve aerosol to better than ±0.05, in very clean conditions, the algorithm cannot determine $\tau = 0.00$ from 0.05 or -0.05. It is up to a user to decide what to do with these values, whether to force them to zero or some small positive value (for use within models). However, these retrievals of negative τ are considered to be good retrievals, and are assigned QAC = 3, unless other conditions apply. Over ocean, however, retrievals of negative τ are not permitted, so that they are automatically forced to zero, but still can be considered as high-quality retrievals.

Below list the all total τ related parameters:

Corrected_Optical_Depth_Land – AOD retrieved over Land at 4 wavelengths (Blue, Green=0.55 μm, Red, SWIR2). The term "Corrected" in the SDS name is a legacy from earlier products. There is no "Uncorrected" version of this SDS. Except for the green wavelength always reported at 0.55 μm, other AODs are reported at the sensor's wavelength.

Effective_Optical_Depth_Average_Ocean – AOD retrieved over Ocean at 7 wavelengths. This SDS averages all retrievals within the algorithm's acceptable error limits. AOD at 0.55 is reported for all sensors, however, the other wavelengths represent specific sensor.

Land_Ocean_Quality_Flag – Quality assurance (QA) or Confidence for the Ocean and Land. For each retrieval path Land or Ocean, QA values are subjectively assigned by the algorithm team based on numerical standards such as number of input pixels used for the retrieval, proximity to bright land or ocean glint and error fitting values. QA values range from 0 – 3 where zero is lowest confidence and 3 is highest confidence. (See Appendix 2)

Image_Optical_Depth_Land_And_Ocean - AOD land plus ocean at 0.55 μm, not filtered for QA. This SDS joins the AOD retrievals for land and ocean, with no requirements for QA confidence levels. It is reported only at 0.55 μm, and provides a snapshot with the greatest amount of retrieval coverage, suitable for general overviews of the scene.

Optical_Depth_Land_And_Ocean – AOD land plus ocean reported at 0.55 μm, filtered for QA

This SDS uses QA to "filter" before joining the AOD retrievals for land and ocean. Specifically, it requires QA ≥ 2 for land, and QA ≥ 1 for ocean. We expect this SDS should be the default for most quantitative studies. It is reported only at 0.55 μm.

9.3.2. Other Aerosol SDSs

Other than total τ, there are other aerosol related SDSs including **AOD by models/aerosol types,** the **fine model weighting (FMW)**, and other derived AOD related to FMW. From these retrieved parameters, one can further derive properties of the aerosol, such **Angstrom Exponent (AE)**. These parameters are explained here:

Fine and Coarse Mode: In general, atmospheric aerosols are observed to have multi-modal distributions. Smaller particles are referred to as "fine mode" (also known as accumulation mode), and have effective radii between 0.1 and 0.25 micrometers. Larger particles ("coarse mode"), have effective radii between 1.0 and 2.5 microns. The DT algorithm assumes properties of each size range (fine model and coarse model) and attempts to mix them together when matching the satellite-observed spectral reflectance. Details on the specific assumptions and how the algorithm computes (whether Land or Ocean) are given in the Section 2.2 and Section 6.4 and Section 7.6.

The aerosol fine mode fraction (FMF; also known as Fine Mode Weighting or FMW) is the proportion of fine mode aerosols to the total, and is defined in terms of total AOD. Therefore, it then be multiplied by the total AOD to determine proportional fine and coarse -AOD (coarse = total – fine). The proportional AOD is only reported for the ocean product. We feel that the algorithms' ability to distinguish fine or coarse mode over land is not accurate enough to permit us to make a fine mode AOD calculation, even when the retrieval algorithm is providing FMF.

Optical_Depth_Ratio_Small_Land: FMF over land

Optical_Depth_Ratio_Small_Ocean_0p55micron: FMF over ocean

Optical_Depth_Small_Average_Ocean: AOD * FMF over ocean, reported at 7 bands.

Optical_Depth_Large_Average_Ocean: AOD * (1-FMF) over Ocean, reported at 7 bands.

Optical_Depth_By_Models_Ocean: The Ocean retrieval retrieves its best fit by choosing among combinations of fine (4 choices) and coarse (5 choices) aerosol models. Essentially, Optical_Depth_Small gets assigned to its model choice (index 1 to 4), whereas Optical_Depth_Large gets assigned to its model choice (index 5 – 9).

Aerosol_Type_Land: The Land retrieval retrieves its best fit by assuming aerosol models based on season and location. The values are denoted by 1 = Continental, 2 = Moderate Absorption Fine, 3 = Strong Absorption Fine,4 = Weak Absorption Fine, 5 = Dust Coarse

Ångström Exponent: The Ångström Exponent (AE) relates to spectral dependence of AOD, and is often used as a qualitative indicator of mean particle size. As a rough guideline Ångström Exponent values in the range of 2 indicate small particles which might be associated with pollution or biomass burning. Values in the range of 1 or less indicate the presence of large particles such as sea salt or dust. For the MODIS algorithm Ångström Exponent is not a true measurement but is a derived value. Note, due to signal-to-noise issues, AE is only reported when aerosol loading (total AOD) is moderate or larger (AOD > 0.2). Note that AEs are calculated based on the nominal wavelengths of the sensor, and may not be entirely comparable between sensors.

Angstrom_Exponent_1_Ocean: AE over Ocean, computed by using Effective_Optical_Depth and comparing AOD for 0.55 and NIR (e.g. 0.87 μm) bands; relates to spectral dependence of fine mode.

Angstrom_Exponent_2_Ocean: AE over Ocean, computed by using Effective_Optical_Depth and comparing AOD for NIR (e.g. 0.87 μm) and SWIR3 (e.g. 2.25 μm) bands; relates to spectral dependence of coarse mode

Angstrom_Exponent_Land: AE over Land, computed by using Corrected_Optical_Depth, and comparing AOD for Blue (e.g. 0.49 μm) and Red (e.g. 0.67 μm).

9.3.3. Other Derived and Diagnostic Parameters

There are a number of other parameters reported within the DT aerosol product. Some of these are "derived" or "diagnostic" products; reported because they have been useful for some applications. None of these are validated. More details can be found in the full ATBD.

For example, there is an estimate of **Mass_Concentration** over both **_Land** and **_Ocean**, which represents the total integrated columnar mass per square area. It is not a retrieved parameter, but rather is a function of aerosol models assumed during the retrieval (and assumed density). Other similar SDSs include **Assymetry_Parameter** and **BackScattering_Ratio**.

Other diagnostic parameters include SDSs relating to **Mean_Reflectance**. These are the averaged values of reflectance used for either the **_Land** or **_Ocean** retrievals.

There are SDSs related to the algorithm's estimate of clouds in the retrieval box. This includes the **Aerosol_Cldmask_Land_Ocean**, which is an N × N grid within each retrieval box, of pixels marked "cloud" or "clear", along with an estimate of the **Aerosol_Cloud_Fraction** within the retrieval box. Finally, an interesting diagnostic is the **Cloud_Pixel_Distance_Land_Ocean**, which attempts to indicate the distance (in pixels) between each pixel and the nearest detected "cloud" pixel (Appendix 6).

At this point, the MODIS aerosol team has not evaluated the reliability of other parameters, including certain derived parameters and diagnostic parameters. The user is cautioned that there is no expected quantitative value to these parameters.

10. Procedures of Evaluation and Validation of DT Products

The first step in determining the quality of any product is to ensure that the product outputs make sense in the real world. We evaluate the products visually to see if they look as expected. Do images of a parameter have discontinuities, gaps, or any other features that indicate logical errors or other problems? Are diagnostic parameters useful, and correct? Are the mean values and the histograms of a retrieved or derived parameter reasonable, at different temporal and spatial scales? Many of these tests are subjective, but they are important in identifying problems in the algorithm or the assumptions.

For all applicable cases we attempt to perform a product *validation*. This means that a product is comparable to some "ground-truth" measurement within some measure of *expected uncertainty*. The

primary means of DT products validation is by showing that a product matches equivalent observations from AERONET or other accurate systems (e.g. Marine Aerosol Network (MAN)). To be considered validated, at least 2/3 (or one standard deviation) of global matched pairs (e.g. MODIS versus AERONET green channel AOD) must be contained within the envelope of expected error (EE). For MODIS C61 product the defined EE is $\pm(0.05 + 0.15\tau_{ground\_truth})$ overland and $(+(0.04 + 0.10\tau_{ground_{truth}}), -(0.02 + 0.10\tau_{ground\_truth}))$ overocean. for the higher-resolution (3KM) MODIS products, as well as VIIRS V2 product and the ABI products, the EE envelope is looser. For these products, we see EE about $\pm(0.05 + 0.20\tau_{ground\_truth})$ overland and $\pm(0.05 + 0.15\tau_{ground\_truth})$ overocean.

   Our primary means of validation is comparison with ground-based sunphotometer measurements, specifically, those of AERONET *[Holben, et al. 1998]* . In direct measurement mode, the AERONET instruments measure spectral τ, to within ~0.01 in the visible and near-IR wavelength regions [*Eck et al., 1999*] and can be used to derive Fine Weighting (η) by the spectral deconvolution method of O'Neill et al. [*2003*]. The AERONET measured τ is easily interpolated to the exact satellite wavelengths (for example 0.55 μm) by quadratic interpolation in log reflectance/log τ space. In the following validation, we use AERONET Version 3 Level 2.0 data (cloud screened and quality assured for instrument calibration) *[Smirnov, et al. 2000; Giles et al., 2019]* . Although North America and Europe provide the most stations in the data base (http://aeronet.gsfc.nasa.gov), all continents (except Antarctica), all oceans and all aerosol types are represented. The methodology of comparing temporally varying AERONET data with spatially varying MODIS data is described in *[Ichoku et al., 2002]* , and the updated method we apply here is described in Petrenko et. al. [*2012*]. There are very different sampling of LEO and GEO satellite product, their unique collocation strategy between these satellite products and AERONET data are listed in **Table 10-1**. Remer et al. [*2005*] provide a comprehensive validation of τ from MODIS C4, whereas Kleidman et al., [*2005*] provide comparisons of the η product, Levy et al., [*2010*] provide a global validation of the MODIS C5-Land aerosol products, Levy et al., [*2013*] provide a global validation of the MODIS C6 land and ocean aerosol products, and Pawan et al., [*2018*] provide a global and regional validation of MODIS 3 km product over land. Site by site validation can also be found on DT website at this link.

TABLE 10-1: COLLOCATION CRITERIA BETWEEN DT SATELLITE PRODUCTS AND GROUND-TRUTH DATA

Products	Sensors Satellite	Time window	Radius at nadir	Min # of DT product retrievals	Min # of AERONET retrievals
Individual LEO DT products	MODIS Terra / Aqua 10 km	±30 mins	27.5 km	20% of possible retrievals or 5	2
	VIIRS SNPP				
	MODIS Terra / Aqua 3 km		7.5 km		
Combined LEO and GEO DT products from DT package	MODIS Terra / Aqua 10 km	±15 mins	20.0 km		
	ABI (GOES-16 and GOES-17)				
	VIIRS SNPP / NOAA20				
	AHI Himawari-8				

Suborbital DT products	eMAS on ER-2	±30 mins	6.0 km	5	

For more validation results and uncertainty analysis please refer to published journal articles and Dark Target website (see this link).

11. Summary

In this document, we have described the fundamentals as well as the latest updates of the dark target algorithm used for deriving aerosol properties from observed spectral reflectance from a family of MODIS-like passive image spectrometers. The DT algorithm was originally developed for the MODIS instrument on polar-orbiting satellite Terra and Aqua. Recently the algorithm has been ported to the many similar instruments, including the VIIRS instruments on SNPP, the JPSS series (NOAA-20 etc.), ABI on NOAA's GOES-R series, as well as Airborne instrument such as enhanced MODIS Airborne Simulator (eMAS), which provides low-altitude measurements at much higher spatial resolution. As with previous versions of DT operational algorithm, the core inversion is comprised of two separate algorithms, one for deriving aerosol properties over ocean, the other over land.

For standard version of MODIS products, known as MxD04_L2 (10 km version) and MxD04_3K (3 KM version), the current version of the algorithm and products is known as Collection 6.1. These data are being produced in forward processing (since 2017) and have been reprocessed back to the beginning of mission (2000 for Terra, 2002 for Aqua). Files are produced in HDF format.

The application of DT algorithm to different sensors has prompted the creation of a generic DT-Package that adopts the DT core algorithm components but separate modules to mainly handle different input sensor data, file formats and independent LUTs for each sensor because of slightly different spectral wavelengths. The new DT-package is used as a basis for processing the standard 6 x 6 km products of VIIRS, for which the current implementation is known as Version 2.0 and has been running since mid 2023. Products for Suomi-NPP go back to 2011 whereas products for NOAA-20 go back to 2018. These products are known as AERDT_L2 and are in NetCDF4 format. The DT-Package is also used for the MEaSUREs XAERDT effort (2019-2022), which includes GEO sensors (ABI and AHI), as well as parallel runs for VIIRS (on SNPP) and both MODIS sensors. DT-Package also has been used to process the field campaign measurements from eMAS.

While the XAERDT Version 1 product for VIIRS is nearly identical (except for metadata and archival information) as the standard AERDT Version 2 product, the XAERDT product for MODIS differs from its C6.1 counterpart. One of the main differences between the DT-package and previous operational algorithm is that the DT-Package no longer reads and processes one scan line after another and process the pixels in their native resolution, rather it reads in the entire granule and apply cloud mask before conducting pixel selection and retrieval on each N × N grid boxes. While users will see variables that look and feel much like their MODIS counterparts, the organization of the SDSs within file is simplified, and some redundant or confusing variables have been removed.

While the ATBD for MODIS had been continually updated from at-launch, through Collections 4, 5 and 6, the porting to multiple sensors made that MODIS-specific ATBD obsolete. Rather than write many corrections and updates, we decided to re-wrirte this ATBD from scratch, and make sure equations and tables represented the generic equations as well as the particulars.

The DT-Package provides modularity and flexibility so it can be improved in the future. It is being used as a basis for developing Collection 7 of MODIS and has already been proven to work within the MODAPS environment. Thus, using the DT-Package, we can consistently apply updates to MODIS, VIIRS and GEO retrievals.

12. References

Ahmad, Z. and Fraser, R. S.: An Iterative Radiative Transfer Code For Ocean-Atmosphere Systems., Journal of Atmospheric Sciences, 39, 656–665, https://doi.org/10.1175/1520-0469(1982)039%3C0656:AIRTCF%3E2.0.CO;2, 1982.

Al-Saadi, J., Szykman, J., Pierce, R. B., Kittaka, C., Neil, D., Chu, D. A., Remer, L., Gumley, L., Prins, E., Weinstock, L., MacDonald, C., Wayland, R., Dimmick, F., and Fishman, J.: Improving national air quality forecasts with satellite aerosol observations, B Am Meteorol Soc, 86, 1249–1261, https://doi.org/10.1175/BAMS-86-9-1249, 2005.

Anderson, T. L., Wu, Y., Chu, D. A., Schmid, B., Redemann, J., and Dubovik, O.: Testing the MODIS satellite retrieval of aerosol fine-mode fraction, J. Geophys. Res., 110, 18204, https://doi.org/10.1029/2005JD005978, 2005.

Barnes, W. L., Pagano, T. S., and Salomonson, V. V.: Prelaunch characteristics of the Moderate Resolution Imaging Spectroradiometer (MODIS) on EOS-AM1, IEEE Trans. Geosci. Remote Sensing, 36, 1088–1100, https://doi.org/10.1109/36.700993, 1998.

Bodhaine, B. A., Wood, N. B., Dutton, E. G., and Slusser, J. R.: On Rayleigh Optical Depth Calculations, J. Atmos. Oceanic Technol., 16, 1854–1861, https://doi.org/10.1175/1520-0426(1999)016<1854:ORODC>2.0.CO;2, 1999.

Bruegge, C. J., Arnold, G. T., Czapla-Myers, J., Dominguez, R., Helmlinger, M. C., Thompson, D. R., Bosch, J. V. D., and Wenny, B. N.: Vicarious Calibration of eMAS, AirMSPI, and AVIRIS Sensors During FIREX-AQ, IEEE Trans. Geosci. Remote Sensing, 59, 10286–10297, https://doi.org/10.1109/TGRS.2021.3066997, 2021.

Carroll, M. L., DiMiceli, C. M., Townshend, J. R. G., Sohlberg, R. A., Elders, A. I., Devadiga, S., Sayer, A. M., and Levy, R. C.: Development of an operational land water mask for MODIS Collection 6, and influence on downstream data products, International Journal of Digital Earth, 10, 207–218, https://doi.org/10.1080/17538947.2016.1232756, 2017.

Chin, M., Ginoux, P., Kinne, S., Torres, O., Holben, B. N., Duncan, B. N., Martin, R. V., Logan, J. A., Higurashi, A., and Nakajima, T.: Tropospheric Aerosol Optical Thickness from the GOCART Model and Comparisons with Satellite and Sun Photometer Measurements, http://dx.doi.org/10.1175/1520-0469(2002)059<0461:TAOTFT>2.0.CO;2, 59, 461–483, 2002.

Chu, D. A., Kaufman, Y. J., Ichoku, C., Remer, L. A., Tanré, D., and Holben, B. N.: Validation of MODIS aerosol optical depth retrieval over land, Geophysical Research Letters, 29, https://doi.org/10.1029/2001GL013205, 2002.

Chu, D. A., Kaufman, Y. J., Zibordi, G., Chern, J. D., Mao, J., Li, C., and Holben, B. N.: Global monitoring of air pollution over land from the Earth Observing System-Terra Moderate Resolution Imaging Spectroradiometer (MODIS), J. Geophys. Res., 108, 4661, https://doi.org/10.1029/2002JD003179, 2003.

Chu, D. A., Remer, L. A., Kaufman, Y. J., Schmid, B., Redemann, J., Knobelspiesse, K., Chern, J. D., Livingston, J., Russell, P. B., Xiong, X., and Ridgway, W.: Evaluation of aerosol properties over ocean from Moderate Resolution Imaging Spectroradiometer (MODIS) during ACE-Asia, J. Geophys. Res., 110, 07308, https://doi.org/10.1029/2004JD005208, 2005.

Chylek, P., Henderson, B., and Mishchenko, M.: Satellite based retrieval of aerosol optical thickness: The effect of sun and satellite geometry, Geophysical Research Letters, 30, 2003GL016917, https://doi.org/10.1029/2003GL016917, 2003.

Ciren, P. and Kondragunta, S.: Dust aerosol index (DAI) algorithm for MODIS, JGR Atmospheres, 119, 4770–4792, https://doi.org/10.1002/2013JD020855, 2014.

Cox, C. and Munk, W.: Measurement of the Roughness of the Sea Surface from Photographs of the Sun's Glitter, Journal of the Optical Society of America, 44, 838–850, https://doi.org/10.1364/JOSA.44.000838, 1954.

Dave, J. V.: Intensity and Polarization of the Radiation Emerging from a Plane-Parallel Atmosphere Containing Monodispersed Aerosols, Appl. Opt., 9, 2673, https://doi.org/10.1364/AO.9.002673, 1970.

Dim, J. R., Takamura, T., Higurashi, A., Kathri, P., Kikuchi, N., and Nakajima, T. Y.: Validation of Two MODIS Aerosols Algorithms with SKYNET and Prospects for Future Climate Satellites Such as the GCOM-C/SGLI, Advances in Meteorology, 2013, 1–16, https://doi.org/10.5194/acp-10-10399-2010, 2013.

van Donkelaar, A., Martin, R. V., Levy, R. C., da Silva, A. M., Krzyzanowski, M., Chubarova, N. E., Semutnikova, E., and Cohen, A. J.: Satellite-based estimates of ground-level fine particulate matter during extreme events: A case study of the Moscow fires in 2010, Atmospheric Environment, 45, 6225–6232, https://doi.org/10.1016/j.atmosenv.2011.07.068, 2011.

Dubovik, O. and King, M. D.: A flexible inversion algorithm for retrieval of aerosol optical properties from Sun and sky radiance measurements, J. Geophys. Res., 105, 20673–20696, https://doi.org/10.1029/2000JD900282, 2000.

Dubovik, O., Holben, B., Lapyonok, T., Sinyuk, A., Mishchenko, M., Yang, P., and Slutsker, I.: Non-spherical aerosol retrieval method employing light scattering by spheroids, Geophys Res Lett, 29, preprint no.-1415, https://doi.org/10.1029/2001GL014506, 2002a.

Dubovik, O., Holben, B., Eck, T. F., Smirnov, A., Kaufman, Y. J., King, M. D., Tanré, D., and Slutsker, I.: Variability of Absorption and Optical Properties of Key Aerosol Types Observed in Worldwide Locations, J. Atmos. Sci., 59, 590–608, https://doi.org/10.1175/1520-0469(2002)059<0590:VOAAOP>2.0.CO;2, 2002b.

Eck, T., Holben, B., Dubovik, O., Smirnov, A., Goloub, P., Chen, H., Chatenet, B., Gomes, L., Zhang, X., Tsay, S., Ji, Q., Giles, D., and Slutsker, I.: Columnar aerosol optical properties at AERONET sites in central eastern Asia and aerosol transport to the tropical mid-Pacific, J. Geophys. Res., 110, D06202, https://doi.org/10.1029/2004JD005274, 2005.

Eck, T. F., Holben, B. N., Reid, J. S., Dubovik, O., Smirnov, A., O'Neill, N. T., Slutsker, I., and Kinne, S.: Wavelength dependence of the optical depth of biomass burning, urban, and desert dust aerosols, J. Geophys. Res., 104, 31333–31349, https://doi.org/10.1029/1999JD900923, 1999.

Evans, K. F. and Stephens, G. L.: A new polarized atmospheric radiative transfer model, Journal of Quantitative Spectroscopy and Radiative Transfer, 46, 413–423, https://doi.org/10.1016/0022-4073(91)90043-P, 1991.

Franz, B. A., Bailey, S. W., Werdell, P. J., and McClain, C. R.: Sensor-independent approach to the vicarious calibration of satellite ocean color radiometry, Appl. Opt., 46, 5068, https://doi.org/10.1364/AO.46.005068, 2007.

Fraser, R. S., Ferrare, R. A., Kaufman, Y. J., MARKHAM, B. L., and Mattoo, S.: Algorithm for atmospheric corrections of aircraft and satellite imagery, Int J Remote Sens, 13, 541–557, https://doi.org/10.1080/01431169208904056, 1992.

Gao, B.-C., Kaufman, Y. J., Tanré, D., and Li, R.-R.: Distinguishing tropospheric aerosols from thin cirrus clouds for improved aerosol retrievals using the ratio of 1.38-μm and 1.24-μm channels, Geophys Res Lett, 29, 36–1, https://doi.org/10.1029/2002GL015475, 2002.

Gao, Y., Kaufman, Y. J., Tanré, D., Kolber, D., and Falkowski, P. G.: Seasonal distributions of aeolian iron fluxes to the global ocean, Geophysical Research Letters, 28, 29–32, https://doi.org/10.1029/2000GL011926, 2001.

Gatebe, C., King, M., Tsay, S., Ji, Q., Arnold, G., and Li, J.: Sensitivity of off-nadir zenith angles to correlation between visible and near-infrared reflectance for use in remote sensing of aerosol over land, Ieee T Geosci Remote, 39, 805–819, 2001.

Gupta, P., Levy, R. C., Mattoo, S., Remer, L. A., and Munchak, L. A.: A surface reflectance scheme for retrieving aerosol optical depth over urban surfaces in MODIS Dark Target retrieval algorithm, Atmos Meas Tech, 9, 3293–3308, https://doi.org/10.5194/amt-9-3293-2016, 2016.

Gupta, P., Remer, L. A., Levy, R. C., and Mattoo, S.: Validation of MODIS 3 km land aerosol optical depth from NASA's EOS Terra and Aqua missions, Atmos Meas Tech, 11, 3145–3159, https://doi.org/10.5194/amt-11-3145-2018, 2018.

Gupta, P., Levy, R. C., Mattoo, S., Remer, L. A., Holz, R. E., and Heidinger, A. K.: Applying the Dark Target aerosol algorithm with Advanced Himawari Imager observations during the KORUS-AQ field campaign, Atmos Meas Tech, 12, 6557–6577, https://doi.org/10.5194/amt-12-6557-2019, 2019.

Holben, B. N., Eck, T. F., Slutsker, I., Tanre, D., Buis, J. P., Setzer, A., Vermote, E., Reagan, J. A., Kaufman, Y. J., Nakajima, T., Lavenu, F., Jankowiak, I., and Smirnov, A.: AERONET - A federated instrument network and data archive for aerosol characterization, Remote Sens Environ, 66, 1–16, https://doi.org/10.1016/S0034-4257(98)00031-5, 1998.

Holben, B. N., Tanre, D., Smirnov, A., Eck, T. F., Slutsker, I., Abuhassan, N., Newcomb, W. W., Schafer, J. S., Chatenet, B., Lavenu, F., Kaufman, Y. J., Castle, J. V., Setzer, A., Markham, B.,

Clark, D., Frouin, R., Halthore, R., Karneli, A., O'Neill, N. T., Pietras, C., Pinker, R. T., Voss, K., and Zibordi, G.: An emerging ground-based aerosol climatology: Aerosol optical depth from AERONET, Journal of Geophysical Research: Atmospheres (1984–2012), 106, 12067–12097, https://doi.org/10.1029/2001JD900014, 2001.

Hubanks, P. A.: MODIS Atmosphere QA Plan for Collection 005, Greenbelt, MD USA, NASA Goddard Space Flight Center, 57, 2012.

Hubanks, P. A., King, M. D., Platnick, S., and Pincus, R.: MODIS atmosphere L3 gridded product algorithm theoretical basis document, ATBD Reference Number: ATBD-MOD-30 (http://modis-atmos. gsfc. nasa. gov/MOD08_M3/atbd. html), 2008.

Ichoku, C., Chu, D. A., Mattoo, S., Kaufman, Y. J., Remer, L. A., Tanre, D., Slutsker, I., and Holben, B. N.: A spatio-temporal approach for global validation and analysis of MODIS aerosol products, Geophys Res Lett, 29, https://doi.org/10.1029/2001GL013206, 2002.

Ichoku, C., Remer, L. A., Kaufman, Y. J., Levy, R., Chu, D. A., Tanré, D., and Holben, B. N.: MODIS observation of aerosols and estimation of aerosol radiative forcing over southern Africa during SAFARI 2000, J. Geophys. Res., 108, 2002JD002366, https://doi.org/10.1029/2002JD002366, 2003.

Ignatov, A., Minnis, P., Loeb, N., Wielicki, B., Miller, W., Sun-Mack, S., Tanré, D., Remer, L., Laszlo, I., and Geier, E.: Two MODIS Aerosol Products over Ocean on the Terra and Aqua CERES SSF Datasets, Journal of the Atmospheric Sciences, 62, 1008–1031, https://doi.org/10.1175/JAS3383.1, 2005.

IPCC, I. P. on C. C.: Climate Change 2007 - The Physical Science Basis, Cambridge University Press, 2007.

Karnieli, A., Kaufman, Y. J., Remer, L., and Wald, A.: AFRI — aerosol free vegetation index, Remote Sensing of Environment, 77, 10–21, https://doi.org/10.1016/S0034-4257(01)00190-0, 2001.

Kaufman, Y., Gobron, N., Pinty, B., Widlowski, J., and Verstraete, M.: Relationship between surface reflectance in the visible and mid-IR used in MODIS aerosol algorithm - theory, Geophys Res Lett, 29, preprint no.-2116, https://doi.org/10.1029/2001GL014492, 2002.

Kaufman, Y. J., Tanre, D., Remer, L. A., Vermote, E. F., Chu, A., and Holben, B. N.: Operational remote sensing of tropospheric aerosol over land from EOS moderate resolution imaging spectroradiometer, J. Geophys. Res., 102, 17051–17067, https://doi.org/10.1029/96JD03988, 1997a.

Kaufman, Y. J., Wald, A. E., Remer, L. A., Bo-Cai Gao, Rong-Rong Li, and Flynn, L.: The MODIS 2.1-μm channel-correlation with visible reflectance for use in remote sensing of aerosol, IEEE Trans. Geosci. Remote Sensing, 35, 1286–1298, https://doi.org/10.1109/36.628795, 1997b.

Kaufman, Y. J., Boucher, O., Tanré, D., Chin, M., Remer, L. A., and Takemura, T.: Aerosol anthropogenic component estimated from satellite data, Geophysical Research Letters, 32, 2005GL023125, https://doi.org/10.1029/2005GL023125, 2005.

Kim, M., Levy, R. C., Remer, L. A., Mattoo, S., and Gupta, P.: Parameterizing spectral surface reflectance relationships for the Dark Target aerosol algorithm applied to a geostationary imager, Atmos. Meas. Tech., 17, 1913–1939, https://doi.org/10.5194/amt-17-1913-2024, 2024..

King, M. D., Kaufman, Y. J., Menzel, W. P., and Tanre, D.: Remote sensing of cloud, aerosol, and water vapor properties from the moderate resolution imaging spectrometer (MODIS), IEEE Trans. Geosci. Remote Sensing, 30, 2–27, https://doi.org/10.1109/36.124212, 1992.

King, M. D., Menzel, W. P., Grant, P. S., Myers, J. S., Arnold, G. T., Platnick, S. E., Gumley, L. E., Tsay, S.-C., Moeller, C. C., Fitzgerald, M., Brown, K. S., and Osterwisch, F. G.: Airborne Scanning Spectrometer for Remote Sensing of Cloud, Aerosol, Water Vapor, and Surface Properties, J. Atmos. Oceanic Technol., 13, 777–794, https://doi.org/10.1175/1520-0426(1996)013<0777:ASSFRS>2.0.CO;2, 1996.

King, M. D., Menzel, W. P., Kaufman, Y. J., Tanre, D., Bo-Cai Gao, Platnick, S., Ackerman, S. A., Remer, L. A., Pincus, R., and Hubanks, P. A.: Cloud and aerosol properties, precipitable water, and profiles of temperature and water vapor from MODIS, IEEE Trans. Geosci. Remote Sensing, 41, 442–458, https://doi.org/10.1109/TGRS.2002.808226, 2003.

King, M. D., Platnick, S., Menzel, W. P., Ackerman, S. A., and Hubanks, P. A.: Spatial and Temporal Distribution of Clouds Observed by MODIS Onboard the Terra and Aqua Satellites, IEEE Trans. Geosci. Remote Sensing, 51, 3826–3852, https://doi.org/10.1109/TGRS.2012.2227333, 2013.

Kleidman, R. G., O'Neill, N. T., Remer, L. A., Kaufman, Y. J., Eck, T. F., Tanré, D., Dubovik, O., and Holben, B. N.: Comparison of Moderate Resolution Imaging Spectroradiometer (MODIS) and Aerosol Robotic Network (AERONET) remote-sensing retrievals of aerosol fine mode fraction over ocean, J Geophys Res-Atmos, 110, 22205, https://doi.org/10.1029/2005JD005760, 2005.

Koepke, P.: Effective reflectance of oceanic whitecaps, Appl Optics, 23, 1816–1824, 1984.

Kotchenova, S. Y. and Vermote, E. F.: Validation of a vector version of the 6S radiative transfer code for atmospheric correction of satellite data Part II Homogeneous Lambertian and anisotropic surfaces, Appl. Opt., 46, 4455, https://doi.org/10.1364/AO.46.004455, 2007.

Kotchenova, S. Y., Vermote, E. F., Matarrese, R., and Klemm, Jr., F. J.: Validation of a vector version of the 6S radiative transfer code for atmospheric correction of satellite data Part I: Path radiance, Appl. Opt., 45, 6762, https://doi.org/10.1364/AO.45.006762, 2006.

Levy, R. C., Remer, L. A., and Kaufman, Y. J.: Effects of neglecting polarization on the MODIS aerosol retrieval over land, IEEE Trans. Geosci. Remote Sensing, 42, 2576–2583, https://doi.org/10.1109/TGRS.2004.837336, 2004.

Levy, R. C., Remer, L. A., Martins, J. V., Kaufman, Y. J., Plana-Fattori, A., Redemann, J., and Wenny, B.: Evaluation of the MODIS aerosol retrievals over ocean and land during CLAMS, J Atmos Sci, 62, 974–992, https://doi.org/10.1175/JAS3391.1, 2005.

Levy, R. C., Remer, L. A., and Dubovik, O.: Global aerosol optical properties and application to Moderate Resolution Imaging Spectroradiometer aerosol retrieval over land, J Geophys Res-Atmos, 112, D13210, https://doi.org/10.1029/2006JD007815, 2007a.

Levy, R. C., Remer, L. A., Mattoo, S., Vermote, E. F., and Kaufman, Y. J.: Second-generation operational algorithm: Retrieval of aerosol properties over land from inversion of Moderate Resolution Imaging Spectroradiometer spectral reflectance, Journal of Geophysical Research: Atmospheres (1984–2012), 112, D13211, https://doi.org/10.1029/2006JD007811, 2007b.

Levy, R. C., Leptoukh, G. G., Kahn, R., Zubko, V., Gopalan, A., and Remer, L. A.: A Critical Look at Deriving Monthly Aerosol Optical Depth From Satellite Data, Ieee T Geosci Remote, 47, 2942–2956, https://doi.org/10.1109/TGRS.2009.2013842, 2009a.

Levy, R. C., Remer, L. A., Tanré, D., Mattoo, S., and Kaufman, Y. J.: ALGORITHM FOR REMOTE SENSING OF TROPOSPHERIC AEROSOL OVER DARK TARGETS FROM MODIS: Collections 005 and 051: Revision 2; Feb 2009, MODIS Algorithm Theoretical Basis Document, 2009b.

Levy, R. C., Mattoo, S., Munchak, L. A., Remer, L. A., Sayer, A. M., Patadia, F., and Hsu, N. C.: The Collection 6 MODIS aerosol products over land and ocean, Atmos Meas Tech, 6, 2989–3034, https://doi.org/10.5194/amt-6-2989-2013, 2013.

Levy, R. C., Munchak, L. A., Mattoo, S., Patadia, F., Remer, L. A., and Holz, R. E.: Towards a long-term global aerosol optical depth record: applying a consistent aerosol retrieval algorithm to MODIS and VIIRS-observed reflectance, Atmos Meas Tech, 8, 4083–4110, https://doi.org/10.5194/amt-8-4083-2015, 2015.

Levy, R. C., Mattoo, S., Sawyer, V., Shi, Y., Colarco, P. R., Lyapustin, A. I., Wang, Y., and Remer, L. A.: Exploring systematic offsets between aerosol products from the two MODIS sensors, Atmos Meas Tech, 11, 4073–4092, https://doi.org/10.5194/amt-11-4073-2018, 2018.

Li, R. R., Remer, L., Kaufman, Y. J., Mattoo, S., Gao, B. C., and Vermote, E.: Snow and Ice Mask for the MODIS Aerosol Products, Geoscience and Remote Sensing Letters, IEEE, 2, 306–310, https://doi.org/10.1109/LGRS.2005.847755, 2005.

Livingston, J. M., Redemann, J., Shinozuka, Y., Johnson, R., Russell, P. B., Zhang, Q., Mattoo, S., Remer, L., Levy, R., Munchak, L., and Ramachandran, S.: Comparison of MODIS 3 km and 10 km resolution aerosol optical depth retrievals over land with airborne sunphotometer measurements during ARCTAS summer 2008, Atmospheric Chemistry and Physics Discussions, 13, 15007–15059, https://doi.org/10.5194/acpd-13-15007-2013, 2013.

Lucchesi, R.: File Specification for GEOS-5 FP-IT (Forward Processing for Instrument Teams) GMAO Office Note No. 2 (Version 1.3), 2015.

Lyapustin, A. and Kaufman, Y.: Role of adjacency effect in the remote sensing of aerosol, J Geophys Res-Atmos, 106, 11909–11916, 2001.

Martins, J. V., Tanré, D., Remer, L., Kaufman, Y., Mattoo, S., and Levy, R.: MODIS Cloud screening for remote sensing of aerosols over oceans using spatial variability, Geophysical Research Letters, 29, https://doi.org/10.1029/2001GL013252, 2002.

McGill, M., Hlavka, D., Hart, W., Scott, V. S., Spinhirne, J., and Schmid, B.: Cloud Physics Lidar: instrument description and initial measurement results, Appl Optics, 41, 3725–3734, https://doi.org/10.1364/AO.41.003725, 2002.

Meister, G., Franz, B. A., Kwiatkowska, E. J., and McClain, C. R.: Corrections to the Calibration of MODIS Aqua Ocean Color Bands Derived From SeaWiFS Data, Ieee T Geosci Remote, 50, 310–319, https://doi.org/10.1109/TGRS.2011.2160552, 2012.

Meyer, K., Platnick, S., Arnold, G. T., Holz, R. E., Veglio, P., Yorks, J., and Wang, C.: Cirrus cloud optical and microphysical property retrievals from eMAS during SEAC<sup>4</sup>RS using bi-spectral reflectance measurements within the 1.88 μm water vapor absorption band, Atmos. Meas. Tech., 9, 1743–1753, https://doi.org/10.5194/amt-9-1743-2016, 2016.

Omar, A. H., Won, J., Winker, D. M., Yoon, S., Dubovik, O., and McCormick, M. P.: Development of global aerosol models using cluster analysis of Aerosol Robotic Network (AERONET) measurements, J. Geophys. Res., 110, 2004JD004874, https://doi.org/10.1029/2004JD004874, 2005.

O'Neill, N., Eck, T., Smirnov, A., Holben, B., and Thulasiraman, S.: Spectral discrimination of coarse and fine mode optical depth, J Geophys Res-Atmos, 108, 4559, https://doi.org/10.1029/2002JD002975, 2003.

Patadia, F., Levy, R. C., and Mattoo, S.: Correcting for trace gas absorption when retrieving aerosol optical depth from satellite observations of reflected shortwave radiation, Atmos Meas Tech, 11, 3205–3219, https://doi.org/10.5194/amt-11-3205-2018, 2018.

Petrenko, M., Ichoku, C., and Leptoukh, G.: Multi-sensor Aerosol Products Sampling System (MAPSS), Atmos Meas Tech, 5, 913–926, https://doi.org/10.5194/amt-5-913-2012, 2012.

Remer, L., Wald, A., and Kaufman, Y.: Angular and seasonal variation of spectral surface reflectance ratios: Implications for the remote sensing of aerosol over land, Ieee T Geosci Remote, 39, 275–283, 2001.

Remer, L. A. and Kaufman, Y. J.: Dynamic aerosol model: Urban/industrial aerosol, J. Geophys. Res., 103, 13859-13–871, https://doi.org/10.1029/98JD00994, 1998.

Remer, L. A., Kaufman, Y. J., Tanré, D., Mattoo, S., Chu, D. A., Martins, J. V., Li, R.-R., Ichoku, C., Levy, R. C., Kleidman, R. G., Eck, T. F., Vermote, E., and Holben, B. N.: The MODIS Aerosol Algorithm, Products, and Validation, Journal of the Atmospheric Sciences, 62, 947–973, https://doi.org/10.1175/JAS3385.1, 2005.

Remer, L. A., Kleidman, R. G., Levy, R. C., Kaufman, Y. J., Tanré, D., Mattoo, S., Martins, J. V., Ichoku, C., Koren, I., Yu, H., and Holben, B. N.: Global aerosol climatology from the MODIS

satellite sensors, J Geophys Res-Atmos, 113, D14S07, https://doi.org/10.1029/2007JD009661, 2008.

Remer, L. A., Mattoo, S., Levy, R. C., and Munchak, L. A.: MODIS 3 km aerosol product: algorithm and global perspective, Atmos. Meas. Tech., 6, 1829–1844, https://doi.org/10.5194/amt-6-1829-2013, 2013.

Remer, L. A., Levy, R. C., Mattoo, S., Tanré, D., Gupta, P., Shi, Y., Sawyer, V., Munchak, L. A., Zhou, Y., Kim, M., Ichoku, C., Patadia, F., Li, R.-R., Gasso, S., Kleidman, R. G., and Holben, B. N.: The Dark Target Algorithm for Observing the Global Aerosol System: Past, Present, and Future, Remote Sensing, 12, https://doi.org/10.3390/rs12182900, 2020.

Salomonson, V. V., Barnes, W. L., Maymon, P. W., Montgomery, H. E., and Ostrow, H.: MODIS: advanced facility instrument for studies of the Earth as a system, IEEE Trans. Geosci. Remote Sensing, 27, 145–153, https://doi.org/10.1109/36.20292, 1989.

Salomonson, V. V., Barnes, W., Xiong, J., Kempler, S., and Masuoka, E.: An overview of the Earth Observing System MODIS instrument and associated data systems performance, in: IEEE International Geoscience and Remote Sensing Symposium, IEEE International Geoscience and Remote Sensing Symposium. IGARSS 2002, Toronto, Ont., Canada, 1174–1176, https://doi.org/10.1109/IGARSS.2002.1025812, 2002.

Sawyer, V., Levy, R. C., Mattoo, S., Cureton, G., Shi, Y., and Remer, L. A.: Continuing the MODIS Dark Target Aerosol Time Series with VIIRS, Remote Sensing, 12, 308, https://doi.org/10.3390/rs12020308, 2020.

Shi, Y. R., Levy, R. C., Remer, L. A., Mattoo, S., and Arnold, G. T.: Investigating the Spatial and Temporal Limitations for Remote Sensing of Wildfire Smoke Using Satellite and Airborne Imagers During FIREX-AQ, JGR Atmospheres, 129, e2023JD039085, https://doi.org/10.1029/2023JD039085, 2024.

Sinyuk, A., Holben, B. N., Eck, T. F., Giles, D. M., Slutsker, I., Korkin, S., Schafer, J. S., Smirnov, A., Sorokin, M., and Lyapustin, A.: The AERONET Version 3 aerosol retrieval algorithm, associated uncertainties and comparisons to Version 2, Atmos. Meas. Tech., 13, 3375–3411, https://doi.org/10.5194/amt-13-3375-2020, 2020.

Sun, J., Xiong, X., Angal, A., Chen, H., Geng, X., and Wu, A.: On-orbit performance of the MODIS reflective solar bands time-dependent response versus scan angle algorithm, in: SPIE Optical Engineering + Applications, SPIE Optical Engineering + Applications, 85100J, https://doi.org/10.1117/12.930021, 2012.

Tanré, D., Herman, M., and Kaufman, Y. J.: Information on aerosol size distribution contained in solar reflected spectral radiances, J. Geophys. Res., 101, 19043–19060, https://doi.org/10.1029/96JD00333, 1996.

Tanre, D., Kaufman, Y. J., Herman, M., and Mattoo, S.: Remote sensing of aerosol properties over oceans using the MODIS/EOS spectral radiances, Journal of Geophysical Research: Atmospheres (1984–2012), 102, 16971–16988, https://doi.org/10.1029/96JD03437, 1997.

Toon, O. B., Maring, H., Dibb, J., Ferrare, R., Jacob, D. J., Jensen, E. J., Luo, Z. J., Mace, G. G., Pan, L. L., Pfister, L., Rosenlof, K. H., Redemann, J., Reid, J. S., Singh, H. B., Thompson, A. M., Yokelson, R., Minnis, P., Chen, G., Jucks, K. W., and Pszenny, A.: Planning, implementation, and scientific goals of the Studies of Emissions and Atmospheric Composition, Clouds and Climate Coupling by Regional Surveys (SEAC4RS) field mission, J Geophys Res-Atmos, 121, 4967–5009, https://doi.org/10.1002/2015JD024297, 2016.

Tucker, C. J.: Red and photographic infrared linear combinations for monitoring vegetation, Remote Sensing of Environment, 8, 127–150, https://doi.org/10.1016/0034-4257(79)90013-0, 1979.

Vermote, E. F., Tanre, D., Deuze, J. L., Herman, M., and Morcette, J. J.: Second Simulation of the Satellite Signal in the Solar Spectrum, 6S: an overview, Ieee T Geosci Remote, 35, 675–686, https://doi.org/10.1109/36.581987, 1997.

Wang, D., Morton, D., Masek, J., Wu, A., Nagol, J., Xiong, X., Levy, R., Vermote, E., and Wolfe, R.: Impact of sensor degradation on the MODIS NDVI time series, Remote Sensing of Environment, 119, 55–61, https://doi.org/10.1016/j.rse.2011.12.001, 2012.

Warneke, C., Schwarz, J. P., Dibb, J., Kalashnikova, O., Frost, G., Al-Saad, J., Brown, S. S., Brewer, Wm. A., Soja, A., Seidel, F. C., Washenfelder, R. A., Wiggins, E. B., Moore, R. H., Anderson, B. E., Jordan, C., Yacovitch, T. I., Herndon, S. C., Liu, S., Kuwayama, T., Jaffe, D., Johnston, N., Selimovic, V., Yokelson, R., Giles, D. M., Holben, B. N., Goloub, P., Popovici, I., Trainer, M., Kumar, A., Pierce, R. B., Fahey, D., Roberts, J., Gargulinski, E. M., Peterson, D. A., Ye, X., Thapa, L. H., Saide, P. E., Fite, C. H., Holmes, C. D., Wang, S., Coggon, M. M., Decker, Z. C. J., Stockwell, C. E., Xu, L., Gkatzelis, G., Aikin, K., Lefer, B., Kaspari, J., Griffin, D., Zeng, L., Weber, R., Hastings, M., Chai, J., Wolfe, G. M., Hanisco, T. F., Liao, J., Campuzano Jost, P., Guo, H., Jimenez, J. L., Crawford, J., and The FIREX-AQ Science Team: Fire Influence on Regional to Global Environments and Air Quality (FIREX-AQ), JGR Atmospheres, 128, e2022JD037758, https://doi.org/10.1029/2022JD037758, 2023.

Wiscombe, W. J.: Improved Mie scattering algorithms, Appl. Opt., 19, 1505, https://doi.org/10.1364/AO.19.001505, 1980.

Witte, J. C., Douglass, A. R., da Silva, A., Torres, O., Levy, R., and Duncan, B. N.: NASA A-Train and Terra observations of the 2010 Russian wildfires, Atmospheric Chemistry and Physics, 11, 9287–9301, https://doi.org/10.5194/acp-11-9287-2011, 2011.

Yu, H., Kaufman, Y. J., Chin, M., Feingold, G., Remer, L. A., Anderson, T. L., Balkanski, Y., Bellouin, N., Boucher, O., Christopher, S., DeCola, P., Kahn, R., Koch, D., Loeb, N., Reddy, M. S., Schulz, M., Takemura, T., and Zhou, M.: A review of measurement-based assessments of the aerosol direct radiative effect and forcing, Atmospheric Chemistry and Physics, 6, 613–666, https://doi.org/10.5194/acp-6-613-2006, 2006.

Zhang, H., Kondragunta, S., Laszlo, I., and Zhou, M.: Improving GOES Advanced Baseline Imager (ABI) aerosol optical depth (AOD) retrievals using an empirical bias correction algorithm, Atmos. Meas. Tech., 13, 5955–5975, https://doi.org/10.5194/amt-13-5955-2020, 2020.

Zhang, Y., Yu, H., Eck, T. F., Smirnov, A., Chin, M., Remer, L. A., Bian, H., Tan, Q., Levy, R., Holben, B. N., and Piazzolla, S.: Aerosol daytime variations over North and South America derived from multiyear AERONET measurements, J. Geophys. Res., 117, D05211, https://doi.org/10.1029/2011JD017242, 2012.

Zhou, Y., Levy, R. C., Remer, L. A., Mattoo, S., and Espinosa, W. R.: Dust Aerosol Retrieval Over the Oceans With the MODIS/VIIRS Dark Target Algorithm: 2. Nonspherical Dust Model, Earth and Space Science, 7, https://doi.org/10.1029/2020EA001222, 2020a.

Zhou, Y., Levy, R. C., Remer, L. A., Mattoo, S., Shi, Y., and Wang, C.: Dust Aerosol Retrieval Over the Oceans With the MODIS/VIIRS Dark-Target Algorithm: 1. Dust Detection, Earth and Space Science, 7, https://doi.org/10.1029/2020EA001221, 2020b.

APPENDICES

A1. Calculation of Central Wavelength and Gas Corrections

The DT aerosol algorithm is based on a LUT approach and uses calibrated and geolocated L1B reflectance as inputs (for e.g. MxD02 and MxD03 for MODIS). Thus, we need to characterize the spectral properties of the sensor as well as the atmosphere which it is observing.

Multi-spectral imagers such as MODIS, VIIRS, ABI, AHI and eMAS all rely on relatively broad-wavelength spectral bands (~20-50 nm) to optimize signal-to-noise vis-à-vis spatial resolution. Although the DT aerosol retrieval mainly uses wavelengths that are in "window" regions, gas absorptions are not zero and may be as high as optical depth 0.02 or even 0.05. At the same time, molecular (Rayleigh) optical depth (ROD) is non-zero, and as high as 0.2 in the Blue wavelength bands. The strategy for DT, then, is to "correct" the observations for gas-absorption, and "include" the Rayleigh within the LUTs. Both corrections require exact knowledge of the sensor's wavelength band.

A sensor's relative spectral response function (SRF) is a measure of how sensitive an instrument's photosensor is to radiation of a particular wavelength. While each band is engineered to be sensitive to a specific minimum, center, and maximum wavelength, with statistical shape (e.g. Gaussian), on-orbit SRFs will be different. For the satellite imagers, these are derived in the lab just prior to launch. In the case of eMAS, these SRFs are derived for individual field campaigns. Each sensor's instrument team keeps tables of SRF, however they have been consolidated at sites such as ESA's (https://nwp-saf.eumetsat.int/site/software/rttov/download/coefficients/spectral-response-functions/#visir (last accessed on 09/06/2023). Examples of SRF are used for creating the Figure A 1-1. In some cases, tables of SRF also note the presence of out-of-band (OOB) response, which indicates the band is sensitive to radiation in wavelengths far from intended in-band (IB). For example, the SNPP-VIIRS M1 (nominal 0.412 μm) band shows signal around 0.770 μm (see this link), but we choose to ignore OOB in our calculations.

Noting the shapes of the SRFs from the Figure A 1-1, we see that these are neither Gaussian, Square nor any other simple shape. Therefore, we must account for RSR to determine the expected effects from aerosol, Rayleigh scattering, and trace gas absorptions. Let us define a one-percent response as anywhere in the band where the SRF is ≥1% of the maximum signal, and half-max (HM) as where SRF is ≥ 50% of the maximum. Although it could be defined either way, we note the distance between the first and last HM (the full width half max or FWHM) and define the midpoint as the *center wavelength*.

We have other choices to characterize a band. A general equation for computing effects is given on NASA's ocean color web page (see this link) as:

$$X = \frac{\int_{\lambda min}^{\lambda max} x(\lambda) * SRF(\lambda) * W(\lambda) * d\lambda}{\int_{\lambda min}^{\lambda max} SRF(\lambda) * W(\lambda) * d\lambda} \qquad \text{Eq. A1-1}$$

Where X represents the quantity we want to calculate, and $x(\lambda)$ is also a function of wavelength. There may be additional weights (W) which are function of wavelength. These weights may be 1.0, or they may be external (for example E_0 = TOA solar irradiance). We may have to integrate one or more of these spectrally dependent functions, so that the equation can be computed. For example, we could compute a "centroid wavelength" of X where the small $x(\lambda)$ are the wavelengths themselves. For most bands, differences between center, centroid (using W = 1), and centroid solar (using $W = E_0(\lambda)$) lead to differences less than an nanometer. It turns out that for estimating aerosol scattering effects, for

MODIS we use the centroid (based on the band-averaged one-percent responses), whereas for VIIRS, ABI and AHI, we use the center (based on the HM).

Details matter even more for the computation of Rayleigh and gas absorption effects. To account for each of these effects we also must know the spectral dependencies of incoming solar radiation, Rayleigh optical depth, and gas-absorption coefficients of different trace gases. For Rayleigh (optical depths and King depolarization factors), we use Bodhaine et al., [*1999*], and assume we are at 45°N and at sea level. For solar irradiance, and for MODIS we used the Thuillier et al. [*2002*], however for VIIRS, ABI and AHI we use Total and Spectral Solar Irradiance Sensor-1 (TSIS-1) Hybrid Solar Reference Spectrum (HSRS) (https://lasp.colorado.edu/lisird/data/tsis1_hsrs; Coddington et al., [*2021*]) interpolated at 1-nm is used as the reference spectrum for computing the band average.
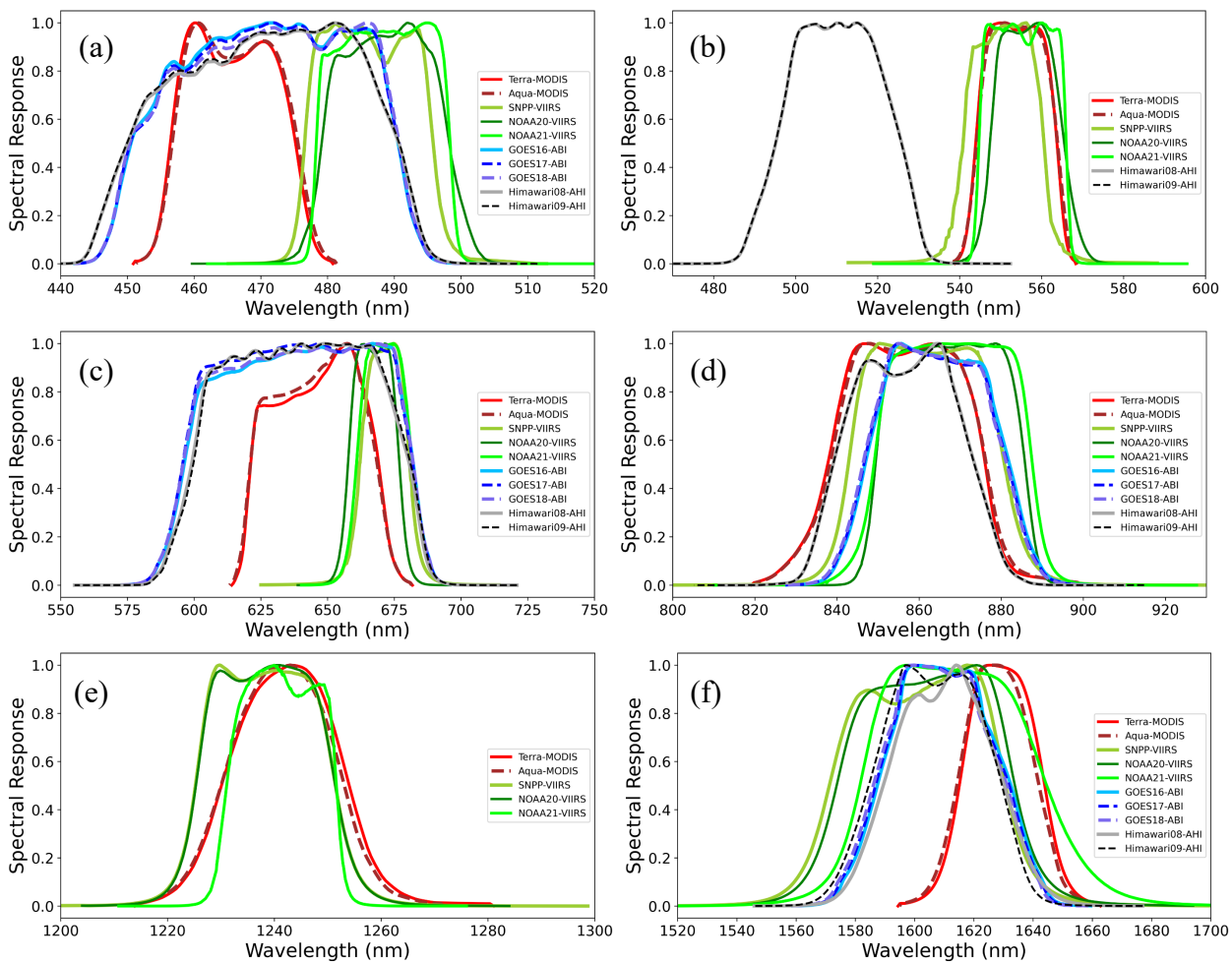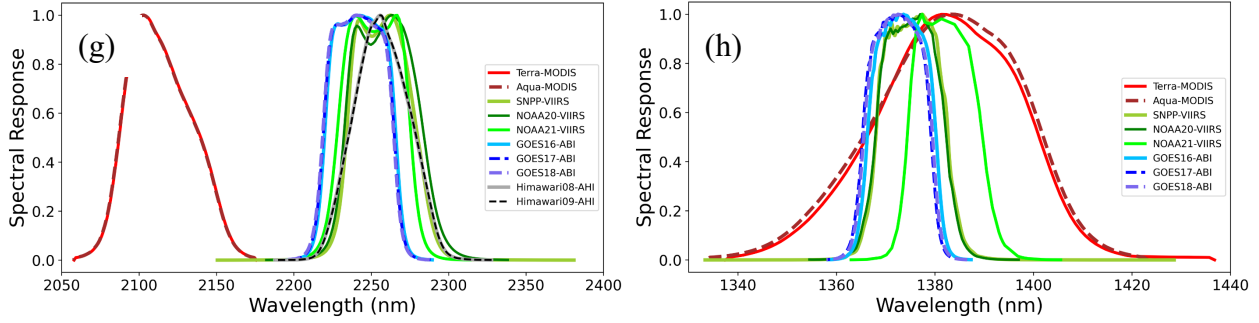
Figure A 1-1: Averaged and interpolated Spectral Response Functions of (a) blue, (b) green, (c) red, (d) NIR, (e) SWIR-1, (f) SWIR-2, (g) SWIR-3, and (h) SWIR bands used in DT aerosol retrieval algorithms are shown for various sensors.

Because the LUT is calculated without accounting for the absorption by major gas constituents such as atmospheric water vapor, ozone, and "dry gas" (include CO2, CO, N2O, NO2, NO, CH4, O2, SO2), an alternative technique must be substituted to account for the effect of these gases within each wavelength band. Without this gas correction, the retrieval algorithm will be matching the measured TOA reflectance to the LUT-calculated reflectance for which the LUT values will be brighter than the measured values for the same amount of aerosol. This leads to the false interpretation of aerosol loading in the atmosphere. Therefore, the gas correction algorithm must deal with this mismatch between measured and LUT reflectance by adjusting the measured TOA reflectance in each wavelength band. Essentially, we multiply the L1B TOA observations by the inverse of the gas-absorbed transmission to derive the corrected "measured" observations. We assume that water vapor and ozone are scene dependent (values provided by ancillary meteorological analysis), whereas carbon dioxide, methane and other "dry gases" are equal to a climatology.

Assuming the atmosphere is a simple spherical shell, the air mass factor (G) is approximated by [Gueymard, 1995]:

$$G = \sqrt{(r\cos(z))^2 + 2r + 1} - r\cos(z) \qquad \text{Eq. A1-2}$$

where Z is the zenith angle for a homogenous atmosphere; $r = R_E/H_{atm}$, R_E is the radius of Earth (6371 km) and H_{atm} is the effective scale height of the atmosphere.

However, water vapor (concentrated near the surface) and ozone (concentrated in the stratosphere) are not well mixed in the vertical and therefore have different scale heights. In this layered situation (rather than continuous), there are empirical formulas that provide slight improvements in the calculation of G assuming a spherical geometry. For example, Gueymard (1995) derived the empirical formula,

$$G^i = (\cos Z + a_{i,1} Z^{a_{i,2}} (a_{i,3} - Z)^{a_{i,4}})^{-1} \qquad \text{Eq. A1-3}$$

where $a_{i,j}$ are the coefficients (j = 1- 4) for gas type i. Thus, G^i varies with gas type and specific profile within the atmosphere. The values of coefficients $a_{i,j}$ can be found in Table 4.1 of Gueymard [1995].

As long as the total gas optical depth is small $(\Sigma_i \tau_\lambda^i \ll 1)$, the total transmission of all trace gases is well approximated by the product of each individual gas:

$$T_\lambda^{GAS} = \prod_i T_\lambda^i = exp\left(\sum_i - G^i \tau_\lambda^i\right) \qquad \text{Eq. A1-4}$$

The total gas transmissivity defined in Eq. (A1-3) for each wavelength band quantifies the degree to which the measured reflectance will be diminished due to gaseous absorption. In order to match the measured reflectance to those calculated for the LUT, this diminished reflectance have to be "corrected" or brightened. This correction factor is simply the inverse transmissivity ($\tilde{T}$),

$$\tilde{T}_\lambda^{GAS} = 1/T_\lambda^{GAS} = exp\left(\sum_i G^i \tau_\lambda^i\right) \qquad \text{Eq. A1-5}$$

which when multiplied with the measured reflectance, restores the amount of light absorbed by gases along the one-way path of the transmission. Or, given a measured radiance, L_M, the corrected (brightened) radiance L is simply $L = L_M \cdot \tilde{T}$. A satellite measures radiation that has traveled downwards through the atmosphere and then back up to space. To account for this, a two-way correction factor needs to be calculated, and this correction factor must also account for the Z angles of both downward (the solar zenith angle) and upward (viewing zenith) paths.

The line-by-line radiative transfer model ([LBLRTM](#)) model is accurate and efficient for calculating radiances from ultraviolet (UV) through microwave wavelengths. Patadia et al., [*2018*] describe the method used to parameterize water vapor, ozone, and "dry gas" optical depths and thereby their transmission corrections. Essentially, we ran LBLRTM for several selected scenarios representing different combinations of vertical gas profiles, gas concentrations, and air mass factors for each gas type and wavelength band of interest. Transmissions of the 10 important atmospheric gases – viz. H_2O, O_3, O_2, N_2O, NO_2, NO, SO_2, CO_2, CO and CH_4 – those affect the spectral bands [*Levy et al., 2013*] were also calculated. $\tilde{T}_\lambda^{Gas}$ are affected by the vertical distribution of gases in the atmospheric column, especially at oblique zenith angles. To account for this effect in formulating the parameterization, 52 atmospheric profiles representing diverse geographical locations and seasons were obtained from model simulations. For H_2O and O_3, and each of their respective profiles, LBLRTM is used to calculate air mass factors and transmissions at 10 discrete viewing zenith angles, ranging from 0 to 80. Transmission is integrated across each wavelength band and weighted by the SRF as within that specific band. Finally, we develop a linear or quadratic (in log-space) formulas to parametrize relationships for water vapor and ozone, respectively, with integrated value of the constituent expected to come from the ancillary meteorological re-analysis. Column concentrations of "dry gas" are assumed to be globally constant with the values given in the US76 profiles. If there is no ancillary information provided during the DT retrieval, the algorithm can proceed, but assumes US76 values for water vapor and ozone

$T\lambda\ H_2O\ = exp\big(exp\ (K_{1,\lambda}^{H_2O} + K_{2,\lambda}^{H_2O} ln(G^{H_2O}w) + K_{3,\lambda}^{H_2O}[\ln (G^{H_2O}w)]^2)\big)$ Eq. A1-6 describes the derived quadratic empirical relationship (seen in Figure A1-4 and Figure A1-4) between the gas transmission correction factor of water vapor ($\tilde{T}_\lambda^{H2O}$), its concentration (w) and the air mass factor (G^{H_2O}). With valid values (from ancillary meteorology) of water vapor, the transmission factor $\tilde{T}_\lambda^{H2O}$ for water vapor calculated by:

$$\tilde{T}_\lambda^{H_2O} = exp\big(exp\ (K_{1,\lambda}^{H_2O} + K_{2,\lambda}^{H_2O} ln(G^{H_2O}w) + K_{3,\lambda}^{H_2O}[\ln (G^{H_2O}w)]^2)\big) \qquad \text{Eq. A1-6}$$

If not, we derive transmission as:

$$\tilde{T}_\lambda^{H_2O} = exp\left(G^{H_2O}\overline{\tau_\lambda^{H_2O}}\right) \qquad \text{Eq. A1-7}$$

where $\overline{\tau_\lambda^{H_2O}}$ are the climatological (US76) mean gas optical depths respectively for water vapor.

Ozone transmission $T_\lambda^{O_3}$ is calculated in a similar way, that is:

$$\tilde{T}_\lambda^{O_3} = exp\left(K_{1,\lambda}^{O_3} + K_{2,\lambda}^{O_3}(G^{O_3}O)\right) \qquad \text{Eq. A1-8}$$

for a valid ancillary value, "O" denotes ozone concentration in $T\lambda\ O_3\ = exp\left(K_{1,\lambda}^{O_3} + K_{2,\lambda}^{O_3}(G^{O_3}O)\right)$ Eq. A1-8, and G^{O_3} is the air mass factor for ozone and is computed using $Gi=(cos\ Z\ + a_{i,1}\ Z^{a_{i,2}}\ (a_{i,3} - Z)^{a_{i,4}})^{-1}$ Eq. A1-3. The regression coefficients $K_{1,\lambda}^{H_2O}, K_{2,\lambda}^{H_2O}$ and $K_{3,\lambda}^{H_2O}$ well as $K_{1,\lambda}^{O_3}$ and $K_{2,\lambda}^{O_3}$ (the slopes and intercepts) for H_2O and O_3 are wavelength dependent (lines of different color in Figure A1-2 and Figure A1-4) and in accordance with absorption characteristics specific to the gas.

If no valid ozone value, we assume:

$$\tilde{T}_\lambda^{O_3} = exp\left(G^{O_3}\overline{\tau_\lambda^{O_3}}\right) \qquad \text{Eq. A1-9}$$

where $\overline{\tau_\lambda^{O_3}}$ are the climatological (US76) mean gas optical depths respectively for ozone.

$\tilde{T}_\lambda^{DryGas}$ is the transmission factor due to dry gas, which includes CO_2, CO, N_2O, NO_2, NO, CH_4, O_2, SO_2, other trace gases and is given by:

$$\tilde{T}_\lambda^{DryGas} = exp\left(G^i \overline{\tau_\lambda^{DryGas}}\right)$$ Eq. A1-10

Therefore, we note the total gas transmission factor is a multiplication of all individual gas transmission terms, that is

$$\tilde{T}_\lambda^{gas} = \tilde{T}_\lambda^{H_2O}\tilde{T}_\lambda^{O_3}\tilde{T}_\lambda^{DryGas}$$ Eq. A1-11

and the corrected reflectance is given by

$$\rho_\lambda^{obs} = \tilde{T}_\lambda^{gas}\rho_\lambda^{L1B}$$ Eq. A1-12

Figures and $Gi = (cos\,Z + a_{i,1}\,Z^{a_{i,2}}\,(a_{i,3}-Z)^{a_{i,4}})^{-1}$ Eq. A1-3 $T\lambda GAS = iT\,\lambda\,i = exp(\sum_i - G^i\tau_\lambda^i)$ Eq. A1-4 describe the methodology and fitting for water vapor and ozone, using the example of MODIS/VIIRS SNPP channels 1-7. Values for center wavelength, Rayleigh optical depth, US76 optical depths for water vapor, ozone, and dry gas, and the coefficients for $T\lambda\,H_2O = exp(exp(K_{1,\lambda}^{H_2O} + K_{2,\lambda}^{H_2O}ln(G^{H_2O}w) + K_{3,\lambda}^{H_2O}[ln(G^{H_2O}w)]^2))$ Eq. A1-6 $T\lambda O\,3 = exp\left(K_{1,\lambda}^{O_3} + K_{2,\lambda}^{O_3}(G^{O_3}O)\right)$ Eq. A1-8 are presented in Table A1-1. These values are used in the MODIS C6.1, using an older version of LBLRTM. For completeness, we also provide values for additional MODIS wavelength bands, as the standard DT product (MODIS C6.1) provides corrected reflectance values for the variables known as "Mean_Reflectance_Land" and "Mean_Reflectance_Ocean".

For Version 2.0 of VIIRS, as well as the XAERDT product, we followed essentially the same procedures, but using a newer version (v12.2) version of LBLRTM. Table A1-2 to A1-12 list gas absorption coefficients and dry gas optical depths used in DT algorithm over all sensors. One can see between A1-2 and A1-1, the minor differences for MODIS when using the updated LBLRTM.
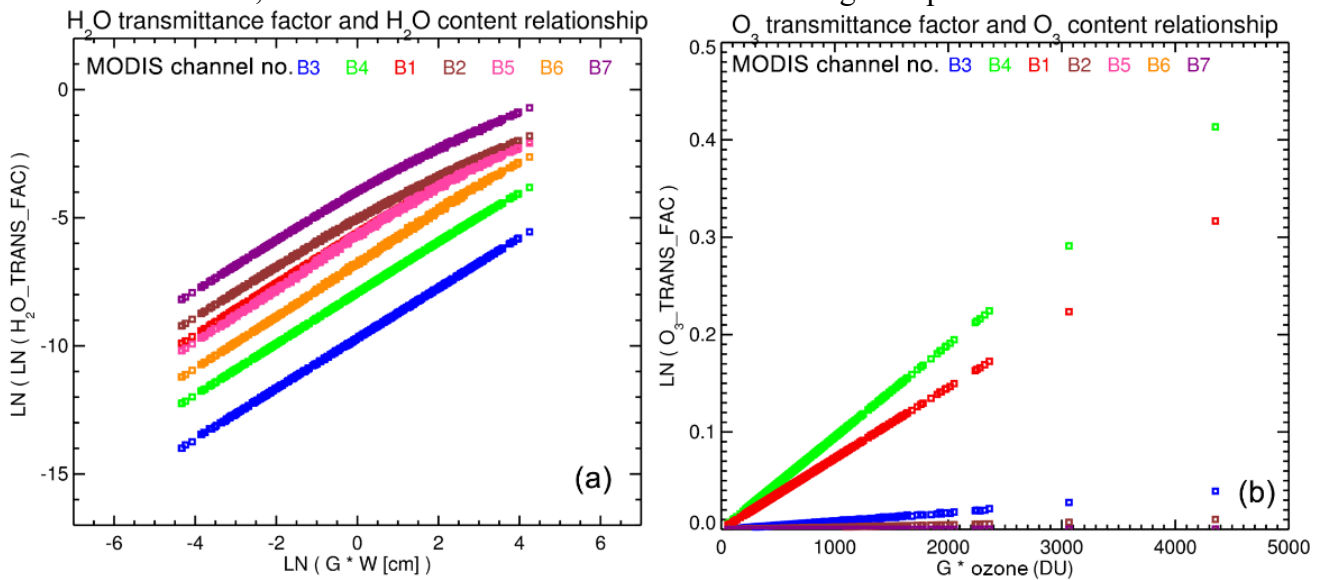
Figure A1-2: Relationship between gas transmission and gas content in the first 7 MODIS bands (a) H₂O Transmission Factor vs. H₂O content (cm) (b) O₃ Transmission Factor vs. O₃ content (DU). Gas Content is scaled by the air mass factor (G). Gas transmittance was calculated for 52 water vapor and ozone profiles (varying gas concentration) and 10 viewing zenith angles (air mass factor) ranging from 0 to 80. These wavelength-dependent empirical relationships are used by the DT aerosol retrieval algorithm for atmospheric gas corrections.
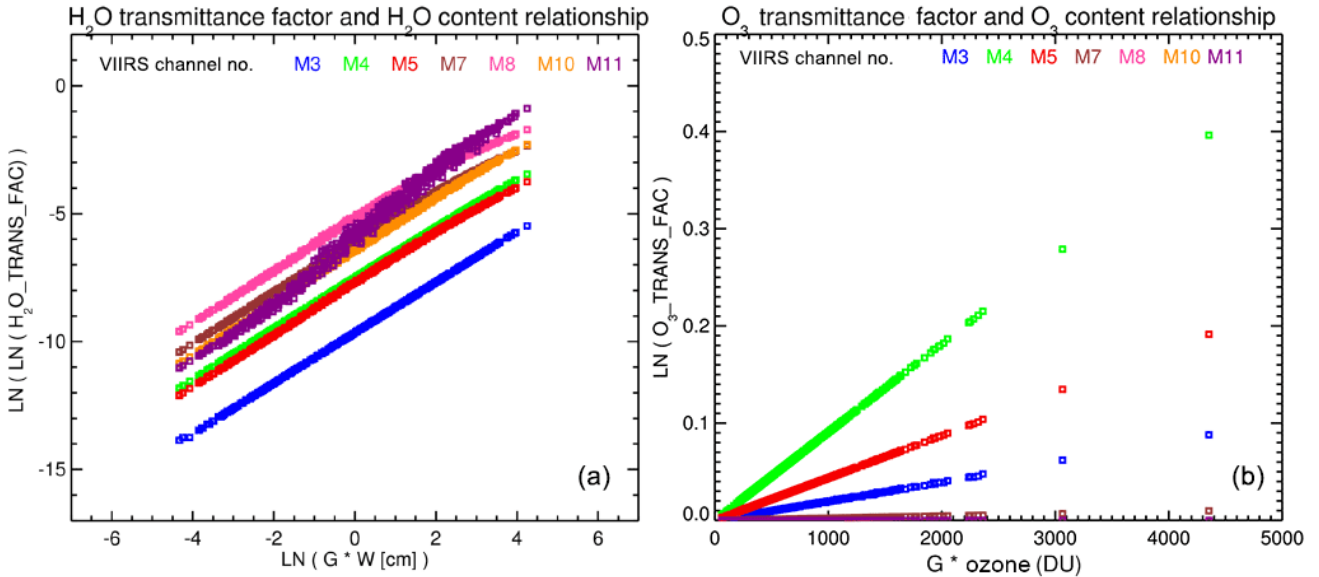
Figure A1-3: Relationship between gas transmission and gas content in the first 7 VIIRS SNPP bands (a) H2O Transmission Factor vs. H2O content (cm) (b) O3 Transmission Factor vs. O3 content (DU). Gas Content is scaled by the air mass factor (G). Gas transmittance was calculated for 52 water vapor and ozone profiles (varying gas concentration) and 10 viewing zenith angles (air mass factor) ranging from 0 to 80. These wavelength-dependent empirical relationships are used by the DT aerosol retrieval algorithm for atmospheric gas corrections.

Figure A1-4: Relative contribution of Dry Gas, Water Vapor, Ozone and Rayleigh optical depths in the first 7 MODIS bands

For each L1B data pixel, the following gas transmission factors are calculated as a function of wavelength, air mass factor and some weighting coefficients, K. **Error! Reference source not found.** lists the coefficients corresponding to each gas (water vapor, ozone and dry gas).

TABLE A1-1: GAS ABSORPTION COEFFICIENTS AND CLIMATOLOGY FOR MODIS SENSORS

MODIS Band	Wavelength	Rayleigh Optical Depth	O_3 Optical Depth[#]	H_2O Optical Depth[#]	Dry Gas[*] Optical Depth[#]	O_3_K0	O_3_K1	H_2O_K0	H_2O_K1	H_2O_K2
3	0.4659	1.92E-01	2.90E-03	8.00E-05	1.25E-03	-1.14E-04	8.69E-06	-9.58E+00	1.23E+00	-1.16E-01
4	0.5537	9.44E-02	3.26E-02	5.00E-04	9.50E-04	5.18E-06	9.50E-05	-7.91E+00	1.00E+00	-1.29E-02
1	0.6456	5.08E-02	2.52E-02	5.11E-03	3.91E-03	1.16E-04	7.32E-05	-5.60E+00	9.40E-01	-1.78E-02
2	0.8564	1.62E-02	8.10E-04	8.61E-03	2.00E-05	2.80E-07	2.36E-06	-5.07E+00	8.77E-01	-2.40E-02
5	1.2417	3.61E-03	0.00E+00	5.23E-03	1.69E-02	1.19E-07	1.55E-25	-5.65E+00	9.81E-01	-2.38E-02
6	1.6285	1.22E-03	0.00E+00	1.62E-03	9.98E-03	1.19E-07	5.17E-26	-6.80E+00	1.03E+00	-4.29E-03
7	2.1134	4.30E-04	2.00E-05	2.53E-02	1.63E-02	6.29E-07	7.03E-08	-3.98E+00	8.86E-01	-2.56E-02
8	0.4122	3.18E-01	7.00E-05	0.00E+00	4.00E-05	-8.74E-06	2.36E-07	-1.42E+01	1.21E+00	1.55E-01
9	0.4423	2.37E-01	9.81E-04	3.80E-04	3.70E-04	-5.65E-05	2.94E-06	-8.14E+00	1.02E+00	-2.42E-02
15	0.7467	2.80E-02	3.74E-03	1.90E-03	0.00E+00	-7.48E-05	1.10E-05	-6.73E+00	1.06E+00	-1.22E-02

* Dry Gas includes CO_2, CO, N_2O, NO_2, NO, CH_4, O_2, SO_2
\# For each MODIS band, this nadir looking (viewing zenith angle = 0) optical depth for the gas is computed from the US 1976 Standard Atmosphere in LBLRTM.

TABLE A1-2: MODIS GAS ABSORPTION COEFFICIENTS AND OPTICAL DEPTHS USED IN DT RETRIEVAL ALGORITHMS. USING LBLRTM, GAS ABSORPTION OPTICAL DEPTH IS CALCULATED FOR THE US 1976 STANDARD ATMOSPHERE.
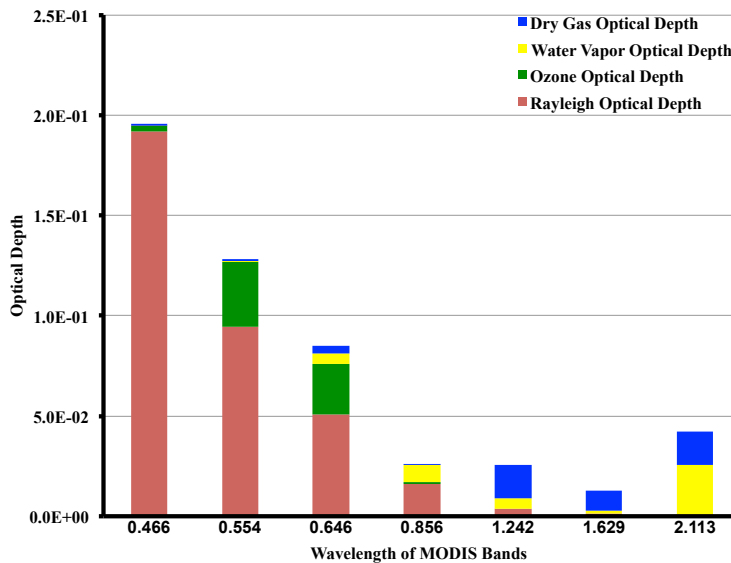
Band	Wavelength (μm)	Rayleigh Optical Depth	H_2O Optical depth	H_2O _K0	H_2O _K1	H_2O _K2	O_3 Optical depth	O_3_K0	O_3_K1	Dry-gas Optical depth
Blue	0.466	1.92E-01	1.63E-04	-9.36E+00	9.93E-01	-6.21E-04	2.91E-03	-1.14E-04	8.63E-06	1.22E-03
Green	0.5539	9.44E-02	7.09E-04	-7.90E+00	1.00E+00	-2.51E-03	3.27E-02	4.99E-06	9.51E-05	9.52E-04
Red	0.6449	5.08E-02	6.82E-03	-5.59E+00	9.37E-01	-1.83E-02	2.52E-02	1.18E-04	7.28E-05	3.87E-03
NIR	0.8569	1.62E-02	9.95E-03	-5.16E+00	8.73E-01	-2.15E-02	8.27E-04	3.68E-07	2.41E-06	2.87E-05
SWIR 1	1.2416	3.61E-03	7.95E-03	-5.53E+00	9.98E-01	-2.15E-02	1.19E-07	1.19E-07	-2.53E-24	1.56E-02
SWIR 2	1.6296	1.22E-03	2.38E-03	-6.73E+00	1.05E+00	1.73E-04	1.20E-06	3.48E-08	3.44E-09	9.65E-03
SWIR 3	2.1131	4.29E-04	3.38E-02	-3.97E+00	9.29E-01	-1.51E-02	2.63E-05	5.90E-07	7.53E-08	1.74E-02

TABLE A1-3: VIIRS-SNPP GAS ABSORPTION COEFFICIENTS AND OPTICAL DEPTHS

Band	Wavelength (μm)	Rayleigh Optical Depth	H_2O Optical depth	H_2O _K0	H_2O _K1	H_2O _K2	O_3 Optical depth	O_3_K0	O_3_K1	Dry-gas Optical depth
Blue	0.4862	1.60E-01	1.65E-04	-9.35E+00	9.98E-01	-3.84E-04	6.73E-03	-1.25E-04	1.98E-05	1.84E-03
Green	0.5507	9.74E-02	1.08E-03	-7.47E+00	9.93E-01	-2.87E-03	3.12E-02	-4.94E-06	9.06E-05	8.05E-04
Red	0.6714	4.39E-02	9.03E-04	-7.67E+00	9.97E-01	-1.09E-02	1.50E-02	-4.80E-05	4.37E-05	1.07E-03
NIR	0.8618	1.60E-02	4.54E-04	-6.03E+00	9.68E-01	-1.49E-02	7.70E-04	4.18E-07	2.24E-06	4.43E-05
SWIR 1	1.2384	3.65E-03	1.23E-02	-5.06E+00	9.65E-01	-2.58E-02	1.19E-07	1.19E-07	-2.69E-24	1.18E-02
SWIR 2	1.601	1.30E-03	3.36E-03	-6.38E+00	1.03E+00	-2.03E-03	9.42E-07	1.92E-08	2.50E-09	1.88E-02
SWIR 3	2.2569	3.29E-04	1.12E-02	-5.38E+00	1.30E+00	2.62E-03	9.58E-07	-6.36E-08	3.29E-09	4.84E-02

TABLE A1-4: VIIRS-NOAA20 GAS ABSORPTION COEFFICIENTS AND OPTICAL DEPTHS

Band	Wavelength (μm)	Rayleigh Optical Depth	H_2O Optical depth	H_2O _K0	H_2O _K1	H_2O _K2	O_3 Optical depth	O_3_K0	O_3_K1	Dry-gas Optical depth
Blue	0.4887	1.58E-01	1.97E-04	-9.17E+00	1.00E+00	-2.45E-03	7.25E-03	-1.25E-04	2.13E-05	9.48E-04

Green	0.5565	9.12E-02	5.16E-04	-8.22E+00	1.00E+00	-3.84E-03	3.43E-02	2.63E-05	9.96E-05	1.38E-03
Red	0.6673	4.40E-02	2.05E-03	-6.85E+00	9.90E-01	-1.38E-02	1.64E-02	-4.73E-05	4.77E-05	1.12E-05
NIR	0.8676	1.53E-02	2.51E-03	-6.66E+00	1.01E+00	-9.33E-03	7.06E-04	4.58E-07	2.05E-06	7.02E-05
SWIR 1	1.2384	3.65E-03	1.20E-02	-5.08E+00	9.68E-01	-2.55E-02	1.19E-07	1.19E-07	-2.64E-24	1.17E-02
SWIR 2	1.6038	1.30E-03	3.27E-03	-6.40E+00	1.03E+00	-2.09E-03	8.91E-07	1.23E-07	2.50E-09	1.79E-02
SWIR 3	2.2582	3.29E-04	1.18E-02	-5.32E+00	1.29E+00	2.44E-03	1.27E-06	-7.01E-08	3.76E-09	4.92E-02

TABLE A1-5: VIIRS-NOAA21 GAS ABSORPTION COEFFICIENTS AND OPTICAL DEPTHS

MODIS Band	Wavelength (μm)	Rayleigh Optical Depth	H_2O Optical depth	H_2O_K0	H_2O_K1	H_2O_K2	O_3 Optical depth	O_3_K0	O_3_K1	Dry-gas Optical depth
Blue	0.4884	1.60E-01	1.67E-04	-9.33E+00	1.00E+00	-1.73E-03	7.13E-03	-1.28E-04	2.09E-05	1.04E-03
Green	0.5553	9.41E-02	6.20E-04	-8.03E+00	1.00E+00	-2.48E-03	3.36E-02	2.17E-05	9.76E-05	1.17E-03
Red	0.6714	4.32E-02	9.58E-04	-7.63E+00	1.01E+00	-1.03E-02	1.50E-02	-4.60E-05	4.37E-05	1.61E-03
NIR	0.8683	1.53E-02	3.29E-03	-6.37E+00	9.84E-01	-1.34E-02	6.96E-04	4.52E-07	2.02E-06	7.77E-05
SWIR 1	1.2414	3.62E-03	5.22E-03	-6.01E+00	1.06E+00	-1.70E-02	1.19E-07	1.19E-07	-2.59E-24	1.24E-02
SWIR 2	1.6131	1.26E-03	3.40E-03	-6.37E+00	1.04E+00	-2.84E-03	8.78E-07	1.30E-07	2.46E-09	1.60E-02
SWIR 3	2.2517	3.33E-04	1.12E-02	-5.37E+00	1.29E+00	1.74E-03	2.32E-06	-1.87E-08	6.79E-09	4.36E-02

TABLE A1-6: ABI-GOES16 GAS ABSORPTION COEFFICIENTS AND OPTICAL DEPTHS

MODIS Band	Wavelength (μm)	Rayleigh Optical Depth	H_2O Optical depth	H_2O_K0	H_2O_K1	H_2O_K2	O_3 Optical depth	O_3_K0	O_3_K1	Dry-gas Optical depth
Blue	0.4706	1.85E-01	1.63E-04	-9.35E+00	9.97E-01	-2.58E-03	3.94E-03	-8.98E-05	1.17E-05	1.62E-03
Green	0.6392	5.45E-02	5.30E-03	-5.85E+00	9.44E-01	-1.75E-02	2.87E-02	3.61E-04	8.35E-05	3.40E-03
Red	0.8644	1.56E-02	3.45E-03	-6.31E+00	9.76E-01	-1.19E-02	7.54E-04	4.62E-07	2.19E-06	5.38E-05
NIR	1.61	1.28E-03	2.93E-03	-6.51E+00	1.03E+00	-1.71E-03	8.09E-07	2.03E-07	1.79E-09	1.75E-02
SWIR 1	2.2429	3.38E-04	1.18E-02	-5.29E+00	1.25E+00	1.01E-03	4.69E-06	3.59E-08	1.37E-08	3.55E-02
SWIR 2	0.4706	1.85E-01	1.63E-04	-9.35E+00	9.97E-01	-2.58E-03	3.94E-03	-8.98E-05	1.17E-05	1.62E-03
SWIR 3	0.6392	5.45E-02	5.30E-03	-5.85E+00	9.44E-01	-1.75E-02	2.87E-02	3.61E-04	8.35E-05	3.40E-03

TABLE A1-7: ABI-GOES17 GAS ABSORPTION COEFFICIENTS AND OPTICAL DEPTHS

MODIS Band	Wavelength (μm)	Rayleigh Optical Depth	H_2O Optical depth	H_2O_K0	H_2O_K1	H_2O_K2	O_3 Optical depth	O_3_K0	O_3_K1	Dry-gas Optical depth
Blue	0.4705	1.85E-01	1.64E-04	-9.35E+00	9.98E-01	-2.70E-03	3.95E-03	-9.01E-05	1.17E-05	1.63E-03
Green	0.6388	5.48E-02	5.33E-03	-5.84E+00	9.45E-01	-1.74E-02	2.90E-02	3.67E-04	8.45E-05	3.40E-03
Red	0.8641	1.56E-02	3.52E-03	-6.29E+00	9.77E-01	-1.19E-02	7.61E-04	4.66E-07	2.21E-06	5.21E-05
NIR	1.6094	1.28E-03	2.97E-03	-6.49E+00	1.03E+00	-1.83E-03	8.09E-07	2.10E-07	1.78E-09	1.76E-02
SWIR 1	2.242	1.39E-04	1.20E-02	-5.27E+00	1.24E+00	8.59E-04	5.14E-06	2.75E-08	1.47E-08	3.46E-02
SWIR 2	0.4705	1.85E-01	1.64E-04	-9.35E+00	9.98E-01	-2.70E-03	3.95E-03	-9.01E-05	1.17E-05	1.63E-03
SWIR 3	0.6388	5.48E-02	5.33E-03	-5.84E+00	9.45E-01	-1.74E-02	2.90E-02	3.67E-04	8.45E-05	3.40E-03

TABLE A1-8: ABI-GOES18 GAS ABSORPTION COEFFICIENTS AND OPTICAL DEPTHS

MODIS Band	Wavelength (μm)	Rayleigh Optical Depth	H_2O Optical depth	H_2O_K0	H_2O_K1	H_2O_K2	O_3 Optical depth	O_3_K0	O_3_K1	Dry-gas Optical depth
Blue	0.4705	1.85E-01	1.65E-04	-9.34E+00	9.98E-01	-2.67E-03	3.98E-03	-8.93E-05	1.18E-05	1.62E-03
Green	0.639	5.47E-02	5.33E-03	-5.84E+00	9.44E-01	-1.74E-02	2.88E-02	3.67E-04	8.39E-05	3.39E-03
Red	0.8638	1.56E-02	3.57E-03	-6.28E+00	9.79E-01	-1.23E-02	7.63E-04	4.64E-07	2.22E-06	5.10E-05
NIR	1.6086	1.28E-03	3.01E-03	-6.48E+00	1.03E+00	-1.97E-03	8.09E-07	1.99E-07	1.79E-09	1.77E-02
SWIR 1	2.2416	3.39E-04	1.21E-02	-5.25E+00	1.24E+00	8.14E-04	5.08E-06	4.73E-08	1.52E-08	3.42E-02
SWIR 2	0.4705	1.85E-01	1.65E-04	-9.34E+00	9.98E-01	-2.67E-03	3.98E-03	-8.93E-05	1.18E-05	1.62E-03
SWIR 3	0.639	5.47E-02	5.33E-03	-5.84E+00	9.44E-01	-1.74E-02	2.88E-02	3.67E-04	8.39E-05	3.39E-03

TABLE A1-9: AHI-HIMAWARI-08 GAS ABSORPTION COEFFICIENTS AND OPTICAL DEPTHS

MODIS Band	Wavelength (μm)	Rayleigh Optical Depth	H_2O Optical depth	H_2O_K0	H_2O_K1	H_2O_K2	O_3 Optical depth	O_3_K0	O_3_K1	Dry-gas Optical depth
Blue	0.4703	1.86E-01	1.65E-04	-9.35E+00	1.00E+00	-2.82E-03	3.92E-03	-1.09E-04	1.16E-05	1.67E-03
Green	0.5105	1.33E-01	1.41E-03	-7.19E+00	9.83E-01	-5.72E-03	1.39E-02	-6.52E-05	4.06E-05	2.58E-04
Red	0.6398	5.45E-02	5.12E-03	-5.88E+00	9.44E-01	-1.76E-02	2.91E-02	3.39E-04	8.43E-05	3.36E-03

	0.8563	1.62E-02	7.54E-03	-5.52E+00	9.54E-01	-2.03E-02	8.28E-04	3.26E-07	2.41E-06	3.23E-05
SWIR 1	1.6098	1.28E-03	2.90E-03	-6.51E+00	1.03E+00	-1.79E-03	8.33E-07	1.88E-07	1.72E-09	1.74E-02
SWIR 2	2.257	3.30E-04	1.15E-02	-5.35E+00	1.29E+00	2.62E-03	1.56E-06	-1.11E-07	4.46E-09	4.79E-02
SWIR 3	0.4703	1.86E-01	1.65E-04	-9.35E+00	1.00E+00	-2.82E-03	3.92E-03	-1.09E-04	1.16E-05	1.67E-03

TABLE A1-10: AHI-HIMAWARI-09 GAS ABSORPTION COEFFICIENTS AND OPTICAL DEPTHS

MODIS Band	Wavelength (μm)	Rayleigh Optical Depth	H_2O Optical depth	H_2O_K0	H_2O_K1	H_2O_K2	O_3 Optical depth	O_3_K0	O_3_K1	Dry-gas Optical depth
Blue	0.4703	1.86E-01	1.64E-04	-9.35E+00	9.97E-01	-5.22E-04	3.91E-03	-1.09E-04	1.15E-05	1.66E-03
Green	0.5104	1.33E-01	1.41E-03	-7.19E+00	9.84E-01	-5.79E-03	1.39E-02	-6.56E-05	4.05E-05	2.55E-04
Red	0.6404	5.43E-02	5.01E-03	-5.90E+00	9.44E-01	-1.75E-02	2.88E-02	3.07E-04	8.37E-05	3.80E-03
NIR	0.8563	1.62E-02	7.55E-03	-5.52E+00	9.54E-01	-2.02E-02	8.29E-04	3.22E-07	2.41E-06	3.23E-05
SWIR 1	1.607	1.29E-03	3.09E-03	-6.45E+00	1.03E+00	-2.10E-03	6.90E-07	7.61E-09	1.92E-09	1.98E-02
SWIR 2	2.2572	3.30E-04	1.15E-02	-5.35E+00	1.29E+00	2.63E-03	1.46E-06	-3.82E-08	4.31E-09	5.21E-02
SWIR 3	0.4703	1.86E-01	1.64E-04	-9.35E+00	9.97E-01	-5.22E-04	3.91E-03	-1.09E-04	1.15E-05	1.66E-03

TABLE A1-11: eMAS-SEACR4S GAS ABSORPTION COEFFICIENTS AND OPTICAL DEPTHS

MODIS Band	Wavelength (μm)	Rayleigh Optical Depth	H_2O Optical depth	H_2O_K0	H_2O_K1	H_2O_K2	O_3 Optical depth	O_3_K0	O_3_K1	Dry-gas Optical depth
Blue	0.4666	1.92E-01	1.11E-04	-9.45E+00	1.00E+00	-6.64E-04	3.33E-03	-9.54E-05	9.81E-06	1.64E-03
Green	0.5504	9.79E-02	8.20E-04	-7.44E+00	9.88E-01	-4.15E-03	3.18E-02	6.69E-05	9.22E-05	1.56E-03
Red	0.6546	4.81E-02	5.33E-03	-5.55E+00	9.39E-01	-1.85E-02	2.14E-02	5.27E-05	6.21E-05	1.62E-03
NIR	0.8652	1.56E-02	1.90E-03	-6.64E+00	1.00E+00	-8.24E-03	7.36E-04	4.50E-07	2.14E-06	5.77E-05
	0.9459	1.07E-02	6.28E-01	-6.48E-01	6.41E-01	-1.90E-02	2.02E-04	3.45E-08	5.88E-07	5.35E-05
	1.6063	1.29E-03	2.28E-03	-6.46E+00	1.03E+00	-2.20E-03	7.08E-07	1.26E-08	1.97E-09	2.00E-02
	1.6625	1.13E-03	5.69E-03	-5.66E+00	1.09E+00	-1.13E-02	5.14E-07	-1.99E-09	1.51E-09	1.35E-02
	1.8749	6.94E-04	5.97E+00	1.63E+00	6.98E-01	2.12E-02	9.48E-06	2.55E-07	2.71E-08	3.26E-03
	2.126	4.19E-04	1.95E-02	-4.25E+00	9.47E-01	-9.10E-03	4.12E-05	1.10E-06	1.18E-07	7.24E-03
	2.2737	3.20E-04	1.14E-02	-5.06E+00	1.26E+00	4.86E-04	1.19E-07	1.19E-07	-2.48E-24	6.76E-02

TABLE A1-12: eMAS-FIREX_AQ GAS ABSORPTION COEFFICIENTS AND OPTICAL DEPTHS

MODIS Band	Wavelength (μm)	Rayleigh Optical Depth	H_2O Optical depth	H_2O_K0	H_2O_K1	H_2O_K2	O_3 Optical depth	O_3_K0	O_3_K1	Dry-gas Optical depth
Blue	0.4716	1.84E-01	1.22E-04	-9.35E+00	9.93E-01	-4.47E-04	4.05E-03	-1.03E-04	1.19E-05	1.85E-03
Green	0.5535	9.53E-02	9.34E-04	-7.31E+00	9.84E-01	-4.77E-03	3.30E-02	8.71E-05	9.56E-05	1.98E-03
Red	0.6595	4.68E-02	5.09E-03	-5.60E+00	9.38E-01	-1.90E-02	1.97E-02	3.62E-05	5.72E-05	6.19E-04
NIR	0.8691	1.53E-02	1.88E-03	-6.65E+00	1.01E+00	-1.03E-02	6.73E-04	4.32E-07	1.96E-06	8.13E-05
	0.9497	1.06E-02	6.14E-01	-6.67E-01	6.37E-01	-2.19E-02	1.93E-04	3.99E-08	5.60E-07	5.99E-05
	1.6163	1.26E-03	1.92E-03	-6.64E+00	1.04E+00	-6.41E-04	7.56E-07	1.49E-08	2.20E-09	1.79E-02
	1.6715	1.10E-03	8.66E-03	-5.26E+00	1.08E+00	-2.12E-02	4.57E-07	3.75E-09	1.32E-09	1.17E-02
	1.885	6.79E-04	5.84E+00	1.61E+00	7.01E-01	2.23E-02	1.16E-05	2.42E-07	3.33E-08	3.28E-03
	2.1372	4.10E-04	2.09E-02	-4.19E+00	9.51E-01	-1.01E-02	8.80E-05	2.33E-06	2.52E-07	6.69E-03
	2.2862	3.13E-04	1.48E-02	-4.78E+00	1.23E+00	-4.93E-04	1.19E-07	1.19E-07	-2.48E-24	7.61E-02

A2. Table of Run Time QA Flags of Level 2 Aerosol Products

This appendix accompanies the information for dark target aerosol flags, given in the QA plan for C61 (MODIS Atmosphere QA Plan for Collection 061) available at this link. and also listed the differences of the QA plan between DT package output and the QA plan for MODIS C6.1

The *Quality Assurance* (QA) information is stored in multiple Scientific Data Sets (SDSs). Probably the most useful is the Quality Assurance *Confidence* (QAC) flag given as the 'Land_Ocean_Quality_Flag' SDS. This SDS is an integer between 0 and 3 that provides the quality assurance confidence (QAC) of the retrieval pixel, where 0=bad/no confidence, 1=marginal/low confidence, 2=good/moderate confidence and 3=very good/high confidence. The value of this 'Land_Ocean_Quality_Flag' is determined by the processing (logic) path taken during the aerosol retrieval, and can, in principle, be diagnosed by decoding one or two additional SDSs. These aerosol QA includes product quality flags, retrieval processing flags, and input data resource flags which are designed separately for land and ocean because of the differences of retrieval algorithms. Particular flags may indicate: a) conditions why retrieval was not attempted at all (e.g. input data outside of boundary conditions), b) cases where input data quality may be poor (e.g. large cloud fraction), so that the retrieval is performed with lower confidence, or c) cases where retrieval may have been performed but the results were poor (e.g. results outside of realistic physical conditions).

For MODIS C6.1, the additional QA SDSs are known as 'Quality_Assurance_Land' and 'Quality_Assurance_Ocean'. These are of type "byte" and must be decoded bit-by-bit to decode their information. (For AERDT and XAERDT (VIIRS and GEO sensors), the analogous information is contained in a type= "integer/short" SDS named 'Error_Land_And_Ocean'. This SDS has two layers representing ocean (1) and land (2).

Table A2-1 and **Table A2-2** describe the byte decoding of the Quality_Assurance_Land, and Quality_Assurance_Ocean SDSs respectively. Each flag corresponds to a certain number of bits, and bit values corresponding to results of certain tests. Note that within the retrieval processing QA flags also known as processing path flags, the flags representing the case of valid retrieval but lower confidence is Part I. Similarly, the flags representing the case of no valid retrieval is in Part II. Under the column "Comments", we list how other flags may be reset (if applicable). For example, if Part I over land receives the value of 8 (less than optimal clear sky pixels) then the QAC bits will be set to 2 (good quality).

Compared to Product quality and retrieval processing QA flags in MODIS C6.1, the QA flags were changed to actual integer number for all DT package products and stored these information in two parameters Land_Ocean_Quality_Flag and Error_Flag_Land_And_Ocean. Land_Ocean_Quality_Flag uses integers from 0 to 3 to represent the quality of the retrieved data following descriptions in product quality QA summary flags in Table A2-1 and Table A2-2. Table A0-1 and Table A2-4 are the retrieval processing QA flags, which does not separate into Part I and Part II as in Table A2-1 and Table A2-2. Each condition has its own representing integer. The retrieval processing QA flags record the conditions of retrieval and provide additional information to the quality assigned in Land_Ocean_Quality_Flag.

TABLE A2-1: PRODUCT QUALITY AND RETRIEVAL PROCESSING QA FLAGS OVER LAND

Flag name	# of bits	Bit value	Description	Comments
Product quality QA summary flags				
Summary quality flag for aerosol optical thickness ("QA usefulness")	1	0 1	Not useful data Useful	0) All products are fill values 1) Valid products
Estimated quality flag of aerosol optical thickness "QA Confidence flag" (QAC)	3	0 1 2 3 4-7	Poor Marginal Good Very Good Not Used (TBD)	
Summary quality flag for aerosol optical thickness	1	0 1	Not useful data Useful	Repeat of bit 0
Estimated quality flag of aerosol optical thickness	3	0 1 2 3 4-7	Poor Marginal Good Very Good Not Used (TBD)	Repeat of bits 1-3
Retrieval processing QA flags - Processing path flags				
Part I: retrieving condition flags when inversion is performed - retrieved value will be output	4	0 1 2 3 4 5 6 7 8 9 10 11 12 13-15	Retrieval performed normally (no issues) Procedure 2 performed (semi-bright surface, $\rho_{SWIR2} > 0.25$) Water pixels in 10 x10 box Possible Cirrus present Fitting error > 0.25 $-0.1 <$ Retrieved $\tau_{0.55} < 0.0$ # pixels between 12 & 20 # pixels between 21 & 30 # pixels between 31 & 50 Ångstrom out of bounds Retrieved $\tau_{0.55} < 0.2$ $>50\%$ coastal pixels Not used (TBD)	0) QAC=3 1) QAC=0 2) QAC=0 3) QAC=0 4) QAC=0 5) QAC=3 6) QAC=0 7) QAC=1 8) QAC=2 9) QAC=0 10) QAC=3 11) QAC=0 12) QAC=0
Part II: retrieving condition flags when inversion is NOT performed – fill values are output	4	0 1 2 3 4 5 6 7-8	No error Solar/sensor geometry out of bounds in LUT Apparent reflectance out of bounds in LUT # pixels < 12 $\rho_{SWIR2} > 0.35$ (too bright) Retrieved $\tau_{0.55} < -0.1$ Retrieved $\tau_{0.55} > 5.0$ Not used (TBD)	QAC=0 QA Useful flag = 0
Aerosol Type	2	0 1 2 3	All empty	Not currently filled
Thin cirrus or stratospheric aerosol index	2	0 1 2 3	All empty	Not currently filled

Retrieval processing QA flags - Input data resource flags				
Total ozone	2	0 1 2 3	GDAS/GMAO	
Total precipitable water	2	0 1 2 3	GDAS/GMAO	
Snow cover	2	0 1 2-3	TBD	
Spare	6		TBD	

TABLE A2-2: PRODUCT QUALITY AND RETRIEVAL PROCESSING QA FLAGS OVER OCEAN

Flag name	# of bits	Bit value	Description	Comments
Product quality QA summary flags				
Summary quality flag for "best" solution: "QA usefulness" flag	1	0 1	Not useful Useful	0) products are fill values 1) valid products
Estimated quality of aerosol parameters of "best" solution "QA Confidence" or "QAC"	3	0 1 2 3 4-7	Poor Marginal Good Very Good Not Used (TBD)	
Summary quality flag for "average" solution: "QA usefulness" flag	1	0 1	Not useful Useful	0) products are fill values 1) valid products
Estimated quality of aerosol parameter of "average" solution "QA Confidence" or "QAC"	3	0 1 2 3 4-7	Poor Marginal Good Very Good Not Used (TBD)	average solution is used for populating joint product
Retrieval processing QA flags - Processing path flags				
Part I: retrieving condition flags when inversion is NOT performed - fill values are output	4	0 1 2 3 4 5 6 7 8 9 10 11-15	Retrieval is performed Glitter present (GA < 40°) Cloudy (less than 10 pixels) Not used Number of valid VIS/NIR channels (Green-NIR1) is insufficient Number of valid channels < 3 Geometry out of bounds Land pixels in 10 × 10 km box Retrieved $\tau_{0.55}$ < -0.01 Retrieved $\tau_{0.55}$ > 5.0 No valid reflectance for any channel TBD	0) QAC defined by Part II 1) QAC=0, no retrieval, but some arrays filled. 2-10) QAC = 0, and no arrays filled.

Part II: retrieving condition flags when inversion is performed - retrieved value will be output	4	0	Retrieval performed normally	*0)* QAC=3
		1	Number of pixels within 10×10 km box is < 10% (40 pixels)	*1)* QAC=1
		2	Signal enough to retrieve τ; Set size distribution η = fill value	*2)* QAC=2
		3	SWIR1 channel not used	*3)* QAC=1
		4	SWIR2 channel not used	*4)* QAC=1
		5	SWIR2 & SWIR1 not used	*5)* QAC=0
		6	Variability of reflectance: Large uncertainty in both retrieved τ and aerosol type	*6)* QAC=1
		7	Variability of reflectance: Large uncertainty in retrieved τ, but aerosol type is stable.	*7)* QAC=2
		8	The best value of e is larger than the threshold value (3%)	*8)* QAC=1
		9	$\tau_{0.55} < 0$ put to avoid bias in level 3 product	*9)* QAC=0
		10	$30° < GA < 40°$ (will be overwritten by either #11 or #12)	*10)* QAC=1
		11	$GA < 40°$. Glint (store only $\boldsymbol{\rho_\lambda}$, var, and number of pixels, unless #12)	*11)* QAC=0
		12	$GA < 40°$ and $\boldsymbol{\rho_{Blue}}/\boldsymbol{\rho_{Red}} < 0.95$ – Thick dust retrieval over glint	*12)* QAC=0
		13	$\rho_{NIR1}\&\rho_{Cirrus}$ suggest possible cirrus contamination	*13)* QAC=0
		14	$GA > 40°$ and $\rho_{Blue}/\rho_{Red} > 0.75$ -- Off glint thick dust	*14)* QAC=2
		15	No retrieval performed	*15)* QAC=0
		16-19	TBD	
		20	$\rho_{NIR} < 1.1$, ρ_{NIR} (Rayleigh) Not enough signal to retrieve anything (set $\tau_{0.55} = 0.0$ and size parameters to fill)	*20)* QAC=1
Retrieval processing QA flags - Input data resource flags				
Total ozone	2	0 1 2 3	GDAS/GMAO	
Total precipitable water	2	0 1 2 3	GDAS/GMAO	
Snow cover	2	0 1 2-3	TBD	
Spare	2		TBD	

TABLE A0-1: PRODUCT QUALITY AND RETRIEVAL PROCESSING QA FLAGS OVER OCEAN FOR DT PACKAGE

Scientific Data Set (SDS): "Error_Flag_Land_And_Ocean" **Description: Dark Target Aerosol Error Code** **Length: Integer*2** **Dimensions: 2 (First index or position Ocean, Second index or position Land)**			
Flag Name	**Int Length**	**Int Value**	**Int Value Definitions**
Ocean and Land Aerosol Error Flag *First index/position Ocean.*	1	0	**When Retrieval………….**
		1	Number of pixels used > threshold
		2	Number of pixels used < threshold
		3	Reflactance at 0.86 um <1.5 Rayleigh
		4	N/A
		5	Aerosol Content is variable (threshold 1)
		6	Aerosol Content is variable (threshold 2)
		7	Aerosol Type is variable
		8	Observations less than 3
		9	Optical depth(0.554 um) between -0.1 and 0.0
		10	Glint Angle between 30 and 40 Degrees
		11	Glint angle is < 40 degrees (Only glint,Reflactance and Number of pixels will be stored
		12	Algorithm detects dust in glint area
		13	Cirrus may be present
		14	Algorithm detects dust off glint area
		15	N/A
		16	N/A
		17	Reflavtance at 0.865 um is less than threshold
		18	N/A
		19	N/A
		20	**No Retrieval ………….**
		21	Glint angle(Reflactence,SD and pixels stored)
		22	Not enough pixels to process
		23	N/A
		24	N/A
		25	N/A
		26	Angles are out of Bound
		28	Optical Depth(0.554) < -0.10
		29	Optical Depth(0.554) < -0.10

TABLE A0-4: PRODUCT QUALITY AND RETRIEVAL PROCESSING QA FLAGS OVER LAND

Scientific Data Set (SDS): "Error_Flag_Land_And_Ocean" Description: **Dark Target Aerosol Error Code** Length: **Integer*2** Dimensions: 2 (First index or position Ocean, Second index or position Land)			
Flag Name	**Int Length**	**Int Value**	**Int Value Definitions**
Ocean and Land Aerosol Error Flag *Second index/position Land.*	1	0	**When Retrieval………….**
		1	Procedure > 1 only Continental model
		2	Water Pixel may be present
		3	Cirrus clouds may be present
		4	Fitting error is greater than 0.25
		5	Mass concentration & fine mode optical depth set to zero when Optical depth(0.54um) is negative.
		6	Number of pixels between 3% - 5%
		7	Number of pixels between 5%-8%
		8	Number of pixels between 8%-12%
		9	Optical depth is negative
		10	Optical depth((0.554 um) < 0.2
		11	**No Retrieval……….**
		12	N/A
		13	N/A
		14	N/A
		15	N/A
		16	N/A
		17	N/A
		18	N/A
		19	N/A
		20	N/A
		21	Angles are out of bound
		22	Data is not Available for wavelengths used
		23	Not enough pixels to process
		24	2.13 Threshold is not met
		25	Optical depth (0.554 um) < -0.10
		26	Optical depth (0.554 um) < 5.0

A3. Masking Over Land and Ocean

Masking clouds without masking aerosol events remains one of the most challenging issues faced by the aerosol retrieval algorithms. The following describes the steps for masking cloud and other unsatisfactory pixels when performing aerosol retrieval over land or ocean. Common to land and ocean are that the L1B reflectance data ρ_λ^{L1B} are corrected for gas absorption (Appendix 1) before masking tests are performed. If any of the pixels within the box are considered 'land' by the MxD35 cloud mask product, then the algorithm proceeds with the land retrieval algorithm. Only if all pixels in the box are 'ocean' is the ocean inversion performed. Separate cloud masks are used over land and ocean. Additional masks over land include snow and ice contamination as well as residual water bodies (such as lakes and swamps). The ocean retrievals require masking for glint and underwater sediments.

A3.1   Masking Over Ocean

A3.1.1   Cloud Masking Over Ocean

If all pixels in the retrieval box are considered to be 'water' then the ocean algorithm is followed. After the gas correction described in Section A1, the algorithm has the arduous task of separating 'good' pixels from 'cloudy' pixels. The standard MxD35 cloud mask includes using the brightness in the visible channels to identify clouds. This procedure will mistake heavy aerosol as 'cloudy', and miss retrieving important aerosol events over ocean. On the other hand, relying on IR-tests alone permits low altitude, warm clouds to escape and be misidentified as 'clear', introducing cloud contamination in the aerosol products. Thus, our cloud mask over ocean combines spatial variability tests (e.g. Martins et al., [*2002*]) along with tests of brightness in visible and infrared channels.

The algorithm marches through the $N \times N$ box, examining the standard deviation of ρ in every group of 3 by 3 pixels (ρ_{Green} for MODIS C6.1 product and ρ_{Red} for DT-package). These are performed pixel by pixel in high resolution, which is twice of the resolution than the ρ_{Blue}, except for MODIS, which is performed at 500 meter resolution.

If the group of 9 pixels has a standard greater than 0.0025, then the center pixel is labeled as 'cloudy' and is discarded [*Martins, et al. 2002*]. The only exception to this rule is for heavy dust, which may at times be as spatially inhomogeneous as clouds. Heavy dust is identified by its absorption at blue channel using the ratio (ρ_{Blue}/ρ_{Red}). This quantifies the difference that our eyes witness naturally. Dust absorbs at blue wavelengths and appears brown. Clouds are spectrally moderately absorbing and appear white to our eyes. If $\rho_{Blue}/\rho_{Red} < 0.75$, then the central pixel of the group of 9 is identified as 'dust' and will be included in the retrieval even if it is inhomogeneous. This is a conservative threshold that requires very heavy dust in order to avoid clouds. Less restrictive thresholds would permit more dust retrievals but might accidentally permit cloud contamination.

The spatial variability test separates aerosol from most cloud types, but sometimes fails at the centers of large, thick clouds and also with cirrus, both of which can be spatially smooth. The centers of large, thick clouds are very bright in the visible, and so we identify these clouds when $\rho_{Blue} > 0.40$. This is an extremely high threshold that translates into an aerosol optical thickness greater than 5.0, but only for non-absorbing aerosol. Absorbing aerosol never reaches that high value of reflectance and will pass this cloud test unscathed. Some high values of non-absorbing aerosol may be discarded along with bright clouds, but this confusion is rare. Most heavy aerosol loading, with $\tau > 5.0$, absorbs

somewhat at blue channel and fails to reach the 0.40 threshold value, exhibited by very bright white clouds.

Cirrus clouds are identified with a combination of infrared and near-infrared tests. Three infrared tests provided by the standard MODIS cloud mask, MxD35, are examined. The three IR tests are the "Thin Cirrus (IR) Test" (Bit 11), the "High Cloud (6.7 μm) Test" (Bit 15), and the "IR Temperature Difference Test" (Bit 18). If any of these three tests register as "applied", then the 2×2 box of 500 m pixels (1 km MxD35 pixel) is denoted as "cloudy", and none of these pixels are retained for aerosol retrieval. The near-infrared cirrus test is based on the reflectance in the 1.38 μm channel and the ratio $\rho_{Cirrus}/\rho_{NIR1}$ if ρ_{NIR1} is available [*Gao, et al. 2002*] . It is applied in the algorithm as a two-step process. If $\rho_{Cirrus} > 0.03$, then the pixel is 'cloudy'. If $0.005 \leq \rho_{Cirrus} \leq 0.30$ and $\rho_{Cirrus}/\rho_{NIR1} > 0.3$, then the pixels is also 'cloudy'.

If the reflectance at red channel (ρ_{Red}) does not exceed 1.5 times the Rayleigh reflectance in that channel ρ_{Red}^{R}) or the reflectance at 1.38 μm does not exceed 0.01, then the pixel is assumed to be 'not cloudy', unless the ratio $\rho_{Cirrus}/\rho_{NIR1}$ exceeds 0.3.

A3.1.2 Ocean Sediment Mask

The final mask applied to the data is the sediment mask, which identifies which ocean scenes are contaminated by river sediments [*Li et al, 2002*] and discards those pixels. The sediment mask takes advantage of the strong absorption by water at wavelengths longer than 1 μm. The resulting spectral reflectance over water with suspended sediments thus show elevated values in the visible, but not in the longer wavelengths. This creates a unique spectral signature quite different from clear ocean water and also different from airborne dust.

A3.2 Masking Over Land

A3.2.1 Cloud Masking Over Land

The algorithm generates a cloud mask over land using the mean weighted spatial variability of the $\sigma(\rho_{Blue})$ (> 0.0025) and $\sigma(\rho_{Cirrus})$ (> 0.003) channel reflectance, as well as the absolute value of the ρ_{Blue} (>0.4) and the ρ_{Cirrus} (> 0.025). The combination of the two channels yields information about both visibly bright thick clouds and visibly dim thin cirrus. Note, that the $0.01 < \rho_{Cirrus} < 0.025$ threshold allows cirrus contamination into the land aerosol retrieval. However, those retrievals will have QAC (Quality Assurance Confidence) set to zero.

The visible channel reflectance spatial variability test for land is similar to that for ocean (as described by Martins et al., [*2002*]), although the ρ_{Blue} channel (at 500 m resolution) is used instead, and the algorithm calculates the mean weighted standard deviation (of the reflectance of each group of 3×3 pixels. If that standard deviation is greater than 0.0025, then the center pixel of the 3×3 pixel box is considered a cloud. For pixels that fail the mean weighted spatial variability test, an additional test is applied to call back optically thick smoke. If the straight (not mean weighted) standard deviation of the 3×3 pixel box is less than 0.0075, the pixel is considered to be clear even if it failed the mean weighted spatial standard deviation test.

The final cloud mask is the union of the four cloud mask tests described above.

A3.2.2 Snow and Inland Water Masking

A number of other tests are performed at a variety of resolutions to remove contamination by "wet" pixels, including snow fields, swamps, and inland water bodies. These pixels would be expected to

have poorly behaved VISvsSWIR2 surface reflectance relationships. Note that the reflectance data have already been cloud masked and corrected for gas absorption.

The snow/ice mask determined by an NDVI-like ratio of Red and NIR1 channel reflectances (at 500 m resolution), i.e. $ratio = (\rho_{NIR}^{L1B} - \rho_{NIR1}^{L1B})/(\rho_{NIR}^{L1B} + \rho_{NIR1}^{L1B})$, and the brightness temperature of the TIR2 (e.g. 11 μm MODIS thermal band) – interpolated to 500 m resolution. If the ratio is greater than 0.01 and $BT_{TIR2} < 285K$, then the pixel is considered a snow or ice contaminated and masked [*Li et al., 2005*]. For senors that does not have NIR1 channel (VIIRS, GOES series, and AHI), SWIR1 channel is used instead. The threshold for the new ratio is 0.3 and $BT_{TIR2} < 280K$.

The inland water mask is determined by computing the traditional NDVI for the Red and the NIR channels in the resolution of blue channel, i.e. $NDVI = (\rho_{Red}^{L1B} - \rho_{NIR}^{L1B})/(\rho_{Red}^{L1B} + \rho_{NIR}^{L1B})$. If the NDVI value is greater than 0.1 it is considered an inland water body.

A4. Calculation of Mass Concentration

The following equations lead to derivation of Mass Concentration in units of [μg per cm^2]. In these equations: $dN/d\ln r$ is the number size distribution with r denoting radius (in μm). For a lognormal mode, r_g is the geometric mean radius, σ is $\ln\sigma_g$ representing the standard deviation of the radius, and N_0 is the number of particles per cross section of the atmospheric column (i.e. the amplitude of the lognormal size distribution). In our case, we assume that the distribution is normalized, so that $N_0 = 1$.

The number N is related to the volume V and area A distributions by:

$$\frac{dN(\ln r)}{d\ln r} = \frac{3}{4\pi r^3}\frac{dV}{d\ln r} = \frac{1}{\pi r^2}\frac{dA}{d\ln r} \qquad \text{Eq. A4-1}$$

N_0, V_0, and A_0 are the amplitudes of the corresponding distributions, i.e.

$$N_0 = \int_0^\infty \frac{dN(\ln r)}{d\ln r} \, d\ln r \qquad \text{Eq. A4-2}$$

$$V_0 = \int_0^\infty \frac{dV(\ln r)}{d\ln r} \, d\ln r \qquad \text{Eq. A4-3}$$

$$A_0 = \int_0^\infty \frac{dA(\ln r)}{d\ln r} \, d\ln r \qquad \text{Eq. A4-4}$$

For a single lognormal mode defined by

$$\frac{dN(\ln r)}{d\ln r} = \frac{N_0}{\sigma\sqrt{2\pi}} e^{\left(-\frac{\ln(r/r_g)^2}{2\sigma^2}\right)} \qquad \text{Eq. A4-5}$$

$$N_0 = V_0 \frac{3}{4\pi r^3} e^{-\frac{9}{2}\sigma^2} \qquad \text{Eq. A4-6}$$

the Moments of order k, M^k are defined as

$$M^K = \int_0^\infty r^k \frac{dN(\ln r)}{d\ln r} d\ln r = (r_g)^k \exp\left(0.5k^2\sigma^2\right) \qquad \text{Eq. A4-7}$$

The effective radius r_{eff} in [μm] is defined by the moments, i.e.

$$r_{eff} = \frac{M^3}{M^2} = \frac{\int_0^\infty r^3 \frac{dN}{d\ln r} d\ln r}{\int_0^\infty r^2 \frac{dN}{d\ln r} d\ln r} = \frac{3}{4}\frac{V_0}{A_0} = r_g \, e^{\left(\frac{5}{2}\sigma^2\right)} \qquad \text{Eq. A4-8}$$

The extinction coefficient, β_{ext} is related to the extinction efficiency Q_{ext} through the area distribution, and is specific to each mode

$$Q_{ext} = \frac{\beta_{ext}}{\int_0^\infty \pi r^2 \frac{dN}{d\ln r} d\ln r} \qquad \text{Eq. A4-9}$$

These parameters are calculated via Mie code (MIEV, [*Wiscombe, 1980*]). Note that the scattering coefficient β_{sct} and efficiency Q_{sct} are related the same way. The mass extinction coefficient B_{ext} is in units of [area per mass] and depends on the extinction efficiency and the particle density ρ (assumed to be 1 g per cm^3), such that $B_{ext} = 3Q_{ext}/4\,\rho r_{eff}$ [*Chin et al., 2002*]. For a single lognormal mode,

$$B_{ext} = \frac{3Q_{ext}}{4\rho}\frac{A_0}{\frac{3}{4}V_0} = \frac{3\beta_{ext}}{4\rho\pi r_g^3 \exp(4.5\sigma^2)} \qquad \text{Eq. A4-10}$$

However our aerosol models are sums of multiple modes, so that the area and volume distributions must take into account the contributions of each mode. If there are two modes, (i.e. modes 1 and 2), r_{eff} must be calculated this way:

$$r_{eff} = \frac{\int_0^\infty r^3 \frac{(dN_1 + dN_2)}{d\ln r} d\ln r}{\int_0^\infty r^2 \frac{(dN_1 + dN_2)}{d\ln r} d\ln r} \qquad \text{Eq. A4-11}$$

Similar modifications are made when calculating Q and thus B.

We can define the Mass Concentration conversion factor, M_c, as the inverse of B, such that $M_C = B^{-1}$. The columnar mass concentration, M [mass per area] is then defined as

$$\mathbf{M} = \boldsymbol{\tau}\mathbf{M_C} = \frac{\tau}{B} \qquad \text{Eq. A4-12}$$

The final columnar mass concentration product is a weighted combination of the fine and coarse model (τ^f and τ^c) and the mass concentration coefficients of each model, i.e.,

$$\mathbf{M} = \boldsymbol{\tau}^f \mathbf{M}_C^f + \boldsymbol{\tau}^c \mathbf{M}_C^c \qquad \text{Eq. A4-13}$$

TABLE A4-1: EXTINCTION PROPERTIES OF THE AEROSOL MODELS USED FOR THE C6 OVER-LAND LOOKUP TABLE

Model	ω_0	Q_{ext} [unitless]	r_{eff} [μm]	β_{ext} [μm²]	B_{ext} [m²/g]	M_c [μg/cm²]
Continental	.8860	0.6210	0.292625	.0010	1.5910	62.8600
Moderately Absorbing / Developing World	.9200	1.0180	0.261287	.0370	2.9220	34.2230
Non-absorbing / Urban-Industrial	.8690	0.9770	0.256210	.0300	3.5330	28.3070
Absorbing / Smoke	.9470	1.1720	0.207507	.0580	3.4310	29.1460
Spheroid / Dust	.9530	1.3390	0.679582	.5450	1.4770	67.6960

Listed for each model are the single scattering albedo, extinction efficiency, effective radius, extinction coefficient, mass extinction coefficient and mass concentration conversion factor. These parameters are defined at 0.55 μm, for $\tau_{0.55} = 0.5$. The particle density is assumed to be 1 g /cm³.

A5. Merged Deep Blue/Dark Target SDSs

The dark target algorithm over land (e.g., Levy et al., [*2007a, b*]) is not designed to retrieve aerosol over bright surfaces, including desert. This leaves significant holes in global aerosol sampling. However, in recent years, Hsu et al. [*2004, 2006*] have developed an algorithm that retrieves aerosol properties over brighter surfaces. This algorithm, known as Deep Blue (DB), makes use of the observation that even visually bright desert scenes have low surface reflectance and are relatively stable in the deep-blue wavelengths (e.g., 0.41 and 0.47 μm for MODIS). The DB algorithms have also been revised for C6, and notably will now also provide coverage over vegetated land surfaces [*Sayer et al., 2013; Hsu et al., 2013*]; therefore, there are land areas that can be retrieved by both DB and DT algorithms.

For MODIS C6.1, we introduce a new "best-of" AOD product that combines DB, DT-land and DT-ocean. This will be reported by the SDS named "Dark_Target_Deep_Blue_Optical_Depth_550_Combined". A climatology from the MODIS-derived, monthly, gridded NDVI product (MYD13C2, [*Huete et al., 2011*]) is used as a map for assigning which algorithm takes precedence. This database is a set of 12 multiannual monthly means, gap-filled using the nearest month. If (NDVI > 0.3) then use the results from DT (τ_DT). If (NDVI < 0.2) then use results from DB (τ_DB). For the transition areas (0.2 ≤ NDVI ≤ 0.3), the routine considers the confidence as indicated by QAC values (Q_DT and Q_DB), where high confidence means Q_DT = 3 or Q_DB ≥ 2. If both are high confidence, the AOD is the average of the two, in other words,

$$M = \frac{1}{2}(\tau^{DT} + \tau^{DB}) \qquad \text{Eq. A5-1}$$

If only one retrieval has high confidence, then the AOD is assigned to that retrieval. If neither has high confidence, then the combined AOD remains undefined. Table A5-1 reports the SDSs referring to the DT/DB merging. A comprehensive analysis of the differences in retrieved AOD from DT, DB and the DBDT merged product is provided in Sayer et al., [*2019*]. There is no merged DT, DB product for DT-Package produced products.

TABLE A5-1: COMBINED DARK TARGET/DEEP BLUE SDSs FOR MODIS C6.1 PRODUCT:

C6 SDS	C6 dimension	New parameter description
Dark_Target_Deep_Blue_Optical_Depth_550_Combined	X, Y	"best of" AOD
Dark_Target_Deep_Blue_Optical_Depth_550_Combined_QA	X, Y	QAC assignment
Dark_Target_Deep_Blue_Optical_Depth_550_Combined_AlgFlag	X, Y	Which product?

A6. Cloud Diagnostic Products

Three diagnostic aerosol cloud parameters are included the DT products (Table A6-1). During the cloud masking operations (separate for land and ocean), the algorithm keeps track of whether a given 500m pixel is considered to be "cloudy" or "clear". This information is carried along in an array of bits (0 = cloudy, 1 = clear) and reported as "Aerosol_Cldmsk_Land_Ocean". As this cloud mask is created, the algorithm also determines the distance from every pixel to the nearest "cloudy" pixel. This is "Cloud_Distance_Land_Ocean". The intention is that users concerned about aerosol retrievals affected by cloud adjacency effects (3-D effects) or by humidified aerosols and cloud fragments in cloud fields (twilight zone) can trace exactly which pixels were used in the retrieval or plot the retrievals as a function to the nearest cloud. There is also a product that offers the average distance to the nearest cloud of all the pixels within the aerosol retrieval box that are used to generate the aerosol output, i.e., "Average_Cloud_Distance_Land_Ocean". An example of the 500 m parameters is shown in Figure A6-1.

TABLE A6-1: AEROSOL CLOUD DIAGNOSTIC PRODUCTS:

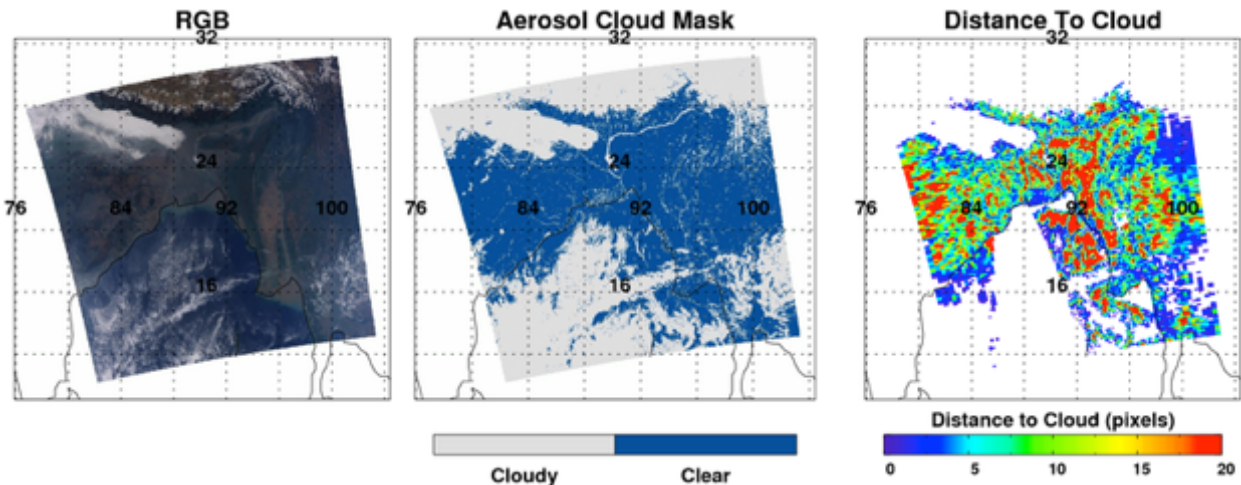| SDS	DIMENSION	DESCRIPTION
Aerosol_Cldmsk_land_Ocean	Twice the resolution of blue channel	Cloud mask used in retrieval
Cloud_Distance_Land_Ocean		Distance each pixel to nearest cloudy pixels
Average_Cloud_Distance_Land_Ocean	10 km, except 7.5 km for VIIRS	Average distance to cloud in retrieval box

Figure A6-1: New aerosol cloud mask variables, both from an Aqua granule on 3 January 2010 at 07:20 UTC. (a) RGB, (b) Aerosol cloud mask, (c) Distance to cloud (in pixels)

A7. Spectral relationship for GEO/LEO

The DT-L algorithms has been ported to GEO/LEO sensors based on the MODIS-based surface reflectance parameterization (SRP) (Eq. 7.7-9 in Sect. 7.3.2). Here, the MODIS-based SRP is denoted as the baseline SRP. In order to assess whether the baseline SRP can be used for these sensors, we repeat the analysis of VISvsSWIR2 relationship shown in Fig. 7-5 and Fig 7-6 (Sect. 7.3.2) with the recent 3 years (2019-2021) observations of MODIS (Aqua), VIIRS (SNPP), VIIRS (NOAA20), ABI-E (GOES-16), ABI-W (GEOS-17) and AHI (Himawari-8).

Figure A7-1 shows results from performing AC using from 2019 to 2021. The AC performed using dataset consists of the spatial TOA reflectance from satellite, spectral AOD from AERONET. AERONET observations within ±15 minutes of satellite overpass are collocated with satellite-derived TOA reflectance within ±0.2° rectangular grid centered over an AERONET site. The relationship between visible and SWIR2 surface reflectance remains similar to the baseline SRP. The visible surface reflectance are strongly correlated with SWIR2 surface reflectance. We are seeing variability in regression slopes between sensors because of wavelength shift and difference in spatial coverage.

Figure A7-1 to Figure A7-4 shows VISvsSWIR2 regressions (slope, y-intercept, and correlation coefficient) as a function of scattering angle in the same manner of Fig. 7-6 (b, c, and d). For MODIS, the change of slope and y-intercept with scattering angle not much different from the baseline SRP (Eq. 7-8). Analysis using VIIRS surface reflectance is also similar to the baseline, although the slope and y-intercept change dramatically with scattering angle.

The regressions obtained from GEO sensors shows a scattering angle dependence similar to MODIS and VIIRS, but the correlations are relatively weak (Figure A7-3). In particular, when the scattering angle is higher than ~150°, the correlation coefficient is significantly lower than that of MODIS and VIIRS. The reason for the differences is that LEO and GEO have very different viewing geometries. In a sun-synchronous polar-orbiting orbit, LEO sensor views a given ground target from a wide variety of VZA and RAA over a period of several weeks, while SZA varies slowly. In contrast, GEO sensors provide multiple images throughout a day and measure various solar angles for a location, and has more chance to observe surface hot-spot (near local noon) and shadowed dark surface (near sunrise/sunset). The broad range of geometries lead to a difficulty in SRP.
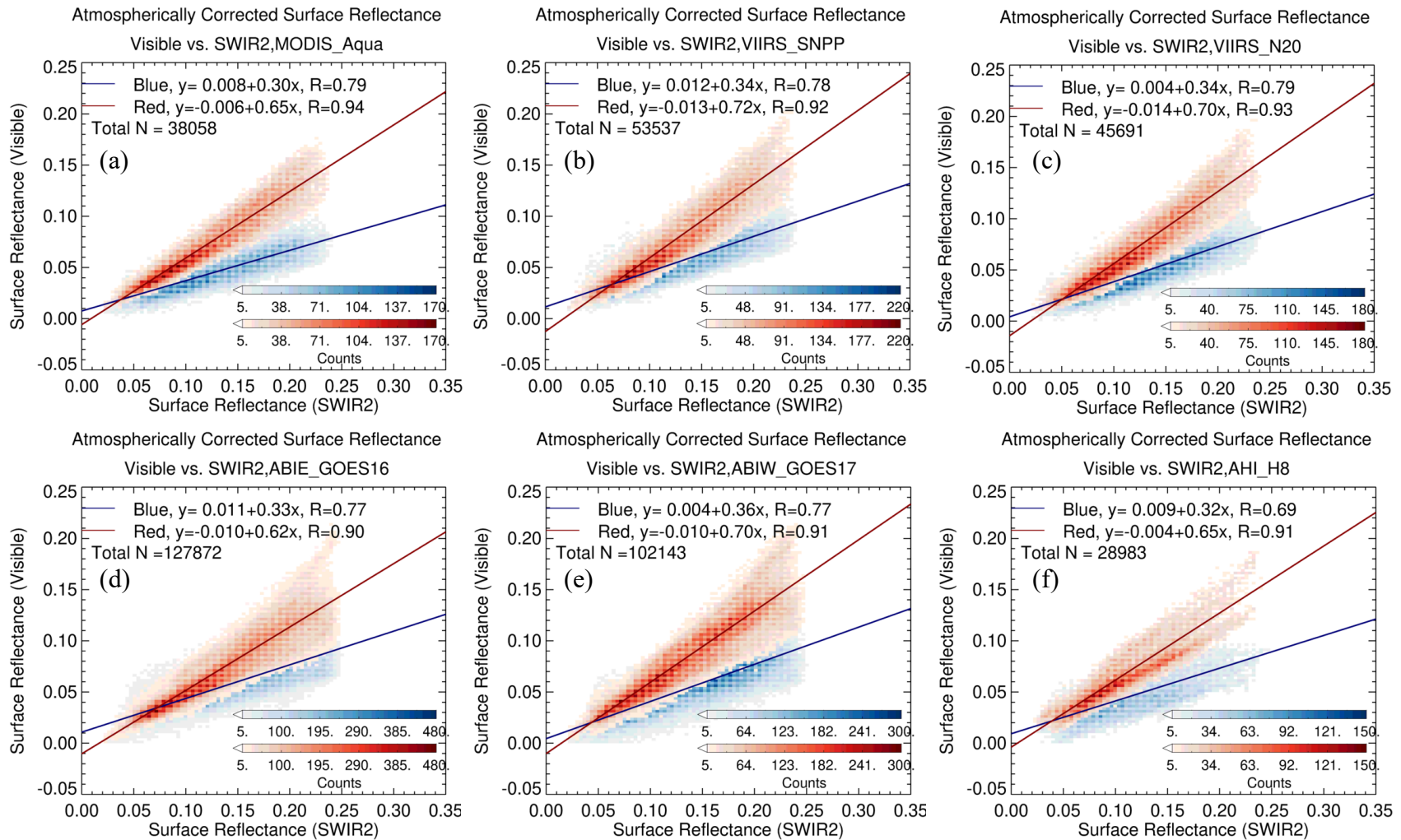
Figure A7-1: Atmospherically corrected surface reflectance in the visible (blue and red) compared with SWIR2. The red and blue indicates the RedSWIR and BlueSWIR relationship, respectively. The surface reflectance are derived from (a) MODIS (Aqua), (b) VIIRS (SNPP), (c) VIIRS (NOAA20), (d) ABI-E (GOES-16), (e) ABI-W (GOES-17), and (f) AHI (Himawari-8) for three years from 2019 to 2021.
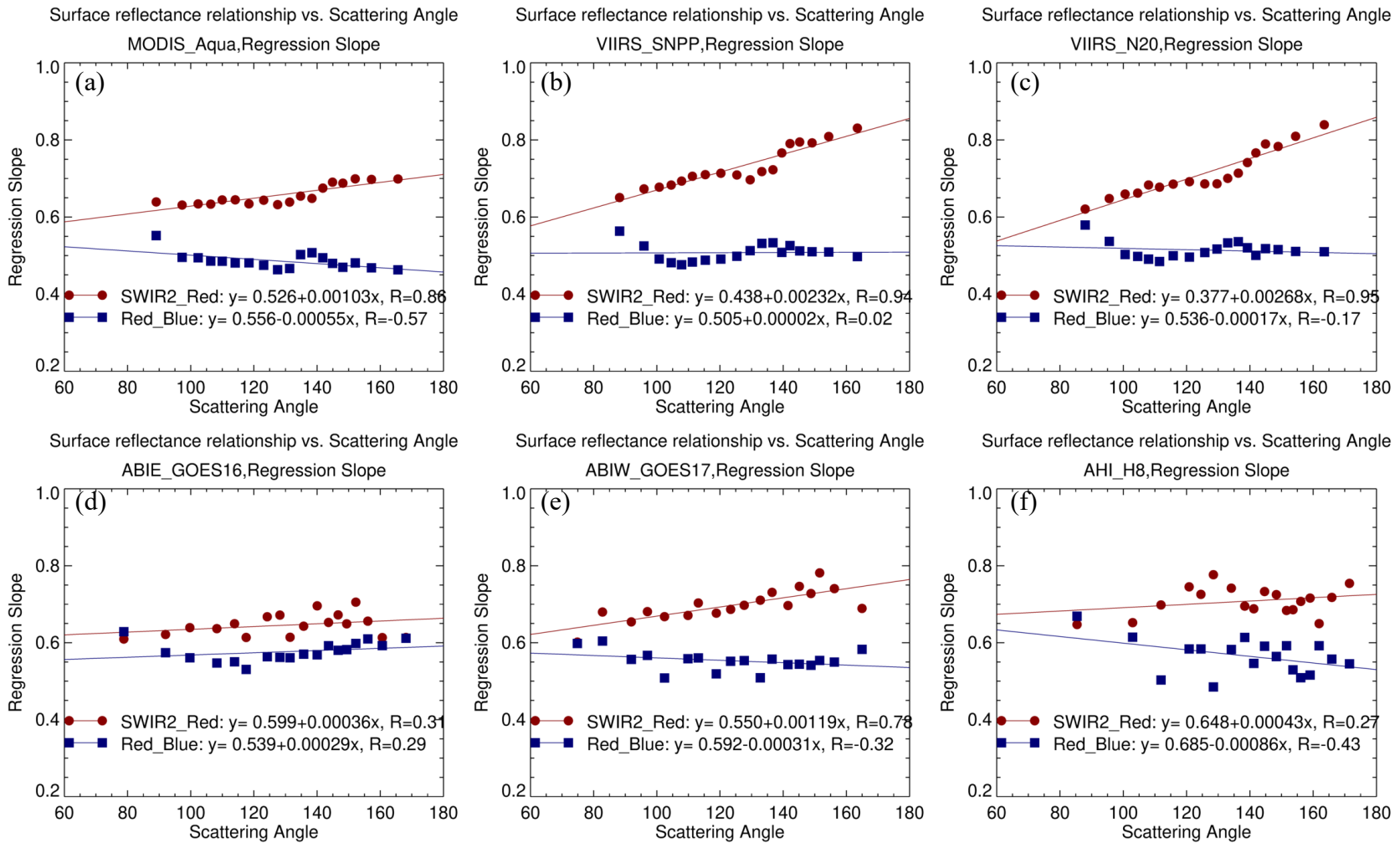
108

Figure A7-2: VISvsSWIR surface reflectance relationships obtained from (a) MODIS (Aqua), (b) VIIRS (SNPP), (c) VIIRS (NOAA20), (d) ABI-E (GOES-16), (e) ABI-W (GOES-17), and (f) AHI (Himawari-8): The slope of the regression as a function of scattering angle.
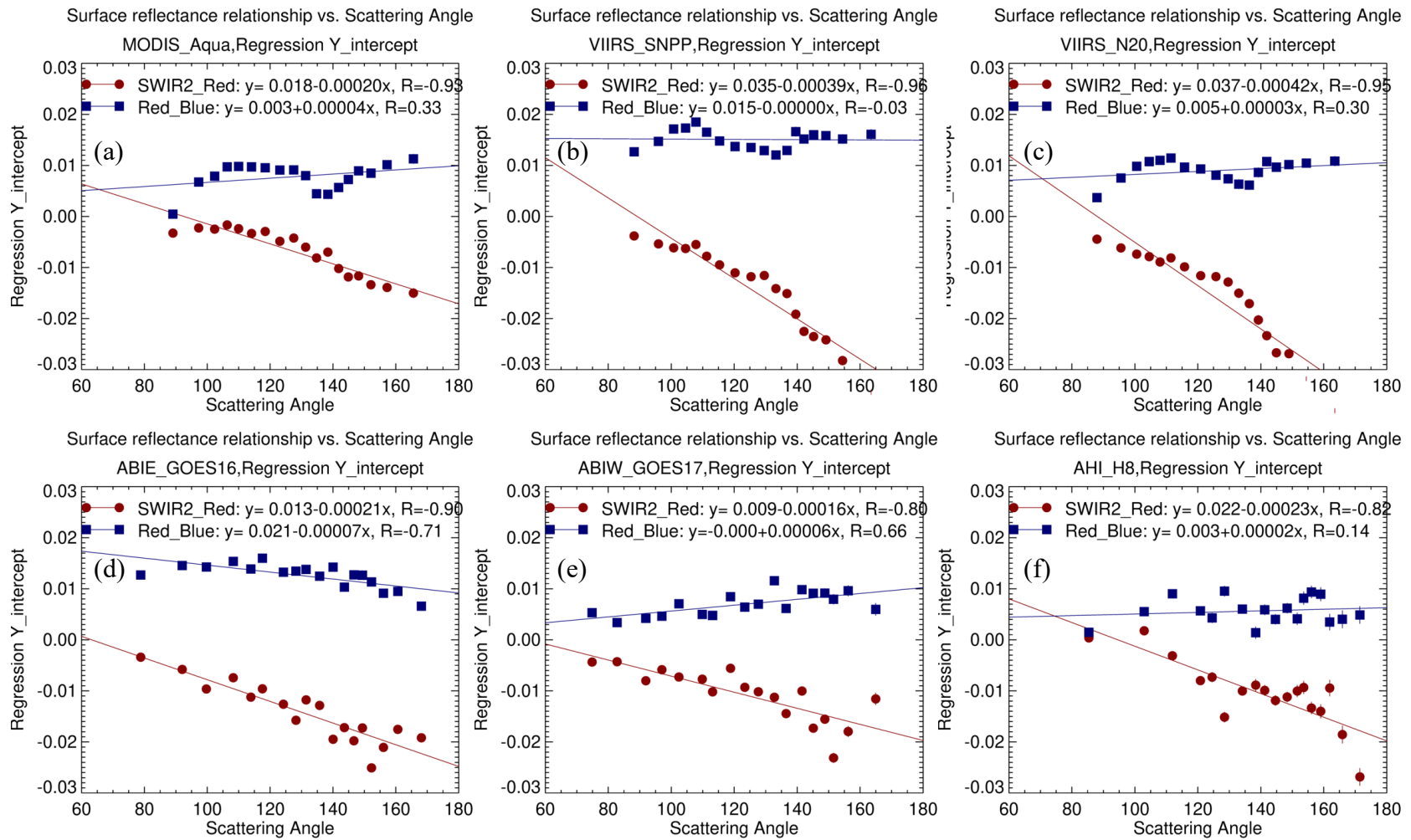
Figure A7-3: VISvsSWIR surface reflectance relationships obtained from (a) MODIS (Aqua), (b) VIIRS (SNPP), (c) VIIRS (NOAA20), (d) ABI-E (GOES-16), (e) ABI-W (GOES-17), and (f) AHI (Himawari-8): The y-intercepts as a function of scattering angle.
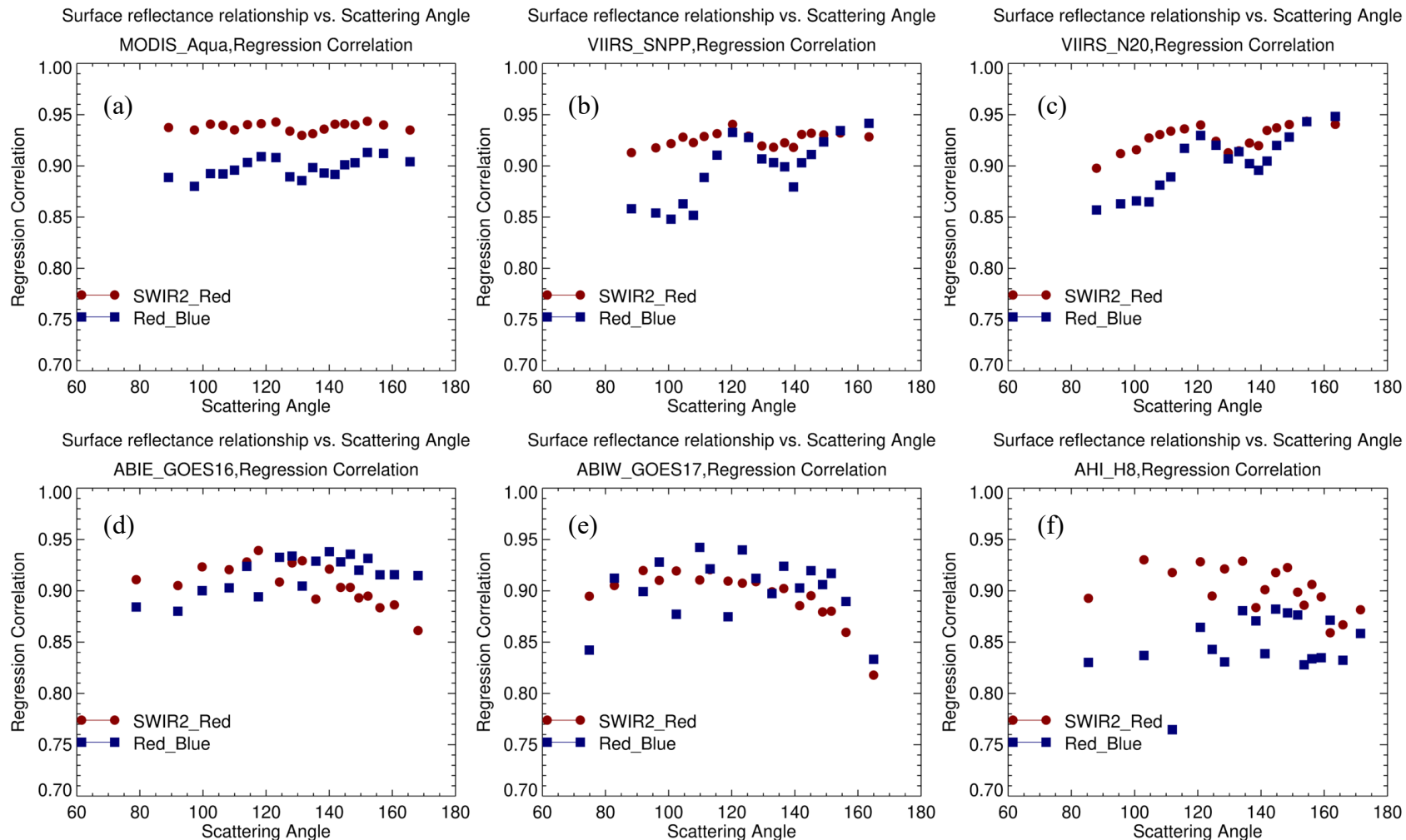
Figure A7-4: VISvsSWIR surface reflectance relationships obtained from (a) MODIS (Aqua), (b) VIIRS (SNPP), (c) VIIRS (NOAA20), (d) ABI-E (GOES-16), (e) ABI-W (GOES-17), and (f) AHI (Himawari-8): The correlation coefficients for each angle bins.